Computational Studies of the Chemical Properties of Complex Metalloenzyme Systems and Transition Metal Catalysis using Electronic Structure Methods

A DISSERTATION
SUBMITTED TO THE FACULTY OF THE
UNIVERSITY OF MINNESOTA
BY

Meghan E. McGreal

IN PARTIAL FULFILLMENT OF THE REQUIREMENTS
FOR THE DEGREE OF
DOCTOR OF PHILOSOPHY

Jason D. Goodpaster, Adviser

June, 2021

Dedication

I dedicate my dissertation to my father, Edward McGreal, who passed away on October 13th, 2017 from 9/11-related cancer. He was a first responder at the World Trade Center when he was a Captain in the NYPD. My dad was always my biggest fan, supporting me when I doubted myself and reminding me I am an intelligent, capable individual who has worked hard to earn all of the opportunities I have received throughout my professional career. Losing him was the hardest thing I have ever had to go through, and even though we found out about his cancer prior to my college graduation, he was the person who insisted I needed to focus on my career and not worry about him. We always shared a dream of my return to UNC Asheville to teach once I received my doctorate (because in his eyes there was no "if" I receive my doctorate). My only regret is that he is not here to see me realize and actualize this shared dream, as I will be returning to Asheville in Fall 2021 as a Physical Chemistry Lecturer. My world was completely turned upside-down when I lost my father, and at times the only thing keeping me going was knowing he had absolutely no doubts in my ability to succeed through graduate school to become Dr. Meghan E. McGreal. Thank you, Dad, and I am so proud to be your daughter.

Acknowledgements

There are many people to whom I owe thanks for supporting me throughout the course of my Ph. D. journey. First and foremost, I would like to thank my adviser, Dr. Jason Goodpaster, for his guidance, support and mentorship over these past six years. I would also like to thank the members of the Goodpaster group for the years of conversations, research assistance, ideas, and general support. There are a few members I would like to explicitly thank, however there is someone else I need to acknowledge first.

I would not have successfully completed my doctorate without Connie Anderson, my roommate of 4 years and best friend. We have been through this

journey together from day 1. Through all the tears, mental health struggles, and personal issues, she has stood by my side, providing comfort (and reality checks) when needed. I cannot express in words how influential Connie has been on my development, both personally and professionally, and simple thanks will never be enough to capture the profound effect she has had on my life.

From my group, I would like to thank Xuelan Wen, my groupmate since prior to the official beginning of our research group. We have worked together for almost 6 full years, through classes, research, conferences, and even teaching. I can say with certainty I would not still be in graduate school without the friendship, love, and support I received from her, from working on collaborations, to personal/family issues, and just general imposter syndrome struggles. Xuelan has become one of my best friends, and I look forward to our future friendship.

I would also like to thank Quin Hu and Andrew Johannesen. These two groupmates quickly became some of my closest friends, listening to my struggles, providing insight, and exposing me to new activities, such as working out and Dungeons & Dragons. I feel as though these two people have somewhat become my mentees in the group, however I also know these two have taught me much more than I have taught them, and their friendship greatly enriched my graduate school experience.

My family has been my support system throughout my entire educational experience. My mother, Angela, has always been supportive and pushed me to reach my full potential even when I did not understand or realize my own capabilities. Growing up, every person who knew my mother would inevitably accidentally call me Angela or Angie, and I could not be more proud to be mistaken for the strong woman who has managed to keep our family together throughout some of the most difficult times in our lives.

I also need to acknowledge my siblings and in-laws, Matt and Melissa McGreal, and Barett and Ryan (soon-to-be) Drummond. My siblings, Matt and Ryan, both followed me to UNC Asheville where I got my undergraduate degree. We had the unique experience of all being students at the same time, and my relationship with my siblings has only gotten stronger since we have all graduated. During the COVID-19 pandemic, I lived at home for 7 months where I was able to spend more time with them than I had throughout the entirety of my graduate career. Melissa McGreal and Barett Drummond have also become integral members of my family, and I am forever grateful for the love and support they, along with my siblings, have given me throughout the years.

I finally need to thank other members of my family for their undying support: Marilyn DeAlmeida, Julio Arniella, Guedy Arniella, Adela Arniella, Ish Lallave, Bryan McGreal, Jayne McGreal-Labbate, Stan & Nicki Swider, Steve Swider and Nick Swider. All of these people have listened to me drone on about the various work I have done, as well as the struggles I have faced and the successes I have accomplished, while always reminding me of how special my accomplishments are, especially when I try to minimize them.

I also need to thank my personal squad of cheerleaders, Aly Wright, Cindy Pyles, David Goldfeld, Beth Dewing, Mark Dresel, Nick Livezey, Bach Nguyen, Emily Potter, Kaylee Brookshire, Sam Groesbeck, Hung Pham, Debmalya Ray, and Prachi Sharma. Special shout out goes to my group mates Brianna, Eduardo, and Adrian for all the research work and editing throughout the years, and Hunter Wilson for being my mentee, collaborator, and involved in the research for half of this dissertation (Ch. 2, 5-6).

I have had many mentors throughout the years who have helped me develop into the educator I have become. Michelle Driessen, the director of General Chemistry at the U of M, noticed my passion for teaching early on and introduced me to Emily Pelton, my first mentor. I was the TA for her introductory chemistry course where I had the opportunity to interact with and teach students during her active learning class sessions. Much of my own teaching style has been influenced by Emily, and she was the person who strongly encouraged me to apply to be the Head General Chemistry TA. I also worked with Emily during my time in MPACT, where she provided me the opportunity to learn about her entirely online course, including creation of lecture video content, which became a more important skill than I ever expected due to the pandemic. After being hired as Head TA, I worked very closely with Michelle, where I learned all about the management of large general chemistry courses and how to effectively implement active learning techniques on this scale. I loved my time working with Michelle, and as with Emily, her teaching style has greatly influenced my own. Finally, during my semester teaching GenChem 2 at MetroState, Kate Ries was integral to the wonderful experience I had. She provided me with all of her teaching materials, making my first course run smoothly while allowing me to add my own style to the course content, and also to be a sounding board whenever issues arose that I had not previously experienced. These three professors were so important towards my development as an educator, and I am beyond excited to be able to continue developing my abilities as an educator in my lecturer position at my alma mater, UNC Asheville.

I would also be remiss to not mention one other mentor who had a strong influence on my graduate career, Jody Kaplan. I met Jody during the few weeks I worked in the Gagliardi group prior to the start of graduate school, and our friendship blossomed instantly. She was there throughout my entire graduate school journey, from my rough start to her last day working on campus and further. Our conversations about our families, past colorguard & dance experiences, obsession with figure skating and Dancing with the Stars, and even just complaining about the stress of graduate school made certain times throughout graduate school bearable, especially around the time my father passed away.

Finally, I would like to thank my committee for being part of my journey through the years. Your input and influence have helped shape my research projects into the fully realized stories I have presented here. I would also like to thank them for the time and effort put into reading, editing, and providing feedback on my work.

Abstract

Computational chemistry is a useful tool for studying the aspects of chemistry that cannot be wholly studied in a laboratory setting, such as mechanisms, electronic structure, reaction barriers, and other various chemical and physical properties. In this dissertation, computational chemistry methods, specifically Density Functional Theory (DFT), is utilized to study complex catalytic systems. These systems include transition-metal based metalloenzymes and molecular catalysts that were studied utilizing electronic structure methods.

Chapters 2, 3, and 4 focus on elucidation of catalysis, structural features, function, and other various properties of the [NiFe]-hydrogenase enzyme system. Specifically, the mechanism of catalysis was studied, appropriate models for the study of this bimetallic enzyme active site were determined (Chapter 2), the effect of mutation of highly conserved residues were analyzed (Chapter 3), and the influence biomimetic-inspired changes to the active site were assessed (Chapter 4). Chapter 5 focuses on elucidating the structure and function of the non-heme Fe chlorination enzyme, SyrB2, in collaboration with the Bhagi-Damodaran Group. Chapter 6 is a study of titanium-catalyzed nitrene transfer of diazenes to isocyanides for carbodiimide synthesis in collaboration with the Tonks Group. Finally, Chapter 7 is computational determination of the chemical hardness of various anions, as well as the effect of stability of anion impact, selectivity and affinity for Gd-containing complexes in collaboration with the Pierre Group.

Table of Contents

List of Tables

List of Figures

List of Abbreviations

DFT	Density Functional Theory
KS-DFT	Kohn-Sham Density Functional Theory
Cys	Cysteine amino acid residue (C)
Glu	Glutamic acid amino acid reside (E)
D. vulgaris	*Desulfovibrio vulgaris*
EPR	Electron Paramagnetic Resonance Spectroscopy
CC	Coupled Cluster
CASPT2	Complete Active-Space Second-Order Perturbation Theory Method
XQC	Quadratic Convergence
SCF	Self-Consistent Field Method
PCM	Polarizable Continuum Model
SHE	Standard Hydrogen Electrode
E. coli	*Escherichia coli*
Ser	Serine amino acid residue (S)
Leu	Leucine amino acid residue (L)
Pro	Proline amino acid residue (P)
QM/MM	Quantum Mechanics/ Molecular Mechanics Method
DMRG	Density Matrix Renormalization Group
P2T	Peak to Trough Energy
Arg	Arginine amino acid residue (R)
Asp	Aspartic acid amino acid residue (D)
FLP	Frustrated Lewis Pair
Asn	Asparagine amino acid residue (N)
Ala	Alanine amino acid residue (A)
Lys	Lysine amino acid reside (K)
S.E.M	Standard error of the mean
VMD	Visual Molecular Dynamics
Cp	Cyclopentadiene
Cp*	Pentamethylcyclopentadiene
Pdt	1,3-propanedithiol
Pedt	(1*Z*)-prop-1-en-1,3-dithiol
Bdedt	(1*Z*,3*Z*)-but-1,3-dien-1,4-dithiol
MRSA	Methicillin-resistant staphylococcus aureus
αKG	α-ketoglutarate
NOG	N-oxalylglycine
NBO	Natural Bond Orbital
SMD	Solvation Model based on Density
IBO	Intrinsic Bond Oribital
Py	Pyridine

1. Introduction

Computational chemistry is a useful tool for studying the aspects of chemistry that cannot be wholly studied in a laboratory setting, such as mechanisms, electronic structure, reaction barriers, and other various chemical and physical properties. In this dissertation, computational chemistry methods, specifically density functional theory (DFT), is utilized to study complex catalytic systems.

DFT is a quantum mechanical method that utilizes electron density to determine the energy of the system of study, which is a functional of the density. The difficulty in this is solving for the exact ground state electron density, which is found through minimization of the unknown total energy functional, $E_{tot}[\rho]$. One way to overcome this is known as the Kohn-Sham (KS) DFT method.[1] The KS-DFT method uses a fictitious system of non-interacting electrons that have the same density as the system to be studied where there are interactions between electrons.[1, 2]

The KS-DFT approximation allows the total electronic energy to be represented by equation 1.1, where each term is a functional of the electron density, ρ.

$$E_{tot}[\rho] = T_s[\rho] + E_{ne}[\rho] + J[\rho] + E_{xc}[\rho] \tag{1.1}$$

The first term is the kinetic energy of the non-interacting electrons, followed by the nuclear-electron interaction energy, the classical electron-electron repulsion, and finally the exchange correlation energy. This term includes the corrections to the kinetic energy from the interaction of electrons and all of the non-classical corrections to the electron-electron repulsion energy.[1, 2]

The electron density is given by the description of non-interacting electrons through the equation

$$\rho(\mathbf{r}) = \sum_{i=1}^{N_o} n_i \left|\psi_i^{KS}(\mathbf{r})\right|^2 \tag{1.2}$$

where N_o represents some number of orthogonal orbitals, ψ_i^{KS}, which are occupied Kohn-Sham molecular orbitals, and n_i are occupation numbers of ψ_i^{KS}. This is the density of the system of interest.[2] Using the dependence upon the KS orbitals shown in eq. 1.2 for the kinetic energy term, the total electronic energy equation can be rewritten with exact definitions of $T_s[\rho]$, $E_{ne}[\rho]$, and $J[\rho]$.

$$E_{tot}[\rho] = -\frac{1}{2}\sum_{i=1}^{N_o} n_i \left\langle \psi_i^{KS} \middle| \nabla^2 \middle| \psi_i^{KS} \right\rangle + \int V_{ne}\rho(\mathbf{r})d\mathbf{r} + \frac{1}{2}\iint \frac{\rho(\mathbf{r}_1)\rho(\mathbf{r}_2)}{r_{12}} d\mathbf{r}_1 d\mathbf{r}_2 + E_{xc}[\rho] \tag{1.3}$$

V_{ne} is the potential due to the nuclear-electron attraction, and r_{12} is the distance between two electrons. An explicit form for the $E_{xc}[\rho]$ cannot be written because this functional contains everything that is unknown. The variational principle is used to minimize the energy expression with respect to the orthonormalized ψ^{KS} orbitals.

$$\left[-\frac{1}{2}\nabla^2 + V_{ne} + \int \frac{\rho(\mathbf{r}_2)}{r_{12}} d\mathbf{r}_2 + V_{xc}(\mathbf{r}_1)\right]\psi_i^{KS} = \varepsilon_i \psi_i^{KS} \tag{1.4}$$

These equations are called the Kohn-Sham equations, from $i = 1$ to N_o KS orbitals. The exchange potential, V_{xc}, is defined as the functional derivative of $E_{xc}[\rho]$ with respect to $\rho(\mathbf{r})$:

$$V_{xc}(\mathbf{r}) = \frac{\delta E_{xc}[\rho]}{\delta\rho(\mathbf{r})}. \tag{1.5}$$

When combined, the last three terms in the brackets in eq. 1.4 are called the effective potential, V_{eff}. Therefore, eq. 1.4 can be simplified to

$$\left(-\frac{1}{2}\nabla^2 + V_{eff}(\mathbf{r}_1)\right)\psi_i^{KS} = \varepsilon_i\psi_i^{KS} \tag{1.6}$$

The terms in the parenthesis make up the one-electron Fock operator and must again be solved iteratively due to the dependence upon density exhibited by the Coulomb term, $J[\rho]$.[2]

The main concern with this method is that analytic expressions for E_{xc} and V_{xc} are unknown,[3] meaning that the KS-DFT approach does not produce an exact energy and density. However, there is a one-to-one relationship between the wave function and electronic density, meaning that all of the information needed can be found from the electronic density, in principle.[2, 3]

There are limitations to the DFT method due to the dependence upon the exchange correlation functional. The choice of functional affects the results calculated, overestimating or underestimating reaction barriers, while potentially producing qualitatively incorrect conclusions, such as predicting untrue mechanisms. For transition metal complexes, DFT also poorly predicts spectroscopic properties, including spin state.[2] Many DFT functionals also do not account for van der Waals interactions, however this is overcome by adding dispersion corrections to the calculation, which produces improved results for modeling systems, such as enzymes.[4, 5] Additionally, appropriate benchmarking studies have been performed for many chemical systems,[6, 7] allowing appropriate choice of functional for large models to be studied using electronic structure methods, in addition to other features such as the dispersion corrections mentioned or utilization of implicit solvation models to mimic the environment of the system.

In this dissertation, the study of the chemical properties of complex metalloenzyme systems and transition metal catalysis were performed utilizing KS-DFT computational chemistry methods. Chapters 2, 3, and 4 focus on elucidation of catalysis, structural features, function, and other various properties of the [NiFe]-hydrogenase enzyme system. Specifically, the mechanism of catalysis was studied, appropriate models for the study of this bimetallic enzyme active site were determined (Chapter 2), the effect of mutation of highly conserved residues were analyzed (Chapter 3), and the influence of biomimetic-inspired changes to the active site were assessed (Chapter 4).

The subsequent chapters 5-7 are all collaboration efforts with various experimental research groups. Chapter 5 focuses on elucidating the structure and function of the non-heme Fe chlorination enzyme, SyrB2, and assessing the fluorination capabilities of the enzyme with the Bhagi-Damodaran group. Chapter 6 is study titanium-catalyzed nitrene transfer of diazenes to isocyanides for carbodiimide synthesis with the Tonks group. Finally, Chapter 7 is computational determination of the chemical hardness of various anions in order study the stability of tripodal gadolinium complexes and the effect of anion impact, selectivity and affinity with the Pierre group.

2. Ni-Fe Hydrogenase – Study of the Mechanism and Enzyme Environment using Various Models of the Active Site

2.1 Introduction

Hydrogenases are metalloenzymes[8-11] that catalyze the reversible reaction of the oxidation of hydrogen gas into protons and electrons.[8, 12, 13] [NiFe]-hydrogenase is one of these enzymes, characterized by the transition metals found in the active site.[9, 10, 14, 15] A greater understanding of hydrogenase enzyme catalysis would provide insight into natural hydrogen oxidation, a vital stepping-stone towards energetically affordable industrial scale hydrogen catalysis. These specific enzymes have been found to rival Pt containing active sites with turnover frequencies exceeding 1000 s^{-1} for H_2 oxidation,[8, 16-19] so further elucidation of the structure/function relationship has the potential to provide insight for development of transition metal catalysts.

The [NiFe]-hydrogenase enzyme consists of αβ-heterodimers. The small β subunit contains three Fe-S clusters involved in transfer of electrons in/out of the catalytic active site, found in the large α subunit, to the surface of the protein. The proximal and distal clusters have the form of [4Fe-4S], while the medial cluster is [3Fe-4S]. Additionally, a hydrophobic gas channel for H_2 extends from the active site to the surface in the large α subunit, along with a proton transfer pathway hypothesized to transfer protons from a Ni-bound terminal cysteine (Cys) residue to a nearby glutamic acid (Glu) residue.[8, 18, 20-23]

Notable geometric features of the active site, in addition to the two transition metals, include three inorganic ligands, two cyanide and one carbonyl coordinated to the Fe center, two Cys residues bridging between the Ni and Fe centers, and two Cys residues bound terminally to the Ni.[14, 24-32] In order for catalysis to take place, the oxidized active site (Ni-A, Ni-B)[8, 22, 33-35] with a formal Ni (III) oxidation state must undergo the dissociation of a hydroxide or peroxide ligand bound in the μ position between the metals to enter the reduced states where catalysis occurs beginning with a formal Ni (II) oxidation state, Ni-SI$_a$.[31, 36-39]

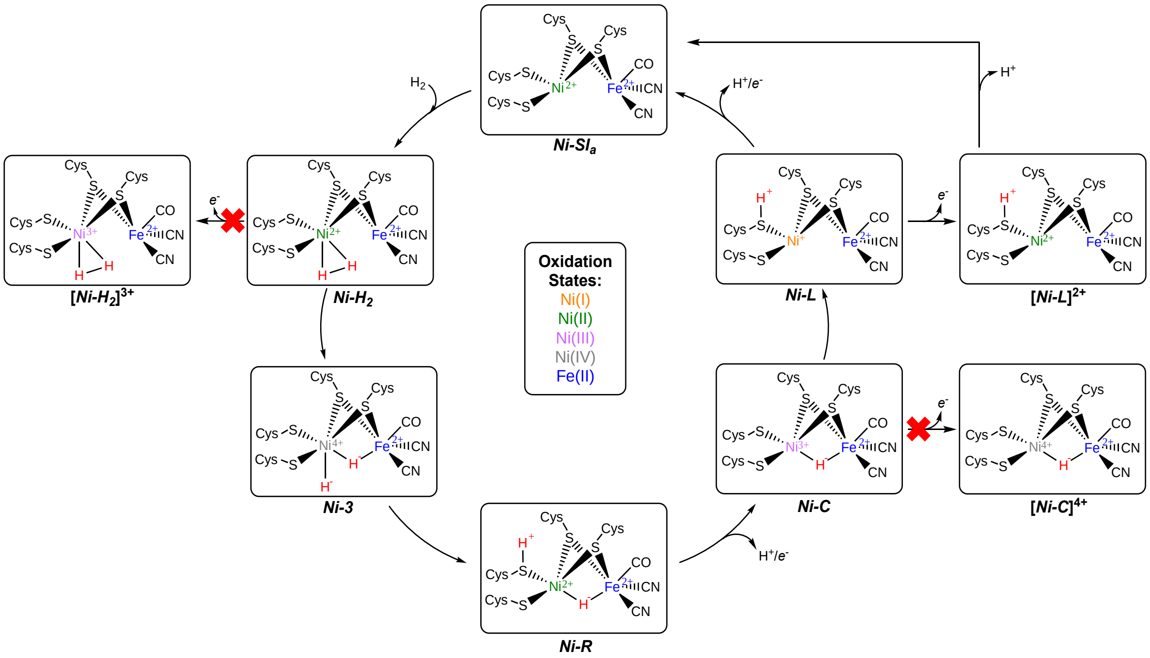

Figure 2.1: The proposed catalytic cycle for the reduced states of the oxidation of H_2 in [NiFe]-hydrogenase, and the possible oxidation pathways studied in this work.

Lubitz and coworkers[40] were able to resolve the hydrogen atoms in the crystal structure for [NiFe]-hydrogenase from the *desulfovibrio vulgaris* (*d. vulgaris*) organism. The intermediate isolated saw a bridging hydride between the metal centers and the protonation of one of the terminal cysteine residues, specifically Cys-546. Based on the crystallographic data and electron paramagnetic resonance (EPR) spectroscopy on the non-silent states (Ni-C and Ni-L), the proposed mechanism of the oxidation of H_2 in [NiFe]-hydrogenase was determined (Figure 2.1).[15, 31, 38-47]

The first half of the catalytic cycle (Ni-SI_a, Ni-H_2, Ni-3, Ni-R) is EPR silent[32, 48] and more stable in the singlet state than the triplet state.[49-51] The oxidation states of the metals throughout most of the catalytic cycle are widely accepted, with Fe (II) remaining in the low spin oxidation state throughout catalysis,[48, 52, 53] and the oxidation state of the Ni center fluctuating, as shown in Figure 2.1 and described below.

First, H_2 binds to the empty active site (Ni-SI_a), coordinating exclusively to the Ni center (Ni-H_2).[49, 50] Then, one of the hydrogen atoms moves to the bridging position between the metals as a hydride, while the other hydrogen acts as a hydride coordinated to the Ni center, causing an oxidization from Ni (II) to Ni (IV).[48] This Ni-coordinated hydride then reduces the Ni (IV) to Ni (II), and transfers as a proton to the terminal Cys546 residue, forming the crystallographically resolved Ni-R intermediate.[40] A proton/electron dissociation then occurs from Ni-R, the proton from the Cys546 leaving the active site via a hydrogen bonding network concurrent with oxidation from Ni (II) to Ni (III) to generate the Ni-C intermediate. The bridging hydride in Ni-C then reduces Ni (III) to Ni (I) with a transfer of the resulting proton to the Cys546 residue (Ni-L). Finally, Ni-SI_a is regenerated via a second proton/electron dissociation from the Ni-L intermediate, resulting in an oxidation from Ni (I) to Ni (II).

However, there are some questions remaining regarding the mechanism of catalysis. Ryde and coworkers[48] studied the catalyst regenerations steps, Ni-C, Ni-L, and Ni-SI$_a$ to determine whether the reaction proceeds through the Ni-L state or through some other mechanistic pathway to convert from Ni-C to Ni-SI$_a$. This study found that the energetic barrier (21.3 kcal/mol) for the transition from Ni-C to Ni-L was too high when compared to the experimental net rate of the reaction, which translates to approximately 12.4 kcal/mol based on transition state theory.[48, 54, 55]

A new pathway was proposed where the proton and electron dissociation occurs in separate steps instead of as a pair (as shown in Figure 2.1): (1) the Ni-C intermediate oxidizes to $[\text{Ni-C}]^{4+}$ via electron ejection, (2) the µ-H migrates to the Cys-546 residue where the electrons from the H^- reduce the $[\text{Ni-C}]^{4+}$ to the $[\text{Ni-L}]^{2+}$ intermediate, followed by (3) H^+ dissociation to regenerate the Ni-SI$_a$ intermediate. The barrier associated with this proposed pathway (steps 2 and 3) was found to be 13.9 kcal/mol relative to $[\text{Ni-C}]^{4+}$. Based on this, it was hypothesized that the reaction would occur be **Ni-C → $[\textbf{Ni-C}]^{4+}$ → $[\textbf{Ni-L}]^{2+}$ → Ni-SI$_a$** as opposed to: **Ni-C → Ni-L → Ni-SI$_a$** (Figure 2.1),[48] completely negating the formation of the Ni-L intermediate.

However, there are still questions to be answered regarding these catalyst regeneration steps. The likelihood of Ni-C to proceed through a redox electron ejection versus a hydride transfer is one avenue of study addressed in the current work. Additionally, the Ni-L intermediate has been previously observed experimentally,[38, 39, 41-43, 45-47, 56] albeit in very specific conditions, so investigation into the presence of the Ni-L intermediate in the catalytic mechanism is also an open question.

Computation has often been used to investigate [NiFe]-hydrogenase because of the difficulty associated with studying this catalysis experimentally due to the many EPR silent states involved in catalysis. Electronic structure methods are ideal for studying bond making and breaking processes, but in large biological systems, this is not always possible due to computational cost.[3, 57] Additionally, the presence of two transition metals in the active site as well as three FeS clusters in the surrounding environment add an additional level of difficulty; transition metal character is not adequately captured without the use of electronic structure methods.[6, 58] Therefore, one must instead create a model to best mimic the enzyme while utilizing methods that are robust enough to describe the chemistry happening in the active site. This can be accomplished using DFT methods, which are well suited for studying complex reaction mechanisms, chemical reactivity, and catalytic reaction kinetics.[59]

In computational chemistry, accuracy is usually assessed by comparison of specific chemical properties to experimental or highly accurate theoretical results, such as coupled cluster (CC) calculations.[6] However, for practical calculations for catalysis, the accuracy is also dependent upon the quality of the model, or how well it captures the important chemical details of the system. Additionally, the chemistry of 3d transition metals (such as Fe and Ni) and the catalytic processes associated with those metals pose challenges with respect to practicality of the model utilized and the quality of the electronic structure methods. This creates a fine balance between accurately modeling a system while utilizing an appropriate level of theory that is effective but not impractical or computationally expensive.[59]

To create a working model of [NiFe]-hydrogenase, choices must be made in order to balance the size of the model with the character of the surrounding environment. One method of doing this is to base the working model on an experimentally resolved crystal structure, isolating the parts of the enzyme that are most likely involved in catalysis, and representing the rest of the enzyme with some sort of potential or treated with a lower accuracy method.[56, 58, 59]

One choice that is usually made is to exclude the backbone structure of the amino acid residues, effectively truncating the model at the various amino acid side chains. This method was used in many studies with DFT, where the active site model was cut at the carbon adjacent to the carbonyl group in the amino acid residue.[51, 60, 61] Models used for studies with wavefunction methods were even smaller, cut at the carbon adjacent to the Cys S, or including just a S-H group to represent the Cys residue.[6, 49, 50, 62] However, these models give a potentially incomplete view of the influence of other residues on the geometry of the active site and the energetics of the catalysis, losing potentially important features.

The goal of this work is to learn information about the mechanism of the reaction and understand how the surrounding enzyme environment and electronic structure influences the catalytic reaction of [NiFe]-hydrogenase. This is accomplished through study of possible redox pathways, and through analysis of the influence of choices made in the creation of the models and the computational results on this system, from an energetic and geometric perspective. This is achieved by using models of increasing size, from 30 atoms to 150 atoms, treated at the DFT level to determine the influence of degree of constraint, exclusion/inclusion of certain residues, and choice of crystal structure as a starting point for building these models.

2.2 Computational Details

The reaction profile of hydrogen oxidation and structure of [NiFe]-hydrogenase was studied with DFT using the Gaussian 09 suite version E01.[63] The BP86[64] functional was used for these calculations, as previous work determined it was one of the best functionals when compared to CCSD and Complete Active-Space Second-Order Perturbation theory (CASPT2).[6] Ni-SI$_a$, Ni-H$_2$, Ni-3, Ni-R were studied using the restricted BP86 formalism, while the two doublet states, Ni-C and Ni-L, were studied with the unrestricted BP86 formalism. All calculations were run using the def2-TZVP[65, 66] basis set.[51]

For all calculations, quadratic convergence (XQC) was used for the convergence of the self-consistent field (SCF) cycles, and symmetry was turned off. Grimme's D3 dispersion correction[4] was also included. The polarizable continuum solvation model[67] (PCM) was applied with $\varepsilon = 4$ to simulate the surrounding enzyme environment.[56, 58] Frequency calculations were also performed to obtain thermodynamic corrections, and any frequencies less than 50 cm^{-1} were shifted to correct the fictitious large contribution caused by small frequencies due to the harmonic oscillator approximation.

The free energies of the reaction intermediates were calculated relative to Ni-SI_a. For the proton/electron dissociation steps (Ni-C and Ni-L), energetic corrections were computed using a comparison to the standard hydrogen electrode (SHE) where $G(H^+/e^-) = \frac{1}{2}G(H_2)$ and the Nernst equation to include the pH effect at physiological conditions (pH=7). The free energy for the Ni-C and Ni-L intermediate was calculated using

$$\Delta G_{rxn} = G_{Ni-C/Ni-L} - G_{Ni-SI_a} - \frac{1}{2}G(H_2) - 2.303RT \times pH.^{51} \tag{2.1}$$

Multiple crystal structures were tested, chosen from varied organisms, reduction states, and crystallographic resolution values. Three of the crystal structures tested, 4U9H (0.89Å resolution),[40] 1H2R (1.40Å resolution),[31] and 4UD2[68] (2.30Å resolution) belong to the *Desulfovibrio* genus. The other crystal structure tested, 5A4M (1.70Å resolution),[69] was isolated from *E. coli*. These crystal structures were used as the starting geometries for the calculations, meant to preserve certain aspects of the experimentally found properties.

$$E_{anode} = \frac{-\Delta G_{red}}{nF} - 4.44\mathrm{V} \tag{2.2}$$

$$\Delta G_{red} = G_{reduced\ product} - G_{oxidized\ reactant} \tag{2.3}$$

In order to explore the catalyst regeneration mechanism, the redox potential was calculated for the electron ejection from the Ni-C and Ni-L intermediates compared to the redox potential of the proximal $[4Fe\text{-}4S]^{2+/+}$ cluster to determine whether the electron ejection would be a spontaneous process using the computational methods outlined above. The reduction potential (E_{anode}) of the electron ejection was calculated using equation 2 where ΔG_{red} (eq. 2.3) is the computational energy difference between the reduced and oxidized intermediates, n is the number of electrons involved in the redox reaction, F is Faraday's constant, and the potential is set relative to the accepted value for the hydrogen electrode by subtracting the value of the absolute electrode potential of the hydrogen electrode, 4.44 V.[70, 71] We then determined the cell potential of the reaction by taking the difference between the cathode, in this case the redox potential of the proximal [4Fe-4S]$^{2+/+}$ cluster from the literature (-0.300 V),[18, 39] and the anode, or the redox potential of the electron ejection step. Model ***2C*** (Figure 2.2) was used to study this phenomenon.

The models tested during this study are portrayed in Figure 2.2 and Figure 2.3, named after their figure labels. Model ***2A*** includes the two metal centers, the three inorganic ligands coordinated to Fe, and the Cys residues are represented by an S atom with a methyl group. Model ***2B*** is similar to model ***2A***, but the Cys residues are represented by an S atom with an ethyl group. Model ***2C*** includes the full amino acid unit for the four Cys residues. This model is capped at both ends of the amino acid, an aldehyde group capping one end, and a primary amide group on the other end. Model ***2D*** expands on ***2C***, including four additional amino acid residues that have potential interactions with the active site inorganic ligands – serine (Ser502), leucine (Leu482), proline (Pro478), and Pro501.[51] All of these models were run with the atoms highlighted in green in Figure 2.2 constrained to preserve the enzyme scaffolding while capturing the environment with solvation.

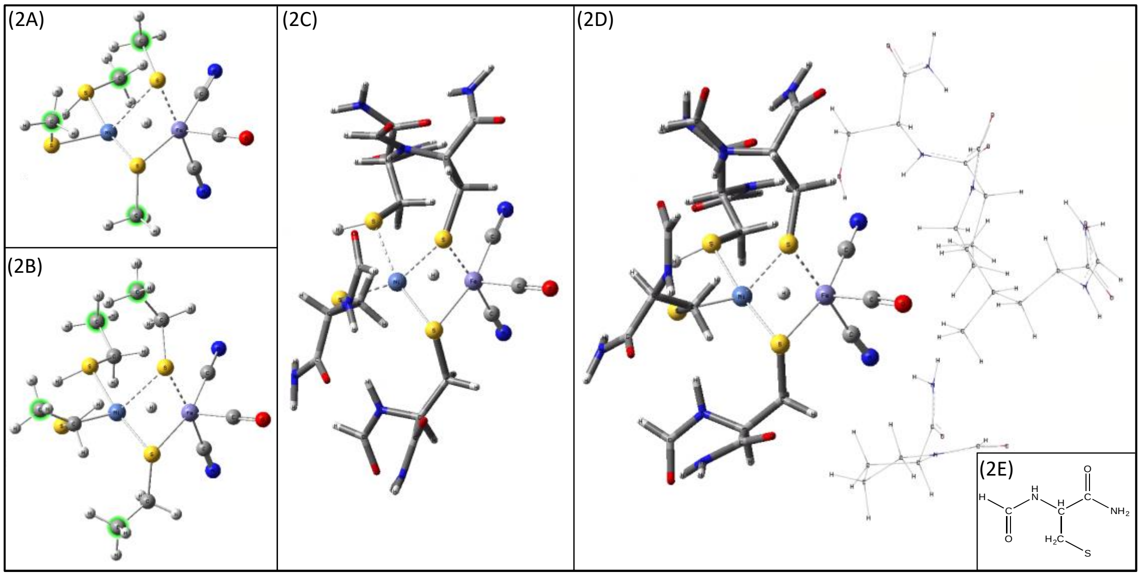

Figure 2.2: The various models of the active site. The highlighted atoms were frozen in the constrained calculations. The end of the chains was capped with an appropriate number of hydrogens. (A) is truncated at the C position adjacent to the Cys S atom. (B) includes an additional C atom in the side chain of the Cys residue. (C) includes the entire Cys residue, and model (D) includes the entirety of (C), as well as four additional amino acids (Ser, Leu, and two Pro). (E) shows the atoms that are constrained for each amino acid in (C) and (D).

In addition to the models tested in Figure 2.2, the degree of constraint was also analyzed for the different models. For the models where the active site was truncated at the second carbon in the Cys chain, there were three variations on degree of constraint tested. The first was shown previously, model ***2B***, where only the carbon on the end of the chain was frozen. Model ***3A*** is constructed the same way as ***2B*** but has both carbons in the Cys residue side chain constrained to the crystal structure geometry. The last is model ***3B***, where the carbon from ***2B*** is frozen in addition to one of the terminal hydrogen atoms. Specifically, the hydrogen atom that is constrained is the one that replaces the carbon position of the amino acid backbone when cut out of the crystal structure. These two models can be seen in Figure 2.3 (***3A*** and ***3B***). The last model system studied is model ***3C*** (Figure 2.3 Model ***3C***); this model is similar to model ***2C*** but an additional constraint has been imposed via constraining the carbon adjacent to the sulfur atoms (Figure 2.3 Model ***3D***) in the active site in addition to the atoms indicated in Figure 2.2 (***2C***).

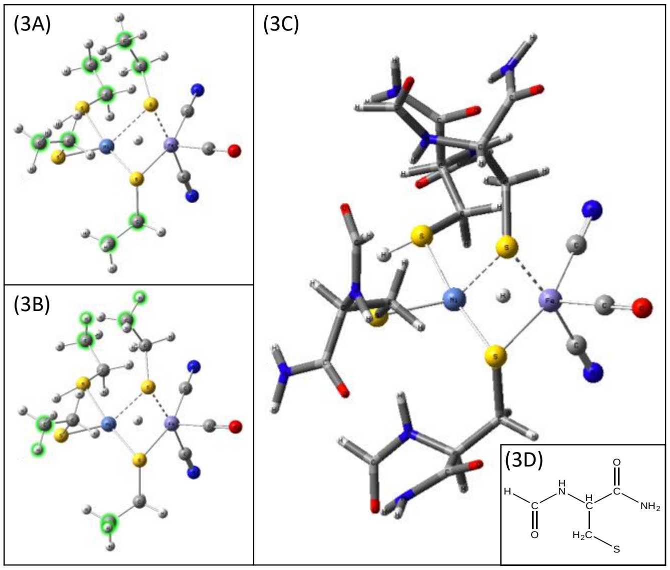

Figure 2.3: Additional active site models with varying degrees of constraint. The highlighted atoms indicated the atoms frozen in the constrained calculations. The end of the chains were capped with an appropriate number of hydrogens. (A) and (B) are built from Figure 2.2 (***2B***), with different degrees of constraint. (C) was built from Figure 2.2 (***2C***), with additional constraints by freezing the carbon adjacent to the S atom. The structure shown in (D) shows the atoms that are constrained for each amino acid in (C).

2.3 Results and Discussion

2.3.1 Redox Catalyst Regeneration Steps

As stated previously, there are questions regarding the catalyst regeneration steps (Ni-C, Ni-L, and Ni-SI$_a$) that have yet to be answered. The literature discussed the possibilities for an alternative pathway where the electron/proton pair dissociation occurs in two separate steps.[48] In order to study this, we calculated the free energy of the redox reaction for three places in the catalytic cycle where oxidation steps could occur in order to determine whether these electron ejections could happen spontaneously, as shown in Table 2.1. The [Ni-H_2] redox intermediate was run as a doublet spin state, and the [Ni-C] and [Ni-L] redox intermediates both show preference to the singlet state over the triplet state.

Table 2.1: Reduction potential (E_{anode}) and cell potential (E_{cell}) of the possible redox pathways indicated in Figure 2.1.

	$E_{anode}\ (eq. 2.2)$	$E_{cell}\ (E_{cathode} - E_{anode})$
$\text{Ni-H}_2 \rightarrow [\text{Ni-H}_2]^{3+} + e^-$	0.194 V	-0.494 V
$\text{Ni-C} \rightarrow [\text{Ni-C}]^{4+} + e^-$	0.075 V	-0.375 V
$\text{Ni-L} \rightarrow [\text{Ni-L}]^{2+} + e^-$	-0.541V	0.241 V

The first reaction, $\text{Ni-H}_2 \rightarrow [\text{Ni-H}_2]^{3+} + e^-$, was hypothesized to be unlikely to occur due to the experimental evidence of the Ni-R intermediate as well as from the inclusion of the Ni-3 intermediate from our study as well as the literature.[48] The results of the calculation indicate a nonspontaneous reaction, with E_{cell} = -0.530 V, meaning the reaction will most likely proceed from Ni-H_2 to Ni-3 instead of an electron ejection. The next reaction tested, $\text{Ni-C} \rightarrow [\text{Ni-C}]^{4+} + e^-$, was also found to be nonspontaneous with E_{cell} = -0.375 V, indicating that the pathway proposed by Dong et al. would most likely not occur in the enzyme without external influence.[48]

The last reaction studied, $\text{Ni-L} \rightarrow [\text{Ni-L}]^{2+} + e^-$, was calculated to be spontaneous, E_{cell} = 0.030 V. This implies that to regenerate the Ni-SI_a state, the proton/electron pair dissociation happens in separate steps, with the electron ejection happening prior to the proton dissociation. For clarity, the reaction profiles discussed below will only include the Ni-L intermediate, but mechanistically the catalytic cycle would most likely proceed as $\mathbf{Ni\text{-}L} \rightarrow [\mathbf{Ni\text{-}L}]^{2+} + \boldsymbol{e}^{-} \rightarrow \mathbf{Ni\text{-}SI_a} + \boldsymbol{H}^{+}$.

2.3.2 Crystal Structure Independence

The next aspect of the [Ni-Fe]-hydrogenase active site we examined was the effect of the crystal structure. We performed this by studying the reaction profile for the 4U9H (blue), 4UD2 (green), 5A4M (red), and 1H2R (gold) crystal structures to determine if there are any major energetic differences between each structure. The results are shown in Figure 2.4, plotted in terms of change in free energy (in kcal/mol) relative to the Ni-SI$_a$ state as a reaction profile. Each crystal structure was truncated and constrained as shown in model ***2B***, where the cysteine residue is represented as SCH_2CH_3 with the carbon in the β position to the S atom frozen.

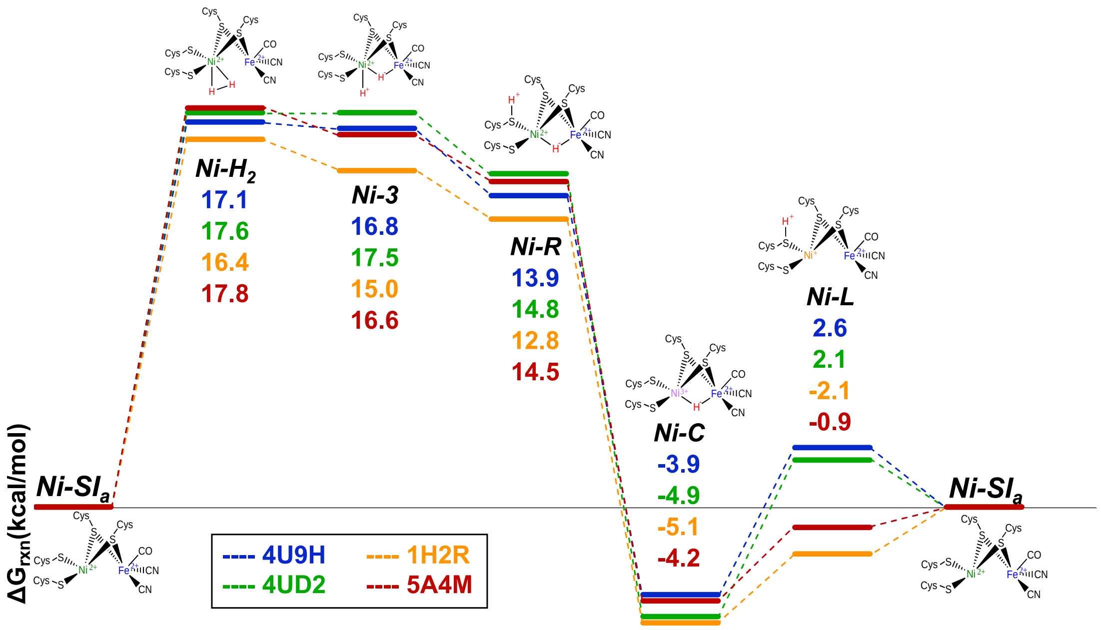

Figure 2.4: Comparison of 4U9H (blue), 4UD2 (green), 1H2R (yellow), and 5A4M (red) crystal structures, in kcal/mol set relative to Ni-SI$_a$ using the model with the carbons at the end of each Cys side chain frozen as seen in Figure 2.2 (***2B***).

In Figure 2.4, we can see that, with the exception of the Ni-L geometry, the largest energy differences between the intermediates are less than 2.6 kcal/mol, indicating that choice of crystal structure geometry has minimal effect on calculation starting point. The energetic stability in the reaction profile indicates that the free energy is independent of the crystal structure chosen as the start for the calculation. Additionally, the energy difference from the highest energy intermediate (Ni-H_2) to the lowest energy intermediate (Ni-C) is 21.1 (4U9H), 22.4 (4UD2), 21.5 (1H2R), and 22.0 (5A4M) kcal/mol. These energies are within a span of 1.3 kcal/mol, further indicating that the reaction profile is not dependent upon which crystal structure is chosen.

The data for the Ni-L intermediate shows energies that vary by up to 4.6 kcal/mol, so the literature was consulted to help determine which crystal structure would prove the best selection. In Dong et al., it was determined that the free energy difference between Ni-C and Ni-L was approximately 5.4 kcal/mol;[48] these Quantum Mechanics/ Molecular Mechanics (QM/MM) calculations were performed on a much larger system where all chemical groups within 4.5 Å of the active site (819 atoms) were treated in QM region of the calculation. Energies were extrapolated to the B3LYP/def2QZVPD functional and basis set, therefore we will use this as a benchmark for the energy difference between Ni-C to Ni-L. In the data shown in Figure 2.4, the Ni-C to Ni-L energy changes were 6.5 (4U9H), 7.0 (4UD2), 3.0 (1H2R), and 3.3 (5A4M) kcal/mol. The energy difference observed in the 4U9H geometry most closely matches the energy difference in the literature, however the other crystal structures provide different values by at most 2.4 kcal/mol. This indicates relative consistency in the net energy change between the Ni-C and Ni-L intermediates across all structures, which is interpreted as choice of crystal structure having minimal effect on the energetics of catalysis.

From this information, the 4U9H crystal structure was chosen as the starting geometry for subsequent calculations, which is crystal structure isolated with hydrogens resolved in the active site for the Ni-R intermediate.[40] Additionally, we have shown that the choice in crystal structure does not greatly influence the reaction, and that the 4U9H crystal structure had only the smallest deviation from to the literature value of Ni-C to Ni-L energy difference.

2.3.3 Geometric Results for Increasing Model Size

In order to determine the best model to use to accurately describe the energetics and geometry of the reaction with respect to the enzyme scaffolding, the active site model was expanded from 4U9H crystal structure. In addition to providing information about the best model to use, we can also extrapolate structural information regarding which features play major roles in catalysis. For example, some of the models tested show local active site geometry deviations which can produce nonminimal energetic changes. This phenomenon is discussed in this section.

The geometry of the Ni-R intermediate, which was resolved crystallographically with H atoms, had deviations in the bond lengths for the Ni-S bond (Table 2.2) that are only found in some models that do not include the entire amino acid backbone.

Since the crystal structure was isolated in the Ni-R state, we can compare the geometric parameters from our calculations to the values determined experimentally. For most of the bonds in the local structure of the active site $[(RS)_2Ni\mu(SR)_2Fe(CO)(CN)_2]$ where SR=Cys, the deviations are less than 0.03 Å.

Table 2.2: Bond lengths of the highlighted Ni-S bond in the Ni-R intermediate for various models of the [NiFe]-hydrogenase active site. Selected values that deviate from the data set are bolded in red. These are ordered by increasing model size and degree of constraint.

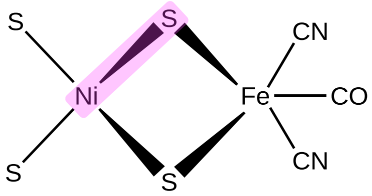

Model	Ni-S Bond Length at Ni-R (Å)	ΔG_{rxn} at Ni-R (kcal/mol)
4U9H	2.54	N/A
2A	**3.15**	5.98
2B	**2.78**	13.86
3A	**2.94**	-3.64
3B	2.68	4.31
2C	2.69	7.07
3C	2.63	5.62
2D	2.69	4.74

However, the Ni-S bond mentioned does deviate more drastically, which is visually apparent in Figure 2.2 (***2A***) as well as quantitatively indicated in Table 2.2. Upon investigation into the more constrained models - specifically the ***2A*** and ***3A*** geometries where the C atom adjacent to the cysteine residue S atom is frozen - we see an increase in bond lengths of 0.4 Å or larger. When visualized, it becomes clear that this phenomenon is caused by the bridging S atom swinging towards the Fe center forming a pseudo-octahedral geometry. This is also seen in the ***2B*** model.

Analyzing the degree of constraint can help illuminate what effects these constraints offer. In model ***3B***, the additional constraint imposed by freezing the hydrogen atom actually decreases the bond length of the Ni-S bond to 2.68 Å (from 2.78 Å in ***2B*** and 2.94 Å in ***3A***). This bond length is in good agreement with the larger models tested, indicating a sensitivity to the choices made in model curation. Specifically, constraints placed too close to the active site atoms cause unphysical distortions of the geometry, but certain constraints further away from the active site atoms, as in model ***3B***, actually correct the geometric distortions without expanding the model.

The other model tested with increased constraint was model ***3C***, which had a bond length closest to the crystal structure value, differing by only 0.09 Å. This implies that when the model is expanded to include the full amino acid residue, the elongated Ni-S bond is not observed regardless of the degree of constraint of the C atoms adjacent to the Cys S atoms.

Another metric used to analyze the geometries of the various models tested are the τ parameters to quantify the geometric distortion for the system of study. In this work, the τ_4[72] and τ_5[73] parameters were utilized to describe the level of distortion of the geometry centered at the Ni atom. These parameters were calculated by:

$$\tau_4 = \frac{360 - (\alpha + \beta)}{141} \tag{2.4}$$

$$\tau_5 = \frac{|\beta - \alpha|}{60} \tag{2.5}$$

Where α and β are the largest bond angles in the portion of the system being analyzed. The τ_4 parameter was used to describe the four-coordinate geometry consisting of $[(RS)_2Ni\mu(SR)_2]$ for all intermediates; the τ_5 was used to describe the five-coordinate geometry $[(RS)_2Ni\mu(H)(SR)_2]$ for the Ni-3, Ni-R, and Ni-C intermediates. For the τ_4 parameters, 0 indicates a square planar geometry while 1 indicates a tetrahedral geometry. The denominator of eq. 2.4 was chosen as 141 in order to allow the value of 1 to be assigned to a tetrahedral geometry; assuming a perfect tetrahedral bond angle of 109.5°, the difference of the sum of these angles to 360° is 141. For the τ_5 parameters, 0 indicates a square pyramidal geometry while 1 indicates a trigonal bipyramidal geometry.

Based on this data, there is not much deviation in the local geometry of the Ni center. Most of the τ_4 parameters (Table 2.3) indicate a geometry that is in between a square planar structure and a tetrahedral structure, whereas the τ_5 parameters (Table 2.4) show a preference towards a square pyramidal geometry with a slight distortion. The few deviations seen in the data exist in the smaller model sizes: the Ni-SI_a intermediate for model ***2B*** has a smaller τ_4 parameter value than the rest of the data set, deviating by 0.11 from the average value (0.46) for Ni-SIa across all models tested.

Table 2.3: Values of τ_4 parameters for all models including each intermediate involved in catalysis as depicted in Figure 2.1. Selected values that deviate from the data set are bolded in red.

Model	**Intermediate**					
	Ni-Si$_a$	**Ni-H$_2$**	**Ni-3**	**Ni-R**	**Ni-C**	**Ni-L**
2A	0.53	0.51	0.51	0.51	0.46	0.49
2B	**0.35**	0.49	0.55	0.53	0.56	0.47
3A	0.51	0.54	0.54	0.54	0.53	0.49
3B	0.47	0.52	0.53	0.54	0.55	0.52
2C	0.43	0.51	0.54	0.57	0.53	0.53
3C	0.50	0.54	0.54	0.55	0.52	0.51
2D	0.43	0.52	0.53	0.56	0.53	0.54

Table 2.4: Values τ_5 parameters for all models including each intermediate involving a bridging μ-H involved in catalysis as depicted in Figure 2.1. Selected values that deviate from the data set are bolded in red.

Model	**Intermediate**		
	Ni-3	**Ni-R**	**Ni-C**
2A	0.22	**0.01**	0.16
2B	0.14	0.12	0.11
3A	0.13	**0.01**	0.15
3B	0.17	0.12	0.12
2C	0.18	0.09	0.19
3C	0.18	0.14	0.20
2D	0.20	0.11	0.18

Additionally, the inclusion of the μ-H influences the geometry for the Ni-R intermediate for models ***2A*** and ***3A***. For both models, the τ_5 parameter is smaller than all other models, indicating a geometry much closer to square pyramidal than the other models tested. The most likely cause of this deviation is the constraint of the C atom adjacent to the S atom in the cysteine residues. In model ***3C***, however, that same C atom is frozen while including the entire amino acid residue. This results in a much larger increase in the τ_5 parameter – 0.01 in ***2A*** and ***3A*** compared to 0.14 in ***3C*** - indicating that the geometric distortions from truncating the amino acid and constraining the model at the C atom adjacent to the S atom are corrected when the entire cysteine residues are included in the calculation.

In order to get reasonable geometries compared to the experimentally determined crystal structure, enough of the active site must be included. It was shown that some smaller models (***2A***, ***2B***, ***3A***) do not adequately represent the active site geometry. As can be seen with the models where the levels of constraint were analyzed, the local structure of the active site is sensitive to degrees of constraint imposed for model sizes that do not include the entire amino acid residue. This effect can be negated by constraining hydrogen atoms as seen in model ***3B***. This leads to the conclusion that the amino acids are important to the stabilization of the local geometry of the active site in this enzyme, but the local geometry can still be adequately captured by smart choices in atom constraint.

2.3.4 Energetic Results for Increasing Model Size

We have found that inclusion of certain features of the active site and the subsequent choices in constraint influence the $[(RS)_2Ni\mu(SR)_2Fe(CO)(CN)_2]$ structure. As we will show in this section, the influence of these geometric distortions does affect the energetics of the reaction. Additionally, we find that the inclusion of additional amino acid residues (specifically the ones in model ***2D***) does not influence the energies. From all this data, we found that as long as the structure of the $[(RS)_2Ni\mu(SR)_2Fe(CO)(CN)_2]$ core is maintained, the energies do not change, meaning the local active site structure has the largest influence on the function and activity of [NiFe]-Hydrogenase.

In Figure 2.5, we can see the reaction profile for the active site models that have only the end of each amino acid chain frozen, which includes models ***2A***, ***2B***, ***2C***, and ***2D*** (indicated in Figure 2.5). The energetics for these for models were plotted with respect to the Ni-SI_a intermediate, and follows the mechanism shown in Figure 2.1.

Between model ***2A*** and ***2B***, a large energy difference can be seen. However, once the active site is expanded to include the entire cysteine residues (models ***2C*** and ***2D***), the reaction profile becomes consistent with model ***2A***, showing that energetically, model ***2B*** does not adequately capture the character of the active site during catalysis. This is further proven by the fact that the intermediate energies for ***2B*** are too high when compared to the experimental net rate of the reaction.[48, 54, 55]

When the active site is expanded from ***2C***, we include four amino acid residues with potential interactions with the inorganic ligands bound to the Fe center (model ***2D***). We see energetic results that correspond with model ***2C*** and can conclude that the four amino acid residues do not influence the free energy profile. This indicates the lack of electronic or long-range contributions to the active site from these residues that is not already captured by the solvation model.

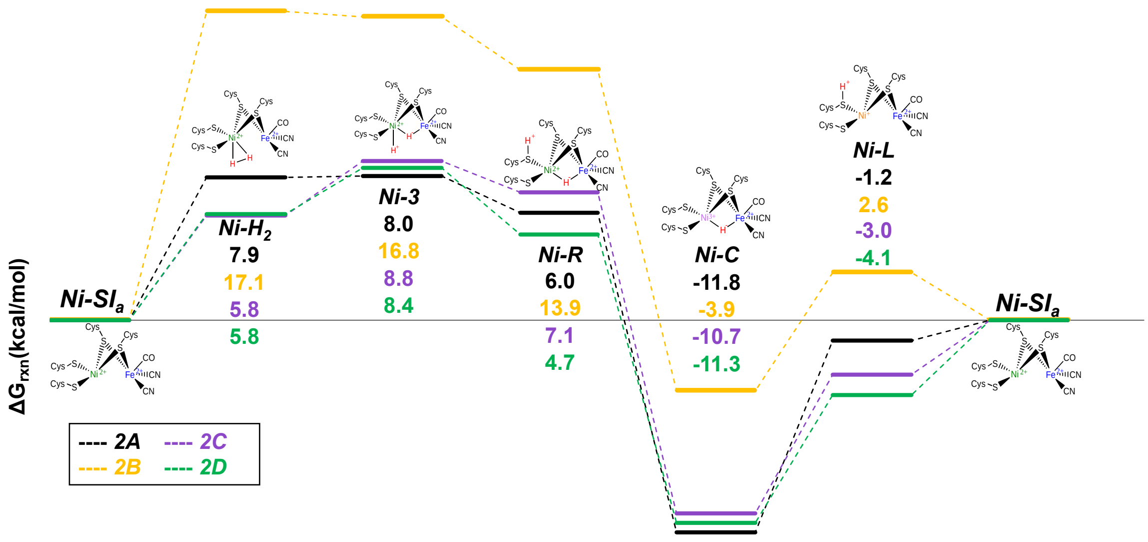

Figure 2.5: Comparison of various model sizes using the 4U9H crystal structure with frozen carbons at the ends of cysteine side chains as seen in Figure 2.2.

One very important detail of the reaction profile is the inclusion of the Ni-3 intermediate. In the literature,[51] this intermediate is often overlooked because it is assumed to have no influence the reaction since the energy of the intermediate is within 1 kcal/mol of the previous step, Ni-H_2. In our results, this trend is true for models ***2A*** and ***2B*** (as seen in Figure 2.5), with differences between the Ni-H_2 and Ni-3 intermediate at 0.1 kcal/mol and 0.3 kcal/mol respectively. However, upon expansion of models to where the entire amino acid residue is included (models ***2C*** and ***2D***), this is no longer the case - the Ni-3 intermediate is approximately 3 kcal/mol higher in energy than the previous step and is the highest energy intermediate. This phenomenon was only captured when a large enough model was used to describe this reaction, indicating the importance of model size in providing mechanistic insight into the catalytic process. Other groups have recently included this intermediate into the study of this mechanism where it was hypothesized to be a hydride bound to a Ni (IV) center with the μ-H bound between the Fe and Ni metals. This was shown with Density Matrix Renormalization Group (DMRG)-CASPT2 calculations.[48]

Additionally, energies for ***2C*** and ***2D*** only differ by 0-2.4 kcal/mol for all the intermediates; the peak to trough energy (P2T) difference, which is between the highest energy intermediate (Ni-3) and the lowest energy intermediate (Ni-C), is 19.5 kcal/mol for ***2C*** and 19.7 kcal/mol for ***2D***, indicating that the reaction profile for these two models are almost identical.

Based on the geometric and energetic data discussed to this point, we can say that models **2C** and **2D** are examples of models that adequately represent the local structure of the active site and are the best models to use without considering degree of constraint. This is due to the small deviations between the energies of the intermediates, the consistency in peak to trough energy differences, and the structural information from Section 2.3.3. We can further infer that the inclusion of the Cys amino acid backbones adds additional long-range interactions that were not captured in the smaller models, supporting the conclusion that the main influence on the catalytic function of the enzyme is the structure of the active site.

2.3.5 Effect of Degree of Constraint on Energy

The models shown in Figure 2.3 were also energetically analyzed to determine the effect of additional constraints of the amino acid residues. We have shown that certain constraints, specifically freezing the C atoms adjacent to the S atoms in the cysteine residues, impact the geometry of the local structure of the active site. In this section, we will discuss the impact the degrees of constraint studied on the energy profile of catalysis. We found that certain constraints (model ***3B***) cause the [(RS)$_2$Niμ(SR)$_2$Fe(CO)(CN)$_2$] structure to match the already discussed appropriate models of the active site (models ***2C*** and ***2D***), and this phenomenon is also reflected in the energetic data, further supporting our conclusion that the main factor that influences the catalytic activity of [NiFe]-hydrogenase is the structure of the core active site. This data is shown in Figure 2.6.

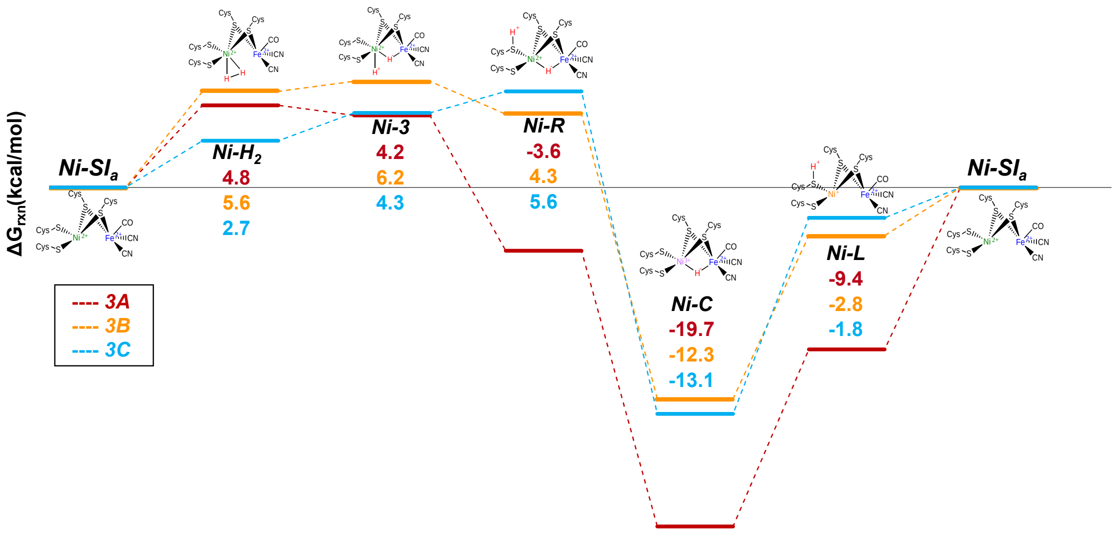

Figure 2.6: Comparison of various model sizes and degrees of constraint using the 4U9H crystal structure with atoms frozen as seen in Figure 2.3.

Model ***3A***, when compared to the analogous model ***2B***, corrects the energy shift observed in Figure 2.5. However, freezing the C atom adjacent to the cysteine S atom seems to overcorrect in this case – the Ni-R, Ni-C, and Ni-L intermediates are 9.5, 8.7, and 5.8 kcal/mol lower in energy than the average energies for models ***2C*** and ***2D*** (5.9, -11.0, and -3.6 kcal/mol for Ni-R, Ni-C, and Ni-L, respectively). Additionally, rather than Ni-3 being the highest energy intermediate, Ni-H$_2$ was found to have a peak to trough energy difference of 24.5 kcal/mol, approximately 5 kcal/mol higher than the corresponding energy for models ***2C*** and ***2D***. This leads us to believe that this model of the active site, while within the range indicated from the experimental rate,[50] does not adequately represent the energetics of the reaction.

While models ***2A*** and ***3A*** struggle to describe the active site due to the small model size, the choice of constraining the C atom at the end of the SCH_2CH_3 chain with an adjacent H atom seems to appropriately correct both the energetics and geometry of the active site. As shown from the results in section 2.3.3 model ***3B*** does not show the distortion of the Ni-S bond length in Ni-R that is seen for models ***2A***, ***2B***, and ***3A***, and does not show deviation within the τ parameter datasets.

Energetically, this data matches very nicely with the data shown in section 2.3.4 for models ***2C*** and ***2D***. For ease of reference, model ***3B*** will be compared to model ***2C,*** as that is the smallest model that has been shown to have reasonable energetic and geometric data at this point. The energy values for each intermediate in ***3B*** when compared to ***2C*** differ by 0.2-2.8 kcal/mol, which is the same approximate range as the values discussed previously. Additionally, the P2T energy difference for ***3B*** is 18.5 kcal/mol, within 1 kcal/mol of the value found for ***2C***. There is very good agreement between models ***2C*** and ***3B***, which leads to the conclusion that one must either include the entire residue for the active site cysteines or make correct choices in constraints to appropriately describe the active site geometrically and energetically. This is due to catalytic cycle sensitivity to active site geometry, so even without the amino acid residues, model 3B is able to properly represent the active site.

The last model shown in Figure 2.6 is model ***3C***, which is analogous to ***2C*** but with extra constraints included by freezing the C atom adjacent to the cysteine S atom. The energies of intermediates Ni-R, Ni-C, and Ni-L are in good agreement between ***2C*** and ***3C***, differing by 1.2-2.4 kcal/mol. However, the first two intermediates, Ni-H_2 and Ni-3, deviate by 3.1 and 4.5 kcal/mol respectively, with ***3C*** being lower in energy. This causes a different intermediate to become the highest energy: for model ***3C*** this is Ni-R, but for most of the other models tested the highest energy intermediate is Ni-3. Model ***3C*** is the only one exhibiting this character, indicating that the extra constraint does impact the reaction profile in unexpected ways even though the Ni-R/Ni-C P2T energy difference (18.7 kcal/mol) is within the range of the other models tested.

When the additional carbon constraint was added to model ***3A***, a net decrease in energy for the reaction profile was observed, providing an explanation for the decreased energies for the Ni-H_2 and Ni-3 intermediates calculated from model ***3C***. While we have shown that increasing the size of the model by utilizing the entire cysteine amino acid residues as opposed to just the truncated side chain (SCH_3 or SCH_2CH_3) corrects for various unphysical phenomenon, it is possible that not all these effects were corrected upon active site expansion with model ***3C***. This model was able to describe the Ni-R, Ni-C, and Ni-L states consistently with respect to model ***2C***, but the decrease in energy for the first two states is most likely a product of the increased rigidity of the active site.

Constraints adjacent to the active site appear to cause a decrease in the free energy of the intermediates regardless of the size of the model used. This can be seen in model ***3A*** and model ***3C*** in Figure 2.6. However, the additional constraint added to the end of the chain used in model ***3B*** seems to represent the energetics of the active site in a way that is consistent with the larger models ***2C*** and ***2D***, with both the comparable peak to trough energy differences and the small deviations in the free energies of the intermediates involved in catalysis.

Given all the results discussed, we can say the two best models to describe catalysis in [NiFe]-hydrogenase are models ***2C*** and ***3B***. While curating appropriate theoretical models is important with regards to finding a balance between computational cost and accuracy,[59] we are also able to extrapolate information about the structure/function relationships for this enzyme. We found that slight changes in the active site structure $[(RS)_2Ni\mu(SR)_2Fe(CO)(CN)_2]$ cause changes to the reaction profile, and that the solvation model captures the enzyme environment well enough, as indicated by the lack of energetic changes found from the inclusion of additional amino acid residues

2.4 Conclusion

[NiFe]-hydrogenase was studied computationally using DFT with implicit solvation to better understand the mechanism of the catalytic cycle and elucidate information about the active site that influences catalysis. This was done by calculating the redox potential of certain intermediate steps, comparing different models with varying features such as increasing model sizes, inclusion of additional amino acid residues, and degree of constraint, all using models built from experimentally resolved crystal structures.

It was found that the Ni-L intermediate most likely goes through an electron ejection to the proximal $[4Fe\text{-}4S]^{2+/+}$ cluster prior to proton dissociation via a hydrogen bonding network, regenerating the Ni-SI_a catalyst. Choice of crystal structure does not affect the energetics of the reaction profiles, as shown by the results in Section 2.3.2 where four different crystal structures were utilized to create the model of the active site used for the subsequent calculations.

From all the energetic and geometric data discussed in this paper, we have determined that the major factor influencing catalytic activity must be the local geometry of the active site. When building these model systems, enough of the enzyme must be included, or smart choices in constraint must be used, in order to appropriately optimize this local geometry.

The choices made in construction of a model system for the active site were analyzed by comparing geometries and free energies between the models tested in conjunction with the literature. It was found that one must include either the entire amino acid residue or have the appropriate constraints (models ***2C***, ***2D***, ***3B***) to get reasonable geometries of the active site. This trend also holds true through the energetic analysis; correct choices in constraint must be used regardless of how much of an amino acid residue is included, however, the inclusion of the entire residue usually improves results. Models ***2C***, ***2D***, ***3B*** are the best ones to use to study catalysis in [NiFe]-hydrogenase using electronic structure methods.

All of this data points to the overarching conclusion that the structure of the core $[(RS)_2Ni\mu(SR)_2Fe(CO)(CN)_2]$ of the active site mediates the catalytic activity of the active site. Slight distortions in the geometry influence the energetics, meaning that the structure of the active site plays the largest role in enzyme catalysis, and any future attempts to mimic the H_2 oxidizing activity should focus on mimicking the structure of the active site as closely as possible, while also retaining the redox character of the active site.

3. Ni-Fe Hydrogenase – Mutation of Highly Conserved Amino Acid Residues in the Local Environment of the Active Site

3.1 Introduction

The structure and function of the [NiFe]-hydrogenase enzyme were discussed in depth in Section 2.1. Additionally, the mechanism was discussed with regards to the crystal structure (4U9H) by Lubitz et al.,[40] where the bridging μ-H was isolated via X-Ray crystallography (Ni-R, Figure 2.1), as well as the possible electron ejection[48] of the catalyst regeneration steps (Ni-L and $[\text{Ni-L}]^{2+}$, Figure 2.1). Within the structure of the enzyme, there are highly conserved residues in the region surrounding the inner coordination sphere, which is comprised of $[(RS)_2Ni\mu(SR)_2Fe(CO)(CN)_2]$.[8] From the literature based on crystallographic data from *E. coli* Hyd-1 (PDB: 3USE[74]), the highly conserved residues, apart from the four Cys residues, are arginine (Arg509), aspartic acid (Asp574), Asp118, and Glu28.[16]

Interestingly, the Arg509 residue is in a position where the guanidine tail hangs over the active site, causing one of the N atoms to reside within 4.5Å of the metal centers. This distance is favorable for a frustrated Lewis pair (FLP) style mechanism, where the combination of a Lewis acid and a Lewis base cannot form a “traditional” complex due to steric hindrance, however permits other reactions such as H_2 formation and decomposition.[75] For the case of [NiFe]-hydrogenase, the FLP mechanism polarizes the H_2 molecule for heterolytic cleavage through simultaneous binding to the acid, in this case the metal center(s), and the base, the Arg509 residue.[69]

The functionality of the Arg residue was studied by Armstrong and coworkers as this residue, prior to publication of this work, had never been experimentally investigated.[69] The assumed role of the residue was a structural stabilizing one, where one of the guanidine N atoms provides a hydrogen bonding interaction with one of the Fe coordinated CN ligands.[25, 28] It was also thought that the residue was part of a proton transfer pathway,[76] however it is more likely that the conserved Glu28 residue is the starting point for this proton transfer channel.[8, 21, 23]

In this work, three of the conserved residues in the "canopy" hanging over the active site were mutated to observe the effect on catalysis. Arg509 was mutated to a lysine (Lys) residue, Asp118 and Asp574 were replaced by asparagine (Asn), and Asp118 was also replaced by alanine (Ala). The results of the study of the turnover rates for the various mutated enzyme complexes are shown below in Figure 3.1.[69]

It was found that the mutated variants had decreased H_2 oxidation activity – the Lys mutated R509K species showed 0.8% the activity found in the native enzyme. Additionally, the local geometry/inner coordination sphere is preserved regardless of the changes made to the canopy residues.[69] Therefore, an FLP mechanism was proposed where, with transient deprotonation, the Arg509 acts as the strong base necessary for H_2 cleavage.[16] This mechanism also shares similarities with [FeFe] hydrogenases[77] and mimetic enzyme-inspired Ni pincer complexes which utilize pendant amine groups as proton acceptors.[78, 79]

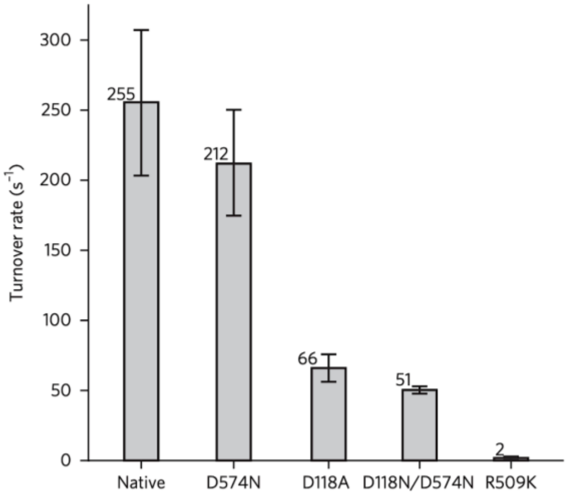

Figure 3.1: Comparison of activities for Hyd-1 and variants investigated in this research. The average turnover rate (s^{-1}) is given for each enzyme, with error bars indicating the standard error of the mean (s.e.m.) of at least 20 repeats with at least 2 different preparations of each enzyme (see also Supplementary Table 3 from the original publication).[69]

Republished with permission of Springer Nature BV from Evans, R. M.; Brooke, E. J.; Wehlin, S. A. M.; Nomerotskaia, E.; Sargent, F.; Carr, S. B.; Phillips, S. E. V.; Armstrong, F. A. *Nat. Chem. Biol.* **2016**, *12*, 46-50. Copyright 2015; permission conveyed through Copyright Clearance Center, Inc

Given the experimental data indicating the importance of the Arg residue, we studied the various effects of the enzyme mutations using computational methods. In Section 2, we carefully investigated the structure and function of [NiFe]-hydrogenases by analyzing the energetics, the geometry of the enzyme environment surrounding the active site, and the mechanism of the catalysis. Using model ***2C*** (Figure 2.2) as the base, we studied the effect of mutating the highly conserved residues in *d. vulgaris* [NiFe]-hydrogenase (PDB: 4U9H), specifically mutations at the Arg479 and Asp123 residues.

3.2 Computational Details

The mutations of the highly conserved residues were studied with the same computational methods outlined in Section 2.2. Gaussian 09 suite version E01[63] was used for the geometry optimizations and frequency calculations using BP86[64]/def2-TZVP.[65, 66] The singlet states (Ni-SI$_a$, Ni-H$_2$, Ni-3, Ni-R) were run with the restricted DFT formalism, while the doublet states (Ni-C and Ni-L) were run unrestricted. Grimme's D3 dispersion correction[4] was included in addition to PCM[67] with $\varepsilon = 4$ to simulate the surrounding enzyme environment.[56, 58] Frequency calculations were also performed to obtain thermodynamic corrections, and any frequencies less than 50 cm^{-1} were shifted. The free energies for Ni-C and Ni-L were calculated with the same formalism in Section 2.2 eq 2.1.

The model used for this work is shown in Figure 3.2, where model ***2C*** from Figure 2.2 was used as the base, and additional amino acid residues were added. The amino acid backbones were constructed as shown in the black box (Figure 3.2), and the atoms denoted with an asterisk show the atoms that were constrained in the calculation. The additional “canopy” amino acids included in our structure are Arg479, Asp123, and Asp544, following the residue numbering scheme of the 4U9H crystal structure. Pro545 was included as well because it is the residue that connects Asp544 to Cys546. Excluding this residue created issues with overlapping frozen coordinates, and as shown in previous work including additional amino acid residues (model ***2D***, Figure 2.2 and Figure 2.5), the residues that do not directly interact with or influence the active site do not cause changes to the resultant energetics, so the additional residue is not expected to affect the study.

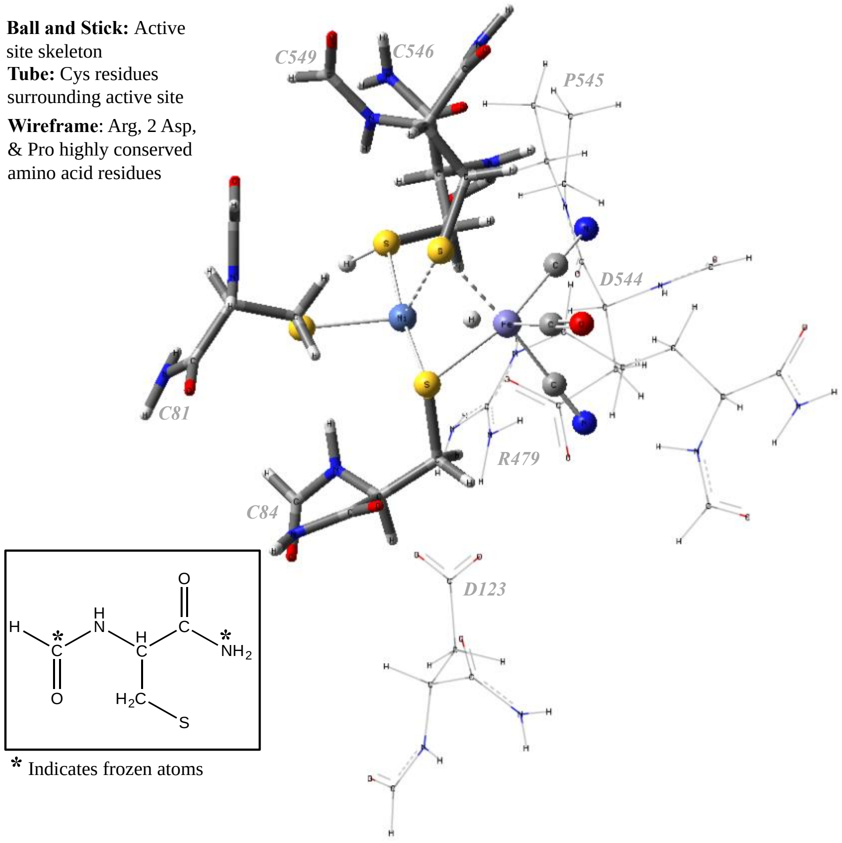

Ball and Stick: Active site skeleton
Tube: Cys residues surrounding active site
Wireframe: Arg, 2 Asp, & Pro highly conserved amino acid residues

* Indicates frozen atoms

Figure 3.2: Model used to study various mutations of the active site of [NiFe]-hydrogenase. The base model for the local active site structure comes from Figure 2.2 model 2C. The additional amino acids included are labelled and the ends are frozen following the scheme indicated by the asterisks on the amino acid backbone shown in the figure.

Two of the mutated enzymes from Figure 3.1 were studied – the Arg mutated to Lys, and the Asp mutated to Ala. These amino acid changes are shown in Figure 3.3. Changing the R479 to K479 preserves the basicity and mostly maintains the length of the side chain. The D123A provides a shorter and hydrophobic side chain, which also limits the possibility of hydrogen bonding to the R479 residue.

This allows for more flexibility of the side chain of R479 to further study the structural influence of this seemingly important residue.

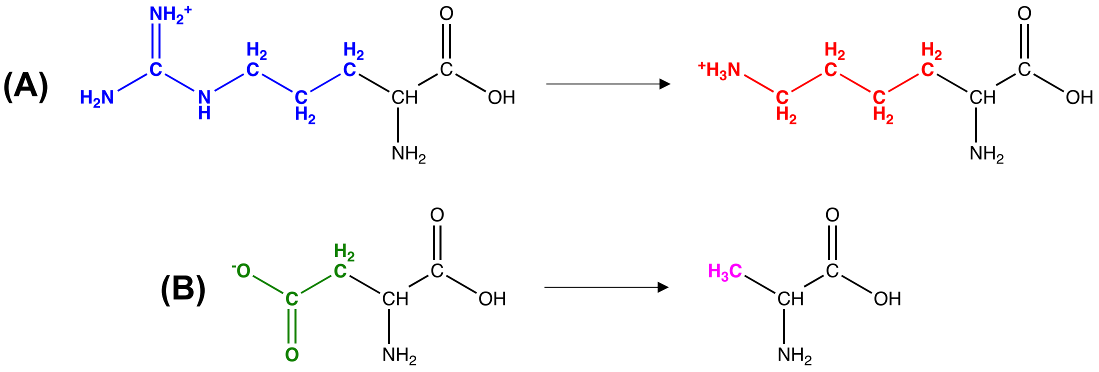

Figure 3.3: The two mutations studied were (A) R479 residue (blue) mutated to a Lys (red) residue and (B) D123 residue (green) mutated to an Ala residue (pink).

Finally, Visual Molecular Dynamics, VMD, 1.9.3[80] was used to create Figure 3.5, where the various mutated models were overlayed to analyze any geometric distortion caused by the changes to the amino acids.

3.3 Results and Discussion

3.3.1 Energetic Comparison of different mutations

We compared the reaction profiles of the wild type enzyme (green), the R479K mutated model (gray), and the D123A mutated model (yellow) (Figure 3.4). The reaction proceeds through the same mechanism outlined in Section 2: H_2 binds to the Ni center in the active site (Ni-H_2) followed by an elongation of the H-H bond resulting in formation of a μ-H (Ni-3). The hydride remaining on Ni then migrates to the S of Cys546 to form the Ni-R intermediate. From here, the proton on Cys546 dissociates as the Ni center oxidizes from Ni (II) to Ni (III) (Ni-C). Following a reduction of the Ni from +3 to +1 and migration of the μ-H as H^+ to the Cys546 residue (Ni-L), the catalyst is regenerated through an electron ejection step ([Ni-L]$^{2+}$) followed by proton dissociation (Figure 2.1).

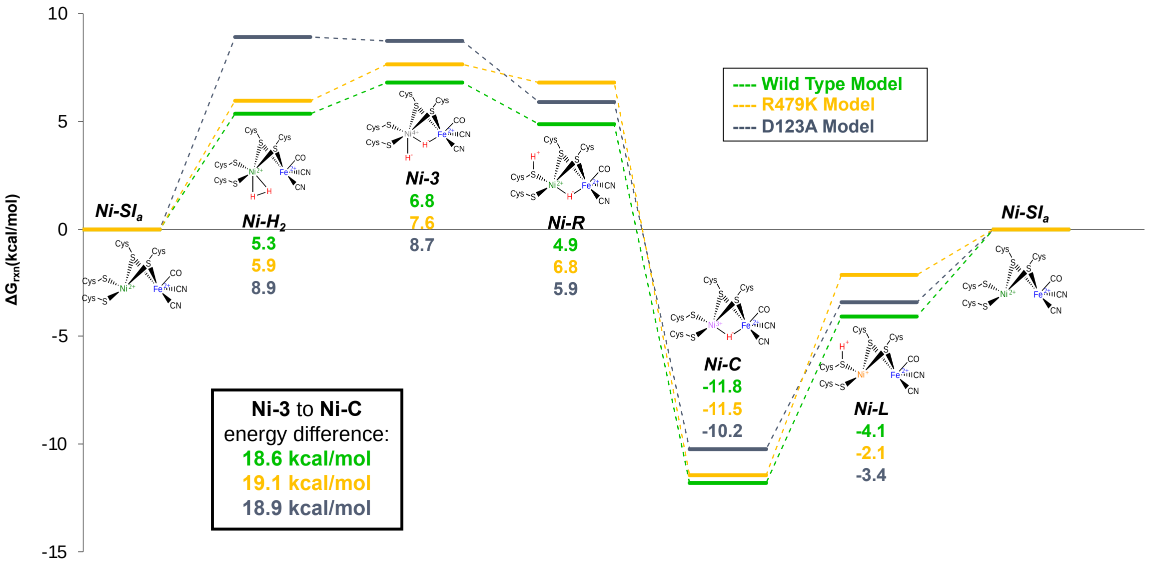

Figure 3.4: Reaction profile of the Wild type (green), R479K (yellow) and D123A (gray) enzyme models, set relative to the bare geometries. Energies reported are in kcal/mol and calculated using the scheme discussed in Section 2.2.

The energetics of the wild type model are in agreement with the work shown in Section 2. The wild type model in the current section has a peak to trough energy of 18.6 kcal/mol. Models ***2C***, ***2D***, and ***3B***, which were determined to be the most accurate models tested for describing the catalysis in [NiFe]-hydrogenase, were found to have peak to trough energies of 19.5 kcal/mol, 19.7 kcal/mol, and 18.5 kcal/mol, showing the inclusion of the additional residues does not change the overall catalytic activity of the enzyme. Additionally, when the energies of the intermediates are compared between the wild type model and the model it was built from (model ***2C***), the energies for the wild type model are all within 2.2 kcal/mol.

When the wild type model and R479K are compared, there are no major energetic deviations found. The energies of all the intermediates when comparing the wild type and R479K models are all within 2 kcal/mol, and the P2T energy for R479K is only 0.5 kcal/mol higher than the wild type at 19.1 kcal/mol. According to these energetic results, the catalytic activity does not decrease upon mutation of the R479 residue (wild type) to a Lys residue (R479K), even though experimental data indicates a shutdown in catalysis with this change.[69] We observe a similar trend when analyzing the D123A model. The P2T energy of 18.9 kcal/mol is consistent with the other energies discussed previously, indicating no change in the catalytic activity compared to the wild type and R479K models.

These results are surprising – experimental data shows that the D123A mutation has 26% and the R479K mutation has 0.8% of the H_2 oxidation activity of the wild type enzyme.[69] Since we see no obvious reasons for this shutdown of catalytic activity through analysis of the energetics, we next turn to the geometric structure of the various models tested.

3.3.2 Geometric Comparison of different mutations

As with the previous section, we use various metrics to quantify the deviations in the geometry of the active site and surrounding amino acid residues. To quantify the distortion about the Ni center, we use the τ_4[72] and τ_5[73] parameters (Section 2.3.3 eq 2.4 and 2.5). The results of the τ_4 parameters are shown in Table 3.1 and

Table 3.2 for the τ_5 parameters. For the τ_4 parameters, 0 indicates a square planar geometry while 1 indicates a tetrahedral geometry. For the τ_5 parameters, 0 indicates a square pyramidal geometry while 1 indicates a trigonal bipyramidal geometry.

Table 3.1: Values of τ_4 parameters for all the intermediates of the three models tested (Figure 3.4).

Intermediates	**Models**		
	Wild Type	**R479K**	**D123A**
Ni-Si$_a$	0.42	0.42	0.42
Ni-H$_2$	0.52	0.52	0.52
Ni-3	0.54	0.55	0.54
Ni-R	0.57	0.57	0.56
Ni-C	0.53	0.59	0.52
Ni-L	0.55	0.56	0.55

Table 3.2: Values τ_5 parameters all the intermediates involving a bridging μ-H of the three models tested as depicted in Figure 3.4.

Intermediates	**Models**		
	Wild Type	**R479K**	**D123A**
Ni-3	0.19	0.18	0.18
Ni-R	0.09	0.10	0.09
Ni-C	0.21	**0.10**	0.15

When we compare the values for each intermediate between the models, we find very few discrepancies with regards to the orientation of the atoms coordinated to the Ni center. For the τ_4 data, only the Ni-C intermediate set deviates by more than 0.01, and that difference between the largest value (R479K) and the smallest value (D123A) is only 0.7. In comparison to the data collected for the various model sizes, this geometric difference is small (in Table 2.3, the average τ_4 value is 0.48 without model ***2B*** (τ_4=0.35), making the difference 0.13).

For the τ_5 parameters, the deviation between the values for Ni-3 and Ni-R is 0.01, indicating there is no quantifiable change of the orientation of the four S atoms and the μ-H at the Ni center. For Ni-C, we do see a change of 0.11 between the wild type and R479K, however the energy difference between these two models is 0.3 kcal/mol, which suggests this difference in the τ_5 parameter does not influence the reaction.

To further support the claim that there is little change among the local active site structure between these mutated models, selected bond lengths were analyzed focused on the core structure of the active site, $[(RS)_2Ni\mu(SR)_2Fe(CO)(CN)_2]$ where SR stands for the Cys residues. These bond lengths were compared for each intermediate, and we found that all of the bond lengths only differ, at most, by 0.05Å, and most of them differ by only 0.01Å. These results further prove that changing these “canopy” ligands does not change the local active site geometry, which has been found to play a large role in the catalytic activity of the enzyme (Sections 2 and 4).

The last feature that we will discuss is the overall geometric distortions of the entire models tested. We achieved this by overlaying the frozen atoms and visually analyzing the structures. This is shown in Figure 3.5, where the wild type (green), the R479K (yellow), and the D123A (gray) models for the Ni-L intermediate can be seen. In order to analyze this visual, we will discuss the various areas of the active site: (*1*) the four Cys residues, (*2*) the Fe coordinated inorganic ligands, (*3*) the R479 residue, and (*4*) the D123 residue.

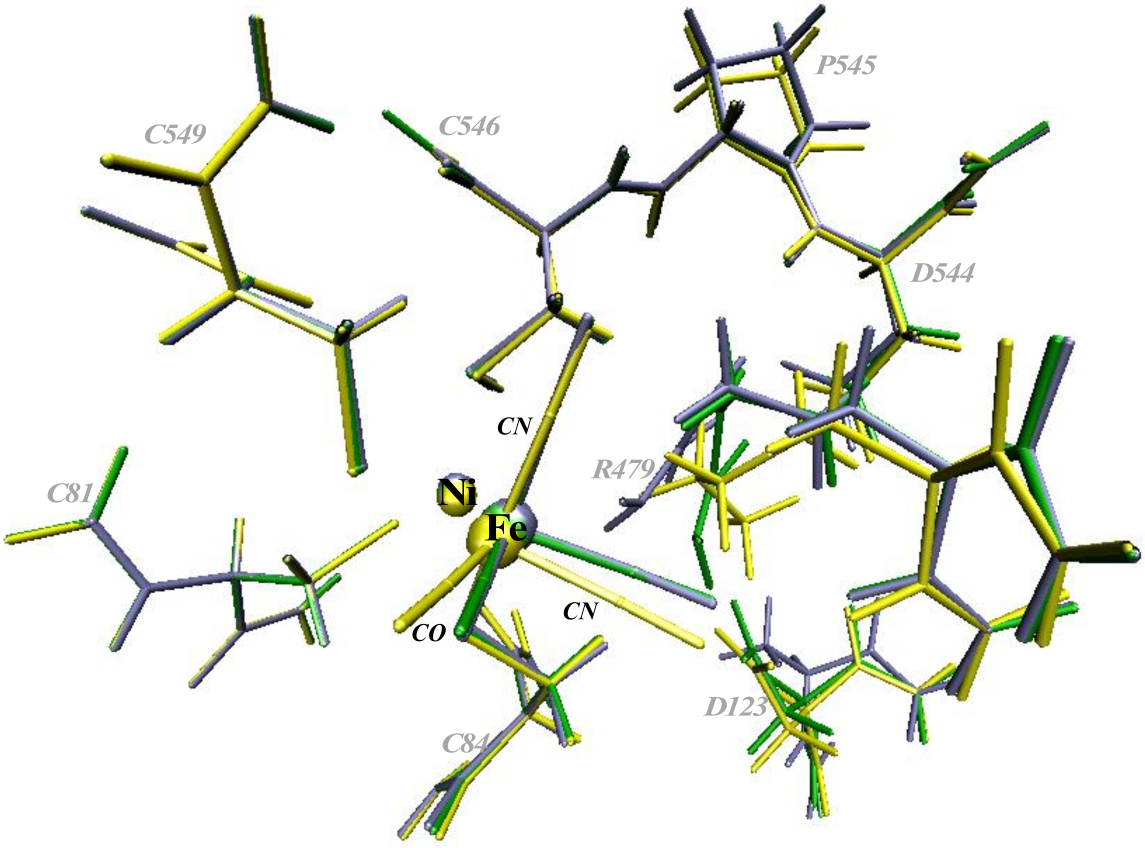

Figure 3.5: Geometries of the native and mutated models of the active site overlayed to show geometric distortion. Green: the native enzyme. Yellow: R479K mutation. Gray: D123A mutation. The intermediate shown is Ni-L.

First, we will analyze the local active site structure. For the four Cys residues (*1*), we find little deviations between the models tested, which is consistent with the τ parameter data and the bond length data. For the Fe coordinated ligands (*2*), some changes can be seen in the R479K model. We see a slight rotation of the inorganic ligands, specifically the CO and CN ligands below the Fe atom in the orientation shown in Figure 3.5. Based on the quantitative data already discussed, this geometric difference does not influence the catalytic activity or the overall structure of the core of the active site.

Analysis of the Arg479 residue (*3*) is rather interesting, seeing as these changes do not influence the catalytic activity of the enzyme. The first noteworthy change is the orientation of the Lys in the R479K model. When we compare the R479K (yellow) to the wild type (green), we see the amine group of the Lys oriented so that it forms hydrogen bonds with the D544 ligand, instead of the placement of guanidine group of the Arg side chain which is much closer to the active site. The Ni-N distance for the Lys side chain is 5.5 Å, and the Ni-N distance for the closest N of the guanidine group of the Arg is 4.3 Å.

One other interesting feature of the Arg479 residue occurs when comparing the wild type (green) with the D123A model (gray). By replacing the D123 residue with an alanine residue, the carboxyl functional group is lost, which means that the hydrogen bonds that constrain the guanidine tail of the Arg residue no longer exist. This phenomenon can be visually seen, and results in more interaction with the Ni center, since the distance between the Ni and the closest N of the guanidine group is 3.3 Å, which is 1 Å closer to the Ni than the wild type.

The last group to discuss is the D123 residue (*4*). When we compare the wild type with the R479K model, we see a small movement of the carboxyl group due to the lack of the hydrogen bonds that form between the guanidine group and the carboxyl group since the Lys of the R479K model has intermolecular interactions with the D544 residue. This allows for the additional flexibility of the D123 residue in the R479K model. Upon analysis of the D123A model, we can see that the side chain changes from -CH_2COO to -CH_3, which causes of parts of the amino acid backbone to shift.

Regardless of the geometric changes found in the “canopy” residues, we have previously stated and shown that the catalytic activity does not change between the wild type model and the mutated models given the limitations of the models tested. The geometry of the core of the active site is mostly maintained, which further proves that the largest factor that effects the energetics of catalysis of [NiFe]-hydrogenase is the local geometry of the active site.

3.4 Conclusion

In this work, we computationally studied the effect of mutating the nearby highly conserved amino acid residues that surround the active site in a sort of “canopy” structure. The mutations studied were based on the work done by Armstrong and coworkers that showed a change from the canopy Arg residue to a Lys has 0.8% of the activity of the native enzyme and changing the nearby Asn residue to Ala results in 26% of the activity of the native enzyme.[69]

We have shown that the overall reaction energy, dubbed peak to trough energy, deviates between the three models tested by only 0.5 kcal/mol, leading to the conclusion that, given the limitations of these models, there is no decrease in H_2 oxidizing activity for the mechanism studied.

Additionally, we have shown that the geometry of the core active site, $[(RS)_2Ni\mu(SR)_2Fe(CO)(CN)_2]$, is mainly conserved. This has been hypothesized to have the largest influence on catalysis, and this current work further supports that claim. As discussed in Section 3.3.2, there are geometric distortions within the “canopy” residues, however these geometric changes do not have any influence on the intermediate energies, or the overall peak to trough energy. The phenomenon of the conservation of the local enzyme active site structure will be discussed further in the next section.

While we were unable to find rationale for the decreased turnover rates found via experiment,[69] we hypothesize that a water molecule could potentially inhibit binding. The reorientation of the R479K mutation opens a pocket between the residue and the active site binding position, as shown in the 5.5 Å bond distance between the Lys N group and the Ni. This allows possible inhibition of H_2 binding at the Ni center due to a solvent water molecule entering this now-opened pocket. For the D123A model, a similar rationale could be the closer position of the now-unconstrained Arg guanidinium tail (3.3 Å from the Ni to the N group closest to Ni) causes difficulty for H_2 binding which slows down catalysis, further supported by the > 3 kcal/mol increase in the Ni-H_2 intermediate compared to the native and R479K models. Future work should include some explicit or crystallographic waters to test the hypothesis for the Lys mutation, as well other model manipulations to assess the D123A slowdown. Regardless, this study was integral in isolating the importance of the active site structure, allowing us to better understand the structure/function relationships for [NiFe]-hydrogenase catalysis. Additionally, we did not calculate transition states for the reaction profile. The mutations could influence the energetics of the transition states to cause catalytic shutdown, therefore another avenue of study for this project would be to isolate the transition states and analyze any changes that could be attributed to the amino acid mutations.

4. Ni-Fe Hydrogenase – Study of Biomimetic Changes to the Active Site and Influences on the Structure and Reactivity of the Enzyme

4.1 Introduction

In the field of catalyst development, nature can be used as inspiration for new catalysts due to the fact that these complex biological systems are able to efficiently process and carry out various chemical reactions.[59, 81] Hydrogenases, which reversibly catalyze H_2 oxidation or H^+ reduction,[8, 12, 13] are an important and diverse class of enzymes that have the potential to provide insight into the necessary requirements for utilization of a "hydrogen fuel economy," which would result in replacement of internal combustion engines for transportation with hydrogen-based fuel cells that produce energy from conversion of H_2 and O_2 into H_2O for clean, renewable, and carbon neutral energy technologies for clean, renewable, and carbon neutral energy technologies.[59, 81, 82]

Research into the structure and function of hydrogenases, as stated in Sections 2 and 3, can provide insight into the expression, biosynthesis, structure, and function of hydrogenases to achieve the goal of creating new catalysts.[10] Even though the different types of hydrogenases ([NiFe], [FeFe], and [Fe]) are physiologically unrelated,[10, 83] structural and mechanistic similarities exist, such as the ability to efficiently oxidize molecular hydrogen and the inclusion of a low spin Fe (II) with coordination to carbonyl and thiolate ligands.

Currently, Pt based fuel cells are the main source for oxidation of molecular hydrogen, however Pt is an expensive noble metal and limited resource. Over the lifetime of these fuel cells, the Pt cathode suffers from reduced activity and efficiency due to corrosion of the carbon support, oxidation of the electrode, loss of active surface area, migration, and impurities that poison the catalyst.[82] One goal of studying biological systems like [NiFe]-hydrogenases is to develop purely organic[82] or transition metal based catalytic alternatives.[84-92]

In addition to creation of alternatives to Pt cathodes, the advancement of this field has the potential to develop methods for H_2 oxidation that are robust and have products that are capable of being mass produced, leading to the evolution of highly active, widely available electrodes for use in fuel cells. In fact, H_2/O_2 biofuel cells have been developed from the d. vulgaris [NiFe]-hydrogenase.[93] However, power output is restricted by substrate mass transport, as well as lack of protection from O_2 and high-potential deactivation from the limiting conditions of the bioanode.[21] Szczesny and coworkers cleverly constructed a gas-breathing polymer-based bioanode that protects the biocatalyst from high-potential deactivation through preventing direct contact with the electrode surface, as well as protection from O_2 by reduction of O_2 is reduced at the outer polymer layer, leaving the biocatalyst/reaction layer unaffected.[94] Regardless, utilization of enzymes as biofuel cells is relatively niche owing to the limited pH and temperature operating conditions. Additionally, enzymes are not robust and do not efficiently utilize the electrode surface due to their large molecular size.[95] An alternative to biofuel cells is the development of biomimetic analogues, utilizing what has been discovered regarding the structure and function of enzymes to attempt to mimic the activity using inorganic catalysts.

Hydrogenases have been found to have high turnover rates (>1000s^{-1}),[8, 16-19] low overpotentials, and stability even at elevated temperatures, therefore they are considered to be highly efficient catalysts.[8] Many biomimics of the [NiFe]-hydrogenase site have been developed, ranging from changing the Fe coordinated ligands, replacing the Cys residues, using protecting groups to preserve the chemistry of certain structural features, and even changing the identity of the transition metals.[84, 86, 96-106]

The basis for this current study is to use currently developed biomimics to manipulate our computational model of the active site and determine the influence of the changes to the enzyme active site. This work provides insight on how these changes affect the structure, redox character, and reactivity, and has the potential to inform features that would improve the field of biomimetic catalysis for [NiFe]-hydrogenases. The goal is to ultimately create a biomimetic catalyst with high TOFs (turn over frequency) and low overpotential. This can be accomplished by using computational methods to change one feature at a time to isolate exactly how that change affects the system, which is something that is usually unattainable or impractical in a laboratory setting.

4.2 Computational Details

The computational models were constructed and calculations were run utilizing the same methods as in the previous Sections 2 and 3. Gaussian 16 suite version C01[107] was used for the geometry optimizations and frequency calculations using BP86[64]/def2-TZVP.[65, 66] The singlet states (Ni-SI$_a$, Ni-H$_2$, Ni-3, Ni-R) were run with the restricted DFT formalism, while the doublet states (Ni-C and Ni-L) were run unrestricted. Grimme's D3 dispersion correction[4] was included in addition to PCM[67] with $\varepsilon = 4$ to simulate the surrounding enzyme environment.[56, 58] Frequency calculations were also performed to obtain thermodynamic corrections, and any frequencies less than 50 cm^{-1} were shifted. The free energies for Ni-C and Ni-L were calculated with the same formalism in Section 2.2 eq 2.1. Reduction potentials were also calculated from Section 2.2 utilizing eq. 2.2 and eq. 2.3.

For computational efficiency, model ***3B*** (Section 2.2 Figure 2.3) was the base structure used to assess the effect of the biomimic inspired changes to the active site model. In our previous work, we proved that this model, which constrained a C and H atom at the end of each Cys residue, resulted in comparable energetics and structure to the larger model ***2C*** (Section 2.2 Figure 2.2), which included the entire amino acid residue backbone.

We have broken down the active site into four main domains for the study of these biomimetic changes: (i) Fe-coordinated ligands, (ii) metal-metal bridging μ-ligands, (iii) Ni-coordinated terminal ligands, and (iv) choice of metal centers. These domains are represented in Figure 4.1. Features that were tested were common between various literature sources,[19, 96-98, 100-102] and specific biomimetic catalysts shown in Figure 4.2 were used to choose what changes to study first.

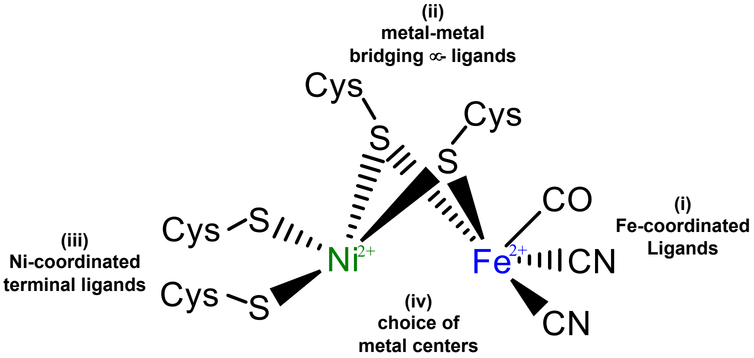

Figure 4.1: The four domains of the [NiFe]-hydrogenase active site for study with biomimetic inspired structural changes. (i) Fe-coordinated ligands, (ii) metal-metal bridging μ-ligands, (iii) Ni coordinated terminal ligands, and (iv) choice of metal centers.

In domain (i) we have three different ligands to test modify: two CN and one CO. It is common for experimentalists to avoid using the CN groups due to the reactivity of the basic N site. For biomimic (6), these ligands were protected by attaching organoboranes (BAr^F_3) to the Fe-CN groups.[102] In biomimics (1), (2), and (3), we can see the CN ligands are replaced with cyclopentadienyl (Cp) or pentamethylcyclopentadienyl (Cp*) ligands,[19, 96-98] therefore the inclusion of Cp and Cp* ligands is of interest and studied.

In addition to the effect of the Cp and Cp* ligands, we also were interested in the effect electron withdrawing/donating ligands have on the chemistry of the active site. Therefore, we also tested the effect of ligands that are more electron withdrawing (N≡N) and more electron donating (NH_2) than CN by replacing one CN group with either N≡N or NH_2.

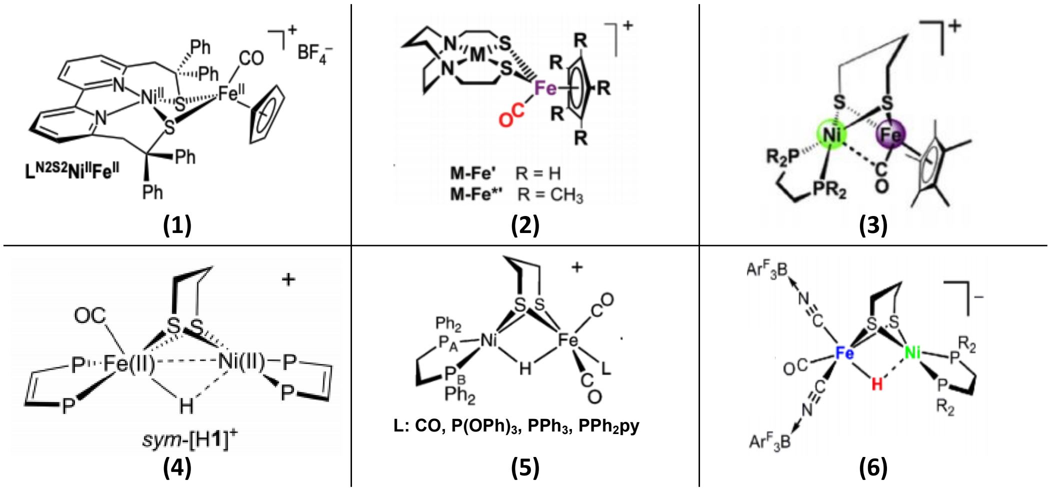

(1) (2) (3) (4) (5) (6)

Figure 4.2: Biomimetic catalysts from the literature[19, 96-98, 100-102] that influence choices of changes to be made in initial studies of biomimetic inspired models of the [NiFe]-hydrogenase enzyme active site. (*Permissions in footnotes*)

The other domain tested in this section is (ii) metal-metal bridging μ-ligands. In biomimics (3), (4), (5), and (6), the bridging Cys residues from the enzyme active site are replaced with a dithiolate ligand, 1,3-propanedithiol (pdt). To systematically assess any structural changes from use of this bidentate dithiolate ligand, we used

---

(1) Reprinted by permission from Springer Nature Customer Service Centre GmbH: Springer Nautre. *Nature Chemistry*, Nickel-centred proton reduction catalysis in a model of NiFe hydrogenase. Brazzolotto, D.; Gennari, M.; Queyriaux, N.; Simmons, T. R.; Pecaut, J.; Demeshko, S.; Meyer, F.; Orio, M.; Artero, V.; Duboc, C. Copyright 2016.

(2) Republished with permission of Royal Society of Chemistry, from Ghosh, P.; Quiroz, M.; Wang, N.; Bhuvanesh, N.; Darensbourg, M. Y., Complexes of MN2S2 center dot Fe(eta(5)-C5R5)(CO) as platform for exploring cooperative heterobimetallic effects in HER electrocatalysis. *Dalton Transactions* **2017,** *46* (17), 5617-5624. Copyright 2017; permission conveyed through Copyright Clearance Center, Inc

(3) Reprinted from Ahmed, M. E.; Dey, A., Recent developments in bioinspired modelling of [NiFe]- and [FeFe]-hydrogenases. *Current Opinion in Electrochemistry* **2019,** *15*, 155-164. Copyright 2019; with permission from Elsevier

(4) Reprinted with permission from Ulloa, O. A.; Huynh, M. T.; Richers, C. P.; Bertke, J. A.; Nilges, M. J.; Hammes-Schiffer, S.; Rauchfuss, T. B., Mechanism of H-2 Production by Models for the NiFe - Hydrogenases: Role of Reduced Hydrides. *Journal of the American Chemical Society* **2016,** *138* (29), 9234-9245. Copyright 2016 American Chemical Society.

(5) Reprinted with permission from Barton, B. E.; Rauchfuss, T. B., Hydride-Containing Models for the Active Site of the Nickel-Iron Hydrogenases. *Journal of the American Chemical Society* **2010,** *132* (42), 14877-14885. Copyright 2010 American Chemical Society.

(6) Reprinted with permission from Manor, B. C.; Rauchfuss, T. B., Hydrogen Activation by Biomimetic NiFe -Hydrogenase Model Containing Protected Cyanide Cofactors. *Journal of the American Chemical Society* **2013,** *135* (32), 11895-11900. Copyright 2013 American Chemical Society.

other modified pdt-style ligands. The first was chosen to shorten the distance between the S atoms: (1*Z*)-prop-1-en-1,3-dithiol (pedt). The second was used to probe the effect of how additional rigidity alkyl chain would affect the structure, therefore we used: (1*Z*,3*Z*)-but-1,3-dien-1,4-dithiol (bdedt).

4.3 Results and Discussion

4.3.1 Domain (i) Fe-Coordinated Ligands

The first domain studied is the Fe-coordinated inorganic ligand binding. As previously mentioned, a common feature of biomimetic [NiFe]-hydrogenase complexes is the inclusion of Cp ligands. Therefore, we assessed the influence of inclusion of the Cp and Cp* ligands in lieu of the two CN ligands, as well as the models where the electron withdrawing/donating character of the CN ligand is changed. The free energy reaction profile for these biomimetic ligands is shown in Figure 4.3. The reaction profile follows the catalytic cycle depicted in Figure 2.1.

First, we will analyze the effects between the native (orange), N_2 (blue), and NH_2 (red) models. The structures of the active site across the catalytic intermediates are indicative of the native model. There are a few interesting features to discuss, namely the P2T energy difference, which gives an indication of the overall reaction energy, and the possibility of spontaneous electron ejection for the catalytic cycle.

The P2T energies are defined as the difference between the highest energy and lowest energy intermediates, in most cases these are the Ni-3 and Ni-C intermediates, respectively. For this discussion, Ni-3 and Ni-C are the intermediates for the native and N_2 models, however for the NH_2 model the highest energy intermediate is Ni-R. Therefore, we will compare the Ni-3 to Ni-C P2T energies from native and N_2 with the Ni-R to Ni-C P2T energy for NH_2, however the Ni-3 intermediate is only 0.9 kcal/mol lower in energy than Ni-R for NH_2, resulting in little change in interpretation.

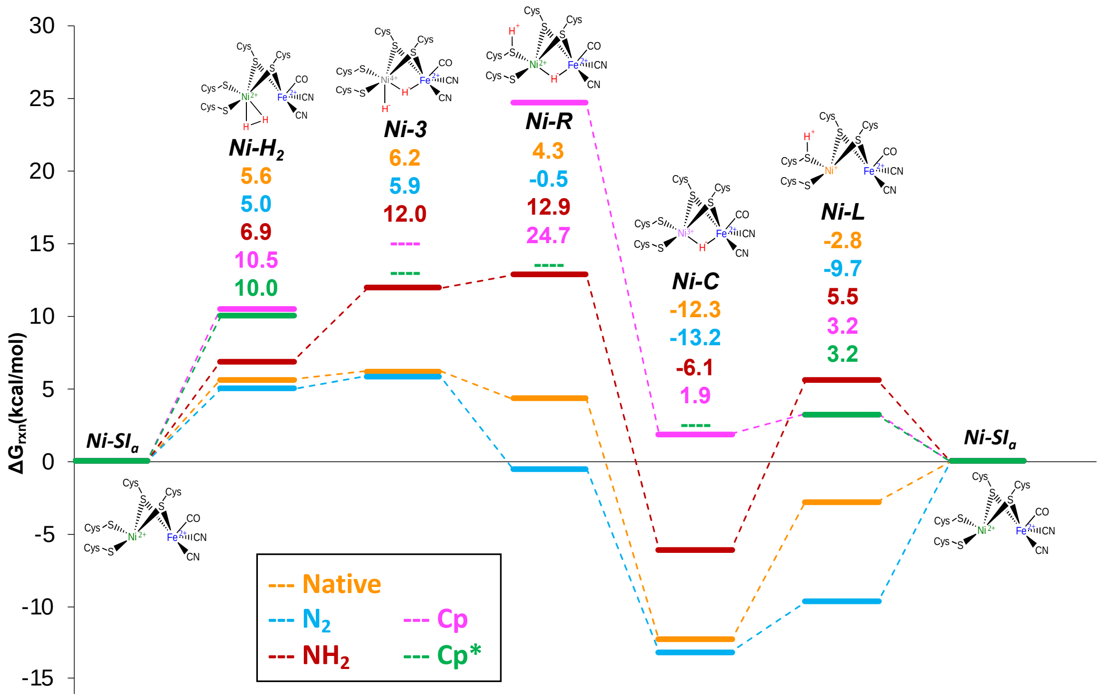

Figure 4.3: Free energy reaction profile for the catalytic cycle of [NiFe]-hydrogenase with biomimetic inspired changes to the (i) Fe-coordinated ligands. Energies are reported with respect to the Ni-SIa intermediate. The models shown are the native (orange), 1 CN replaced with 1 N_2 (blue), 1 CN replaced with NH_2 (red), 2 CN replaced by Cp (pink), and 2 CN replaced by Cp* (green).

The P2T energies are 18.5 (native), 19.1 (NN), and 19.0 (NH_2) kcal/mol. As we have discussed in the previous two chapters (2.3 and 3.3), these energies are well within the range of all of the other models tested. This implies that the overall activity of the enzyme is most likely unchanged by the more electron withdrawing ligand, NN, or the more electron donating ligand, NH_2. However, when we analyze the redox character of the active site, we see an interesting phenomenon. The methods outlined in Section 2.2 for calculation of the reduction potentials were utilized for this section, and the results are shown below in Table 4.1.

Table 4.1: Redox potential calculations for the biomimetic inspired changes to the domain (i) Fe-coordinated ligands, as calculated by eq. 2.3. The reaction pathways tested are depicted in Figure 2.1.

$\mathrm{Ni{-}H_2} \rightarrow [\mathrm{Ni{-}H_2}]^{3+} + e^-$	
Model	**E_{cell} (V)**
Native	-0.08
NN	-0.51
NH_2	1.23
cp	-
cp*	-

$\mathrm{Ni{-}C} \rightarrow [\mathrm{Ni{-}C}]^{4+} + e^-$	
Model	**E_{cell} (V)**
Native	-0.09
NN	-0.57
NH_2	0.34
cp	0.03
cp*	-

$\mathrm{Ni{-}L} \rightarrow [\mathrm{Ni{-}L}]^{2+} + e^-$	
Model	**E_{cell} (V)**
Native	0.69
NN	-0.01
NH_2	0.62
cp	0.92
cp*	1.01

As we discussed in Section 2.3.1 our results indicated that spontaneous electron ejection at the Ni-L intermediate was possible, so the reaction proceeds from the Ni-L through the oxidized form $[Ni\text{-}L]^{2+}$ and regeneration of Ni-SI_a following proton dissociation. This is shown in the table above for the native model, as indicated by the positive E_{cell} value for the Ni-L oxidation pathway compared to the negative values for the Ni-H_2 and Ni-C pathways.

Upon analysis of the more electron withdrawing N_2 ligand model, we see that all of the E_{cell} values for all tested pathways are negative. This shows that changing one CN ligand to a N_2 ligand changes the redox character of the active site, indicating that spontaneous electron ejection is unlikely to occur throughout the catalytic cycle. The influence of the inclusion of a ligand with a stronger electron withdrawing character than CN is based on the metal-metal cooperativity of the active site, mainly that Fe (II) is no longer able to stabilize the redox character of the Ni center due to electron density being pulled toward the N_2 ligand.

When we compare this to the more electron-donating ligand, NH_2, we find the opposite phenomenon – all of the E_{cell} values across the three pathways tested are positive, indicating the possibility of spontaneous electron ejection to the proximal [4Fe-4S] cluster. The redox character of the active site is thus changed opposite to the N_2 ligand model, namely that the NH_2 ligand donates electron density to the Fe center, which further stabilizes the Ni center, allowing for easier ejection of electrons. While the active site geometry does not undergo any structural changes from the manipulation of the CN ligand and the overall reaction energy does not change, the redox character of the active site is influenced by these modifications, indicating that the choice of ligands for replacing CN in biomimetic systems should be chosen to mimic the electron withdrawing character of CN without being too strongly electron withdrawing. These results also indicate that the Cp ligand would have an electron donating nature, as the Ni-C oxidation path has the potential to spontaneously eject an electron, just like the NH_2 model.

The other two models tested in this section are the Cp and Cp* models, where the two CN ligands coordinated to Fe were replaced. As can be easily noticed, not all of the intermediates were able to be isolate for these biomimetic inspired models. For the Cp ligand model, the Ni-3 intermediate consistently minimized to the Ni-H_2 geometry. For the Cp* model, the Ni-3, Ni-R, and Ni-C intermediates could not be isolated. The common factor between all of these intermediates, in addition to the Ni-R and Ni-C intermediates for Cp, is that the bridging μ-H due to the structural changes associated with the inclusion of these ligands, namely the elongation of the Ni-Fe bond. These bond lengths can be found in Table 4.2.

Table 4.2: Bond lengths of Ni-Fe for all intermediates in the active site structure of the biomimetic inspired Cp and Cp* ligand models. Ni-3 was excluded because it was not isolated for either Cp or Cp* model.

Intermediate	Cp model	Cp* model
Ni-SI$_a$	3.15 Å	3.36 Å
Ni-H$_2$	3.26 Å	3.38 Å
Ni-R	2.63 Å	N/A
Ni-C	3.34 Å	N/A
Ni-L	3.00 Å	3.38 Å

Our previous work and work shown in the literature[49] have all indicated that the Ni-Fe bond length for the native enzyme active site structure should range between 2.54 and 2.84 Å across all models, including various crystal structures of the reduced catalytically active form of the enzyme. Only one intermediate between both Cp and Cp* models is in this range - Ni-R from Cp. However, when we visualize this intermediate, as shown in Figure 4.4(a), we can see that there are other structural distortions apparent that only exist in this intermediate, specifically the elongation of the Ni-S bond to form exclusive coordination to Fe, and that the Cp ligand binds through a single C instead of as η^5-(C_5H_5).

Analysis of the Cp model Ni-C intermediate, shown in Figure 4.4(b), shows that the elongation of the Ni-Fe bond to 3.34 Å causes the μ-H to bind exclusively to Ni. The formation of the μ-H as a bridging ligand is present in multiple steps in the catalytic cycle, and has been resolved using X-Ray crystallography.[40] It is highly probable that the inability for the μ-H to form is the reason we were unable to isolate intermediate geometries for the Cp* model, as the Ni-Fe bond lengths for the three intermediates were even further elongated than the Cp model.

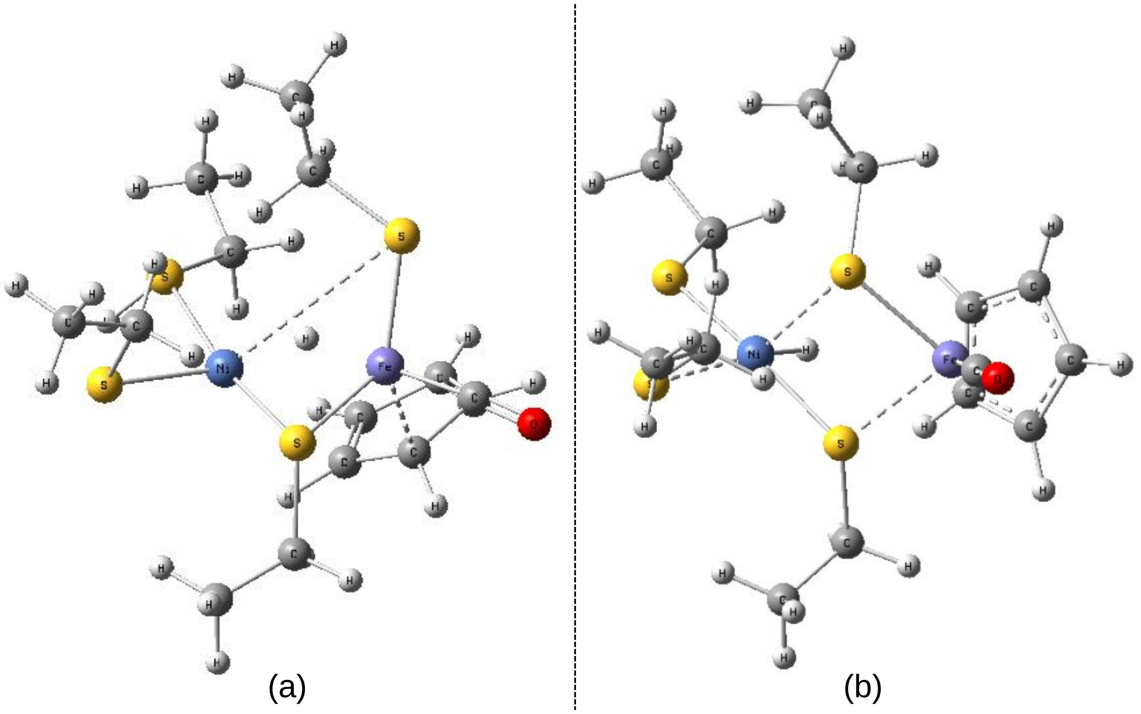

(a) (b)

Figure 4.4: Optimized geometries of the Cp model of the biomimetic inspired [NiFe]-hydrogenase system. (a) is intermediate Ni-R and (b) is intermediate Ni-C.

These geometric changes to the active site are represented in the energetics of the catalytic cycle shown previously in Figure 4.3. Since we could not isolate the Ni-3 intermediate, the P2T energy for the Cp model is the difference between the Ni-R and Ni-C intermediates, 22.8 kcal/mol, which is 4.3 kcal/mol higher than the native model. We can assume the Cp* ligand would have a very similar or higher P2T energy relative to Cp, considering the Ni-H_2 and Ni-L intermediate energies differ between Cp and Cp* by < 0.5 kcal/mol and the fact Ni-Fe bond is further elongated.

The results of the influence of the Cp and Cp* ligands, as well as the N_2 and NH_2 models, are further proof that the activity of the [NiFe]-hydrogenase enzyme is strongly modulated by the structure and redox character of the active site. The influence of electron withdrawing/donating ligands show that the Fe-coordinated ligands strongly influence the redox character, and subsequently the mechanism of catalysis. The geometric distortions observed for the Cp and Cp* ligand models, notably the inability to form the μ-H, are the major factors that influence the increase in P2T energy. These results can be used to inform experimental studies on biomimetic works, specifically that the structure of the active site must be as conserved to as great an extent as possible and that any changes to the CN ligands should have a similar electron withdrawing capacity.

4.3.2 Domain (ii) Ni-Fe Bridging μ-Ligands

The next domain in the current study is domain (ii), which is manipulation of the two μ-Cys residues that bridge between Ni and Fe via the S atoms. As shown in Figure 4.2, a common replacement for these residues is using a bidentate dithiolate ligand, pdt. To study influence of this ligand, we compared the pdt model to the native, in addition to a shortened C chain between S atoms by adding a double bond forming the pedt model and adding additional rigidity by elongating the C chain to a butadiene, forming the bdedt model. The reaction profile is shown in Figure 4.5.

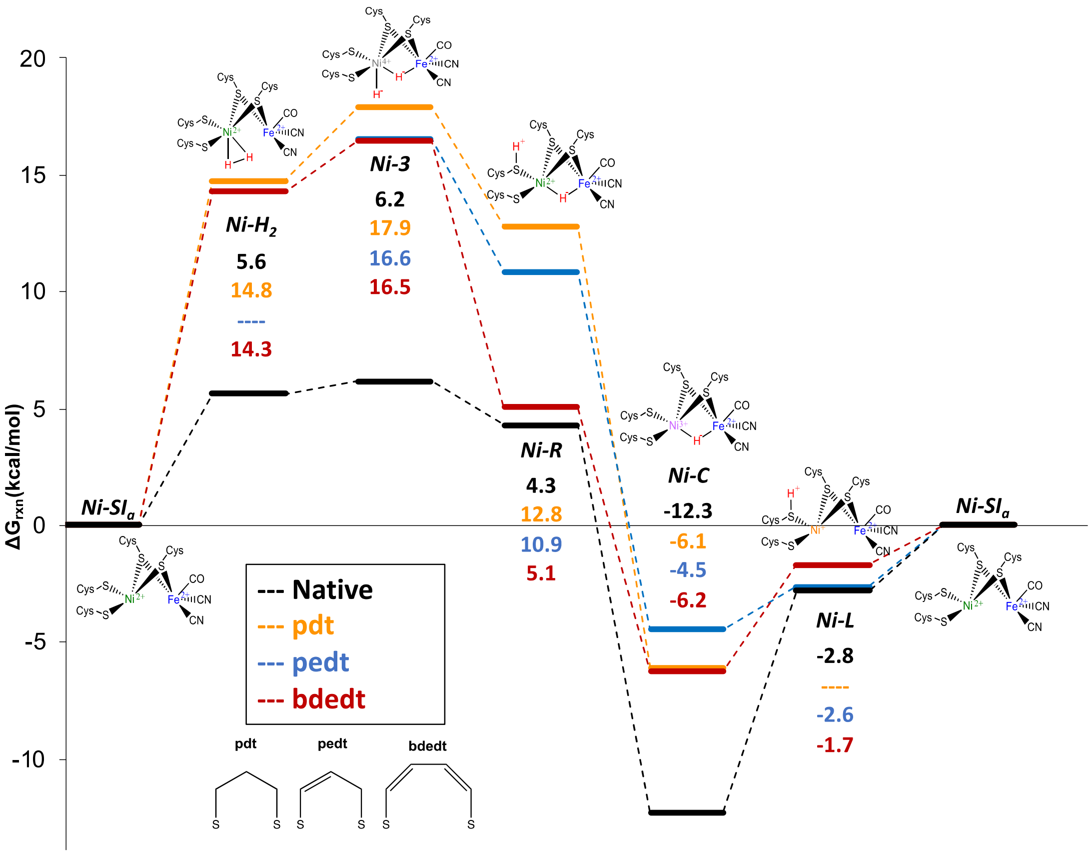

Figure 4.5: Free energy reaction profile for the catalytic cycle of [NiFe]-hydrogenase with biomimetic inspired changes to the (ii) Ni-Fe bridging μ-ligands. Energies are reported with respect to the Ni-SI$_a$ intermediate. The models shown are the native (black), 2 Cys replaced with pdt (gold), 2 Cys replaced with pedt (blue), and 2 Cys replaced with bdedt (red).

As with previous reaction profile analyses, we compare the P2T energies for all the models tested. For this data, the highest energy intermediate for all the models is Ni-R, and the lowest energy intermediate is Ni-C, as with every single model tested through Sections 2, 3, and 4. We find the native (18.5 kcal/mol) is 2.6-5.5 kcal/mol lower in energy than the pdt-derived models: 24.0 (pdt), 21.1

(pedt), and 22.7 (bdedt) kcal/mol. With this information, we can assume that the pdt based ligand modifications would slow down catalysis.

The redox potential of the pdt derived modifications to the active site remains unchanged. In Table 4.3, the redox potential for spontaneous electron ejection is shown for the Ni-C and Ni-L pathways. Ni-H_2 was omitted in this case due to difficulty in optimizing either the Ni-H_2 intermediate, as is the case for pedt, or the $[\text{Ni-H}_2]^{3+}$, as is the case for pdt and bdedt. Regardless, we can see from the Ni-C and Ni-L data that replacement of the Cys ligands with the bidentate dithiolate ligands does not change the redox character of the active site, therefore the catalytic mechanism is likely unchanged with this biomimetic modification.

Table 4.3: Redox potential calculations, in V, for the biomimetic inspired changes to the domain (ii) Ni-Fe bridging μ-ligands, as calculated by eq. 2.3.

$\text{Ni–C} \rightarrow [\text{Ni–C}]^{4+} + e^{-}$	
Model	**E_{cell} (V)**
Native	-0.09
pdt	-0.02
pedt	-0.15
bdedt	-0.15

$\text{Ni–L} \rightarrow [\text{Ni–L}]^{2+} + e^{-}$	
Model	**E_{cell} (V)**
Native	0.69
pdt	-
pedt	0.65
bdedt	0.56

We now turn to the structural data to see further proof that this increase in overall reaction energy is due to the structural differences found in the $[(RS)_2Ni\mu(SR)_2Fe(CO)(CN)_2]$ core geometry. The data for the τ_4[72] and τ_5[73] parameters quantifies the distortion of the $(RS)_2Ni\mu(SR)_2$ moiety. We have previously shown (Sections 2 and 3) in the models which adequately describe the active site of [NiFe]-hydrogenase that there is little deviation for both τ_4 and τ_5 parameters, corresponding to similar catalytic reaction energies between 18.5 and 19.7 kcal/mol across a wide spectrum of catalytic models. The τ_4 and τ_5 parameters are calculated by eq. 2.4 and eq 2.5 and the results are shown in Table 4.4 and Table 4.5.

Table 4.4: Values of τ_4 parameters for all models including each intermediate involved in catalysis as depicted in Figure 2.1. Selected values that deviate from the native model by more than 0.1 are bolded in red.

Intermediates	**Models Tested**			
	Native	**pdt**	**pedt**	**bdedt**
Ni-SI$_a$	0.47	**0.08**	**0.11**	**0.24**
Ni-H$_2$	0.52	**0.37**	-	**0.34**
Ni-3	0.53	0.61	0.59	0.53
Ni-R	0.54	0.56	0.54	**0.30**
Ni-C	0.55	0.65	0.65	**0.41**
Ni-L	0.52	-	0.62	**0.77**

Table 4.5: Values of τ_5 parameters for all models including each intermediate involved in catalysis as depicted in Figure 2.1. Selected values that deviate from the native model by more than 0.1 are bolded in red.

Intermediates	**Models Tested**			
	Native	**pdt**	**pedt**	**bdedt**
Ni-3	0.17	**0.04**	**0.02**	0.11
Ni-R	0.12	0.06	0.10	**0.53**
Ni-C	0.12	**0.33**	0.15	**0.38**

The deviations between the τ parameters for all the pdt-derived models can be seen in the red bolded numbers, indicating geometric distortion about the Ni center. For the pdt model, Ni-SI$_a$ and Ni-H$_2$ are shown to deviate from the native model for the τ_4 parameters and additional deviations are seen for Ni-3 and Ni-C in the τ_5 parameters. The pedt model, which has the P2T energy closest to the native model (2.6 kcal/mol higher), has the least geometric distortion of the three models tested. Only Ni-SI$_a$ in the τ_4 parameter and Ni-3 in the τ_5 parameter exceeds 0.1 difference from the native model; however, it is worth noting that the Ni-H_2 was not isolated due to consistent H_2 abstraction from Ni during optimization. Finally, in the bdedt model, all of the parameters differ from the native except for both the τ_4 and τ_5 parameters for the Ni-3 intermediate.

Table 4.6: S-S bond lengths, in Å, for the three models tested compared to the native.

Intermediates	**Models Tested**			
	Native	**pdt**	**pedt**	**bdedt**
Ni-SI$_a$	2.8	3.1	3.1	3.2
Ni-H_2	2.9	3.1	-	3.3
Ni-3	2.9	3.2	3.2	3.2
Ni-R	3.0	3.3	3.2	3.3
Ni-C	2.9	3.2	3.1	3.3
Ni-L	2.9	-	3.2	3.3

These geometric distortions across all the pdt-derived models can be attributed to the position of the bridging S atoms. In the native model, the S-S distance for the bridging Cys residues is 2.8-3.0 Å across various models tested, however the S-S distance in the biomimetic models all exceed 3.1 Å. These bond lengths are compared to the native model in Table 4.6. The elongation of the S-S bond is not unexpected, considering two unconnected Cys residues were replaced with a single bidentate dithiolate ligand. As one would expect due to the (1*Z*,3*Z*)-but-1,3-

dienyl group, the bdedt model has the largest S-S distances of 3.2-3.3 Å due to the inclusion of an additional C compared to the pdt and pedt ligands.

There is a strange geometric anomaly found in this data set. For the pdt model, Ni-C has strange torsion where the $\mathrm{Ni\mu(SR)_2Fe}$ cluster has twisted out of the native position (Figure 4.6(a)), and the Ni-L geometry was not isolated because all optimizations kept resulting in minima that exhibited this large-scale twist of the bridging cluster. This twisting phenomenon was also found in Ni-L intermediate for bdedt.

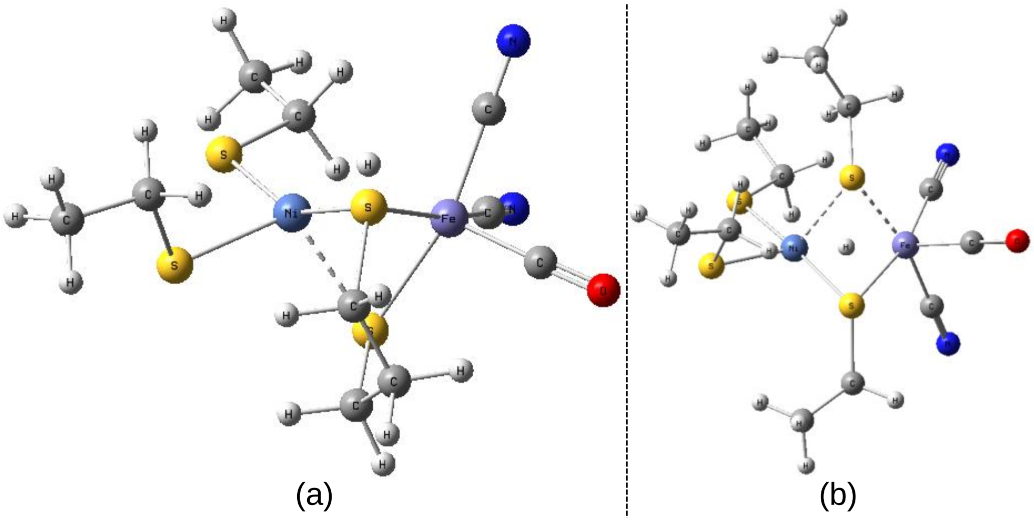
(a) (b)

Figure 4.6: Visualization of the anomalous torsion of the $\mathrm{Ni\mu(SR)_2Fe}$ moiety in the Ni-C intermediate for the (a) pdt model compared to the (b) native Ni-C model.

The results in this section show that inclusion of these pdt-derived bidentate dithiolate ligands in lieu of the native bridging Cys residues increases the overall reaction energy due to the changes in the $\mathrm{[(RS)_2Ni\mu(SR)_2Fe(CO)(CN)_2]}$ active site structure. These geometric distortions are found in the placement of the S atoms of the dithiolate ligands, as seen in the S-S bond distances and the τ parameters.

Once again, these results further support the claim that the factor that most strongly influences the catalytic activity of [NiFe]-hydrogenase is the core structure of the active site, and the best method via biomimetic catalyst design for mimicking this enzyme is to match the structure of the active site as closely as possible while maintaining the redox character.

4.4 Conclusion

In summary, biomimetic-inspired modification of the [NiFe]-hydrogenase active site were studied for domain (i) Fe-coordinated ligands, and domain (ii) Ni-Fe bridging μ-ligands in this section. The data gathered supports the claim that the primary factor that affects the catalytic function of the enzyme is the structure of the active core, $[(RS)_2Ni\mu(SR)_2Fe(CO)(CN)_2]$, and secondarily the redox character of the active site.

When CN is replaced with a more electron withdrawing ligand, e.g., N≡N, the electronic density pulled toward the ligand destabilizes the active site at the Fe center, causing the Ni to lose the potential capacity for spontaneous electron ejection to the proximal [4Fe-4S] cluster. Conversely, a more electron donating ligand (NH_2) results in additional stability to the Fe center, allowing Ni to spontaneously eject an electron at any step throughout the catalytic cycle. Therefore, replacement of CN ligands should consider how strongly electron withdrawing or donating the modifying ligand is in order to maintain the redox character of the active site.

The modifications of the Cp and Cp* ligands cause large geometric distortions in the active site, mainly the Ni-Fe bond distance. This distortion, which increased the overall reaction energy by upwards of 4 kcal/mol, created a structure where formation of the bridging μ-H ligand was inhibited. In order to utilize these ligands in a biomimetic complex that has comparable catalytic activity to the native enzyme, some other feature should be included to modulate the bond length between Ni-Fe so it better maintains the geometry of the core active site structure, which has once again been shown to be the main factor in the catalytic function of the enzyme. However, Cp should occupy an entire hemisphere, or replace 3 ligands, therefore further work analyzing the effect of replacing the 2 CN and 1 CO ligands are required to get a better representation of the influence of these ligands.

Finally, analysis of the bidentate dithiolate bridged ligands indicates an increase in reaction energy, most likely due to the S-S dithiolate bond distances, which cause distortions in the Ni centered geometry, as indicated by the τ parameters in Table 4.4 and Table 4.5. While these ligands are unable to maintain the structural integrity of the active site in the same manner as the native Cys residues, which seems to act as a scaffold for the active site cluster $[(RS)_2Ni\mu(SR)_2Fe(CO)(CN)_2]$, it should be noted that these ligands do not affect the redox character of the enzyme. Assuming steric strain would not affect the energetics, a possible solution could be an ethane-based bidentate thiolate bridging ligand to attempt to replicate the S-S distance of the native Cys residues.

5. Fe Halogenase Chemistry

5.1 Introduction

Natural products containing halogen-carbon bonds are a diverse group of compounds that have wide usage in various applications, from pesticides to advanced materials and pharmaceuticals.[108-111] In medicine, thousands of these halogenated products have been isolated[108, 112-115] and many have been found to have antibiotic and anticancer properties.[108, 109, 115, 116] For halogenation in nature, the predominant modification is chlorination, followed by bromination, however fluorination and iodination are rare. Halogenation has been found to improve drug efficiency, potency, and selectivity, therefore medicinal chemists use stereo- and regio-specific halogenation of drug candidates to improve molecular properties in order to control tissue distribution and pharmacokinetics, or to block/redirect the drug metabolism.[108, 115, 117] One example of an important halogenated antibiotic drug is the broad spectrum antibiotic, vancomycin.[108, 112, 113, 118-120] This drug works against Gram-positive bacteria, and is used for the treatment of various infections, including methicillin-resistant *Staphylococcus aureus* (MRSA).[121] However, chlorination affects the atropisomer distribution, which is important in order to achieve the clinically active conformation.[115, 122, 123]

In order to halogenate compounds like antibiotics at ambient temperatures and non-harsh conditions, activation of unreactive species, such as saturated hydrocarbons, must be achieved. Mononuclear non-heme Fe enzymes[124-129] have been found to be involved in biological oxidative reactions, such as hydroxylation, epoxidation, desaturation, ring cleavage, and halogenation of C-H bonds.[119, 130-139] One feature of non-heme Fe enzymes is the formation of an Fe(IV)=O intermediate, which allows for the abstraction of H from an alkane followed by halogenation, or more commonly hydroxylation for other non-heme Fe enzymes.[109, 119]

Within the class of non-heme Fe enzymes is SyrB2, an α-Ketogluatarate (αKG) dependent halogenase from *Pseudomonas syringae* which is part of the biosynthetic pathway of syringomycin E, an antifungal agent. Upon substrate delivery via a prosthetic phospopantetheine (PPant) arm attached to the SyrB1 acyl carrier protein, chlorination the γ-carbon of L-Thr occurs.[109, 140-147]. The SyrB2 enzyme has a reactive center that is deeply embedded into the protective enzyme environment, and the substrate delivery process controls the specificity.[124-129] A minimal model of the SyrB1-PPant-L-Thr substrate and chlorinated product is shown in Figure 5.1.

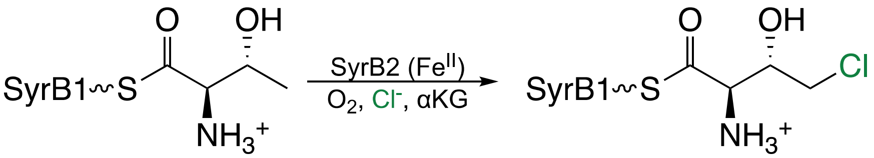

Figure 5.1: Halogenation of SyrB1-PPant-L-Thr to SyrB1-PPant-4-Cl-L-Thr Catalyzed by SyrB2.

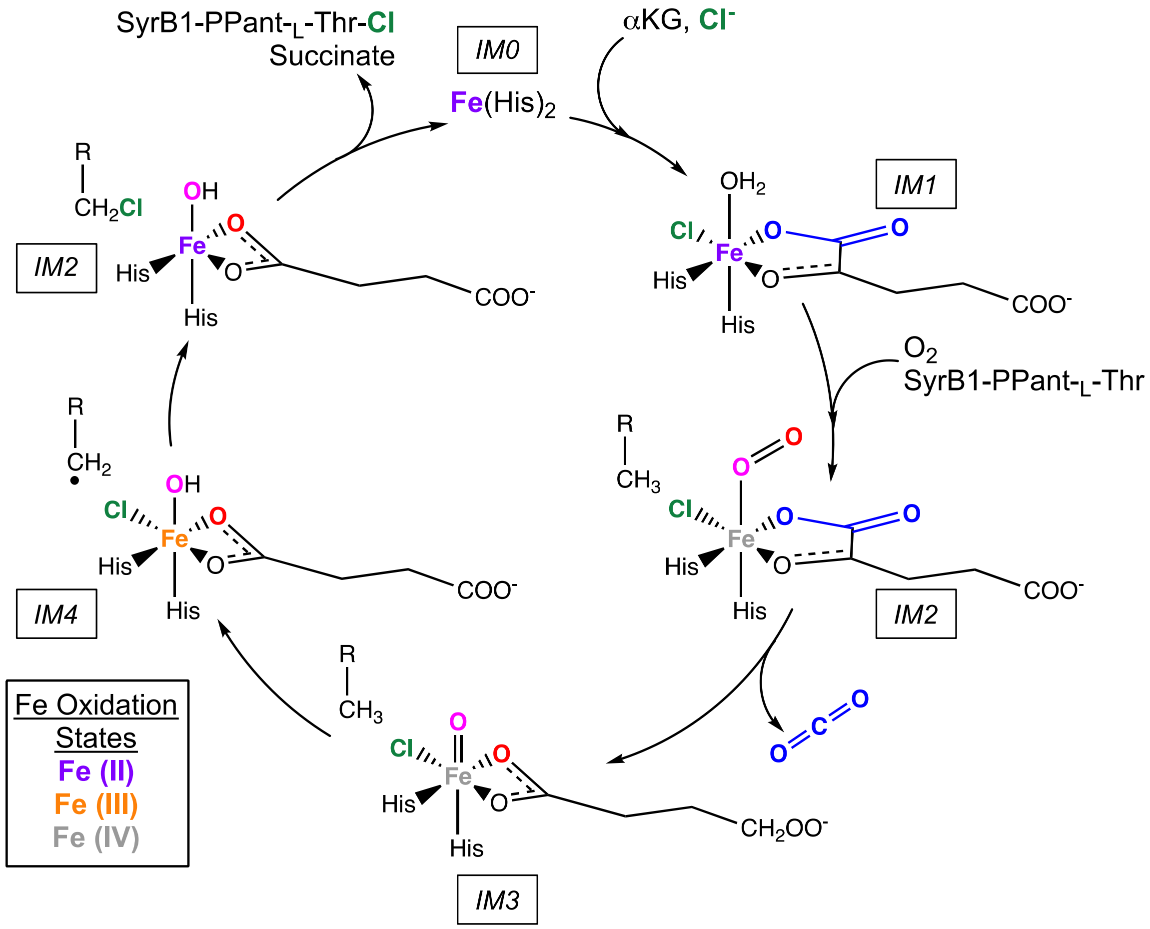

Figure 5.2: Proposed catalytic cycle of the chlorination of SyrB1-PPant-L-Thr by the non-heme Fe halogenase, SyrB2. Oxidation states of Fe are color coded. The Syr-B1-PPant-L-Thr substrate is represented by R-CH_3 in this catalytic cycle.

The active site of the SyrB2 halogenase is comprised of an Fe center coordinated to two histidine residues. Throughout the catalytic reaction, this Fe center becomes further coordinated by a Cl^- ion and the αKG ligand, which can be seen in the depiction of the proposed catalytic cycle in Figure 5.2. The αKG ligand and Cl^- anions from an aqueous NaCl solution enter the active site of the enzyme and are coordinated to the Fe center (*IM1*). During the substrate delivery step, with the substrate represented as R-CH_3, the Fe (II) center is oxidized through coordination of O_2, forming *IM2*. Upon CO_2 dissociation, the highly active Fe(IV)=O intermediate is formed, labeled *IM*3. Homolytic cleavage of a C-H bond in the L-Thr results in a $-CH_2$ radical, in addition to reduction of the Fe (IV) to Fe (III) and formation of an Fe-coordinated hydroxide (*IM4*). The Cl^- is then liberated from the Fe center via radical addition, forming a C-Cl bond and reducing Fe (III) to Fe (II) in *IM5*. Finally, the chlorinated substrate and the Fe-coordinated succinate ligand leave the active site, regenerating *IM0*.

Our experimental collaborators[148] found that the SyrB2 enzyme also has another interesting halogenation reaction – through inclusion of an amine group in the β-position relative to the carboxyl group of the αKG ligand forming the non-native N-oxalylglycine (NOG) ligand, a known inhibitor of the αKG-dependent hydroxylase enzymes,[149, 150] selective fluorination of the L-Thr in SyrB1-PPant-Thr was observed, as seen in Figure 5.3.

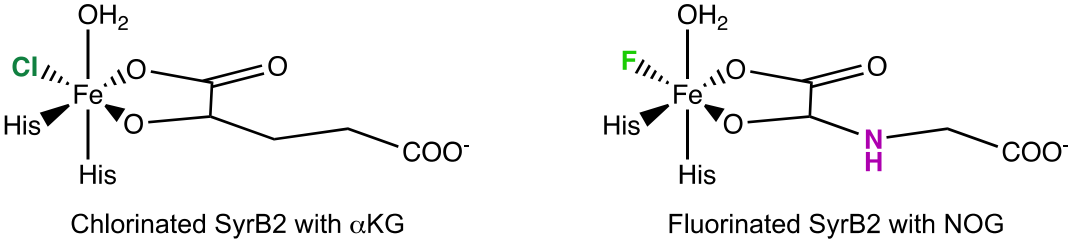

Figure 5.3: SyrB2 halogenated active site structures of IM2 (from Figure 5.2). Left: native chlorinated SyrB2 with Fe-coordinated αKG ligand. Right: non-native fluorinated SyrB2 with Fe-coordinated NOG ligand.

Considering the difficulty of C-F bond formation due to the strong electronegativity of F^- ions, which strongly interact with H_2O molecules in aqueous systems, natural fluorinated products are very rare.[111, 151, 152] As of 2019, only two examples of enzymatic C-F bond formation have been found, therefore this finding is of particular importance because formation and cleavage of C-F bonds require non-environmentally friendly methods and harsh conditions.[111, 153] Therefore, the goal of this computational study is to elucidate the mechanism of the halogenation of SyrB1-PPant-Thr, and to identify the chemical or structural properties of the SyrB2 active site that contribute to selective C-F bond formation when the αKG ligand is changed to an NOG ligand.

5.2 Computational Details

Calculations were run using Gaussian 16 suite version C01[107] for the geometry optimizations and frequency calculations using unrestricted B3LYP[154-156]/def2-SVP[65, 66] with an ultrafine grid. For all calculations XQC was used for the convergence of the SCF cycles. B3LYP was chosen as the functional based on the work performed by Altun et al. where the accuracy of CC calculations, specifically CCSDT(Q), DFT, and correlated multireference multiconfuguration ab initio methods were tested for H_2 activation by FeO^+. CCSDT(Q) was found to be an acceptable reference when compared to the available experimental data, and B3LYP had the smallest deviations from the relative energies calculated by CCSDT(Q).[7]

Grimme's DFT-D3(BJ) dispersion correction[5] was included with the revised damping parameters as stated by Smith et al.[157] Solvation was included using PCM[67] with $\varepsilon = 4$ to simulate the surrounding enzyme environment.[56, 58]

Frequency calculations were also performed to obtain thermodynamic corrections, and any frequencies less than 50 cm^{-1} were shifted.

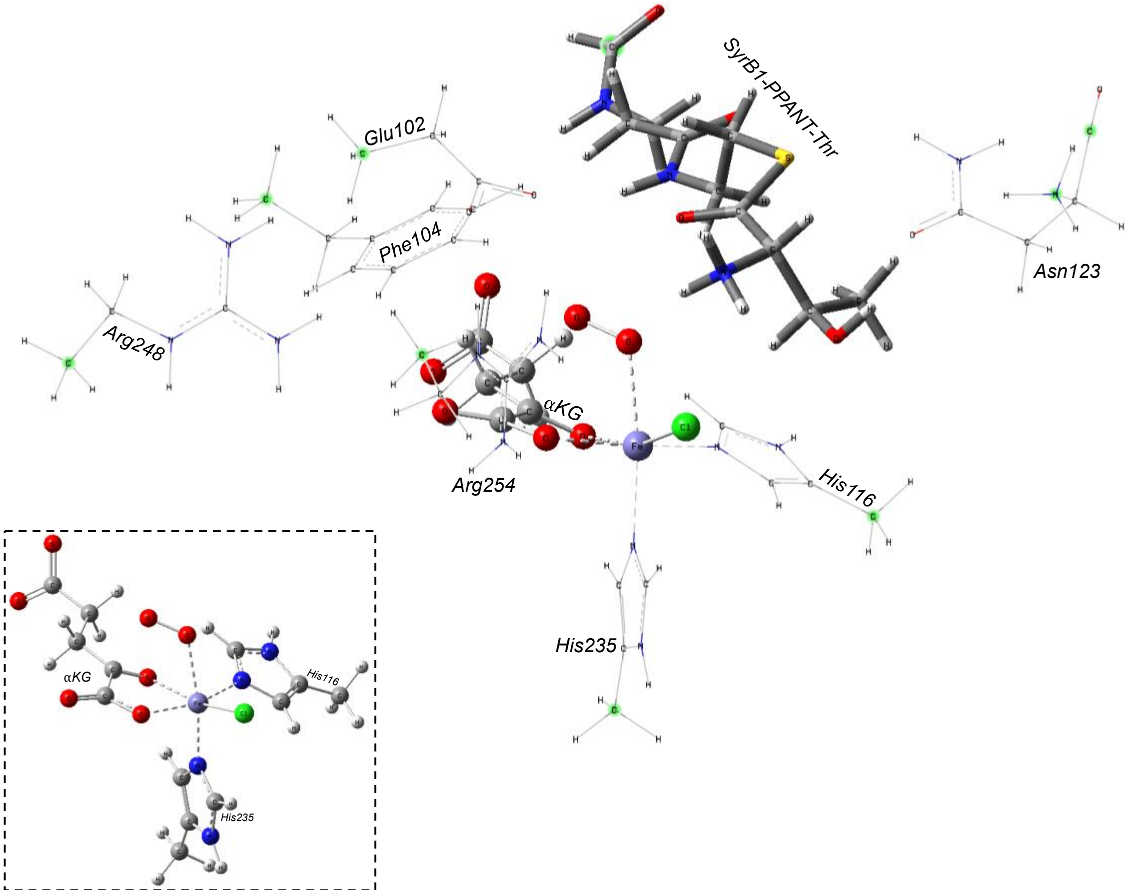

Figure 5.4: Model of *IM2* of the active site of SyrB2 utilized for calculation of *IM2-IM5* (Figure 5.2). The first coordination sphere of the Fe was included – Fe, Cl-. His115, His 235, αKG, and O_2, as seen in the dashed box. A truncated model of SyrB1-PPant-Thr is also included, as well as highly conserved residues Glu102, Phe104, Asn123, Arg248, and Arg254. The constraints on the amino acid residues are shown as atoms highlighted in green.

The computational model used to study *IM2-IM5* (from Figure 5.2) is shown in Figure 5.4. The specific intermediate shown is Fe-O_2 coordinated *IM2*. The Fe coordination sphere (excluding the His residues) are shown in the ball-and-stick drawing, which include the Fe center, the halogen, the αKG ligand, and the O_2

molecule. The amino acid residues included are shown in the wireframe drawn portions of the model and include the following highly conserved residues: Fe-coordinated His115 and His 235; Glu102, Phe104, Asn123, Arg248, and Arg254. The Arg254 residue is difficult to see, as it is positioned directly in front of the αKG ligand in the orientation shown in Figure 5.4. We have also included the truncated SyrB1-PPant-L-Thr substrate, shown in the tube drawing. All of the atoms that were constrained during the geometry optimizations are highlighted in green. This model was constructed from a molecular dynamics simulation. In this simulation, all starting structures of the SyrB1/SyrB2 complex and parameters for tor the phosphopantetheinylated threonine were taken from Mehmood et al.[109] Structures were energy minimized, heated to 300K, and density equilibrated before 500 ns production runs, and each system was performed in triplicate.

For computational study of the binding affinity of the halogens in *IM1*, a modified version of the model shown in Figure 5.4 was constructed, seeing as the substrate is not yet interacting with the system in *IM1*. To study the binding of halogens to Fe(II) in the enzyme matrix, explicit water molecules were included to determine the energy required to remove a water molecule from a microsolvated halide system in order for the halide to coordinate to the Fe center. This was done through comparison of the intermediate solvated with four water molecules with a halide solvated by five explicit water molecules with an implicit solvation model simulating an aqueous solution. To calculate this binding affinity, we used:

$$\Delta G_{X\cdot H_2O\ bind} = \left(G_{IM1+4H_2O} + G_{H_2O}\right) - \left(G_{IM1-X} + G_{X^-+5H_2O}\right) \qquad (5.1)$$

where G_{IM1+4H_2O} is *IM1* solvated by four explicit water molecules, G_{H_2O} is the free energy of a single water molecule, G_{IM1-X} is *IM1* without the halogen and no explicit water molecules, and $G_{X^-+5H_2O}$ is the halide with five explicit water molecules. All of these values were calculated including the dispersion corrections and implicit solvation described previously. These calculations were performed with uB3LYP/def2-TZVP.[65, 66]

Finally, in preliminary studies, the spin state of the catalytic cycle was analyzed by testing the triplet, quintet, and septet states due to the spin contamination values from initial calculations. However, upon further analysis, the quintet state was the lowest energy pathway for the majority of the intermediates, and when compared to the literature for another non-heme Fe halogenase, WelO5,[119] the quintet pathway was chosen for all the models and intermediates studied.

5.3 Results and Discussion

5.3.1 Halide Binding to Fe in *IM1*

In order to analyze the effect of including the NOG ligand as an alternative to the αKG ligand, we analyzed the Natural Bond Orbital (NBO) charges of the atoms in the ligand, as well as the Fe center and the halide for the intermediate prior to substrate delivery, *IM1*. The three ligand/halide combinations tested were the two systems of interest, the wild type αKG/Cl and the modified catalytically active NOG/F, as well as two other combinations, NOG/Cl and αKG/F, for comparison of the effect of the ligand and halide. The free energy of halide binding to *IM1* was also tested in order to assess whether changing the Fe-coordinated ligand from αKG to NOG affected the binding affinity of the F⁻. This causes the F⁻ to coordinate to Fe (II) from the aqueous NaF solution in order for the SyrB2 enzyme to fluorinate the SyrB1-PPant-L-Thr substrate. The results of the charge analysis are indicative of electronic stabilization from the inclusion of the amine group, which allows for charge modulation of the resonant X-Fe-Ligand complex. The binding affinities of the halides show that binding is favorable among all the models assessed. The charge results are shown in Figure 5.5, and the associated binding affinities are reported in Table 5.2.

The NBO charges show the effect of the resonance stabilization of the inclusion of the amine functional group in the NOG ligand. In the native αKG/Cl and the αKG/F models, we see consistency in the NBO charges of the atoms in the αKG ligand, namely that the C in the γ-position and the carbonyl C have the same charges (-0.51 and 0.53, respectively). We also see similarities in the charges for Fe-coordinated carbonyl O, -0.61 for αKG/Cl and -0.63 for αKG/F, as well as the Fe-coordinated carboxylate O, -0.79 for αKG/Cl and -0.80 αKG/F. Comparison of the halide partial charges is consistent with chemical intuition – fluorine is more electronegative than chlorine, therefore we would expect a more negative partial charge on F⁻ (-0.69 in αKG/F) compared to Cl⁻ (-0.66 in αKG/Cl), however these charge differences are minimal. Finally, we look to the partial charge of the Fe for both models. In the αKG/Cl model, the Fe has a partial charge value of 1.12, which is less positive than the subsequent charge on the Fe in αKG/F, 1.18.

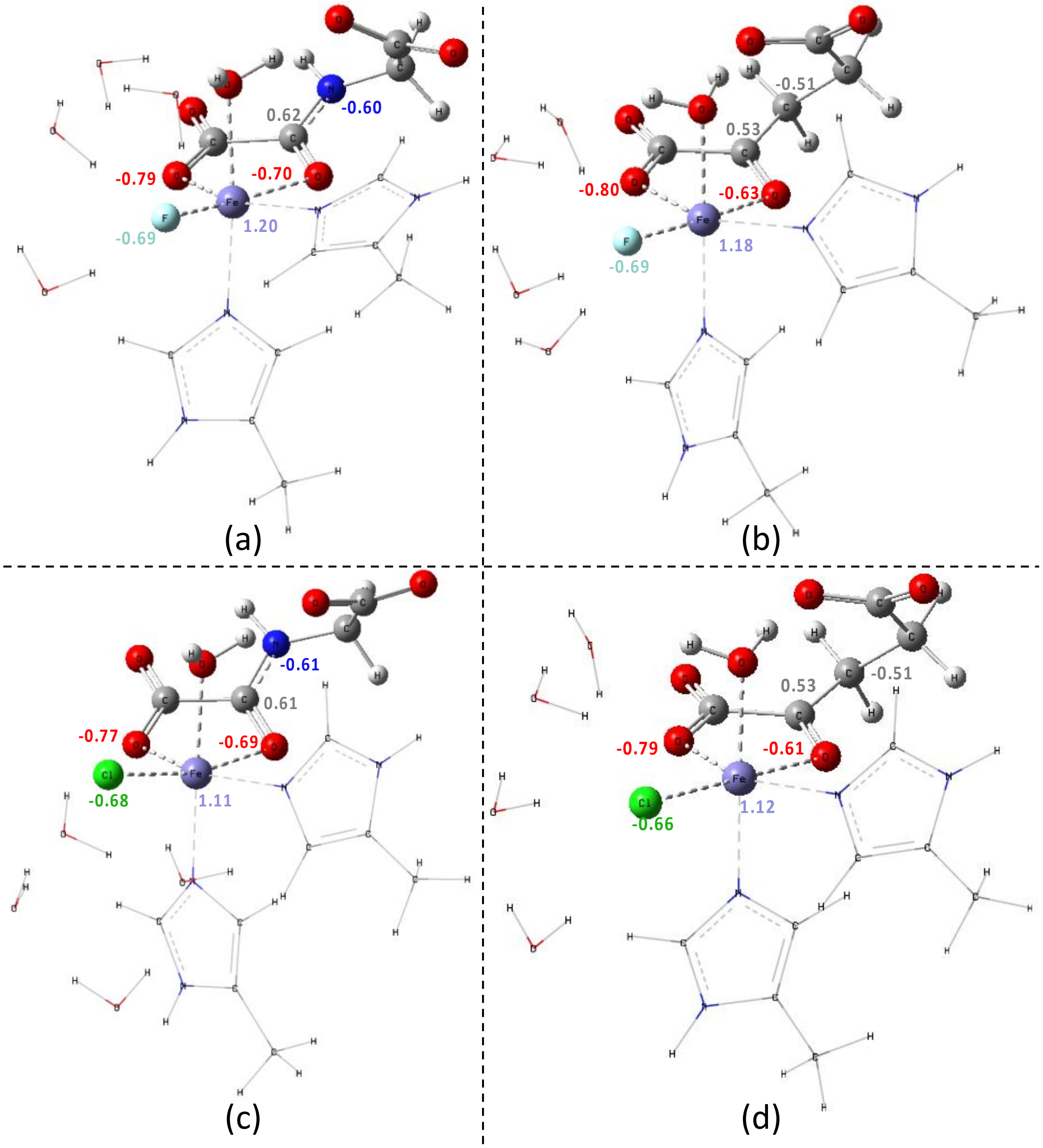

Figure 5.5: The NBO charge analysis for the minimal IM1 model for the various halide/ligand combinations tested. (a) is NOG/F, (b) is αKG/F, (c) is NOG/Cl, and (d) is the native αKG/Cl.

When we compare the αKG models (Figure 5.5b&d) to the NOG models (Figure 5.5a&c), we see differences, but not large ones. The partial charge of the F^- ion is -0.69, the same as the αKG/F model, as is the charge on the Fe-coordinated carboxylate O (-0.80). The partial charge on the Cl is -0.68, which is slightly more negative than the αKG/Cl, however the carboxylate O is slightly less negative in the NOG/Cl (-0.77). For the other atoms analyzed, we do see some changes. The N of the amide group in the γ-position of the NOG ligand is more negative than the γ-C atom in the αKG ligand for all models tested, which follows electronegativity trends. However, this additional negative charge can be seen influencing the now-conjugated amide group, namely that the carbonyl C is more positive at 0.62 for NOG/F and 0.61 for NOG/Cl. The carbonyl O is also more negative at -0.70 (NOG/F) and -0.69 (NOG/Cl). The charge on the Fe is only slightly more positive than the αKG/F model at 1.20, therefore we can assume that the additional charge density from the amide pulls charge density from the Fe center, allowing F to bind more easily to the more positive Fe. However, the more negative Cl^- in NOG/Cl does not influence the partial charge on Fe, seeing as the value for NOG/Cl is 1.11 and 1.12 for αKG/Cl.

Table 5.1: Sum of selected partial charges for the NBO charge analysis of the three ligand combinations tested for IM1 in Figure 2.1.

	NOG/F	**αKG/F**	**NOG/Cl**	**αKG/Cl**
Fe^{2+}	1.20	1.18	1.11	1.12
$O_{carbonyl}$	-0.70	-0.63	-0.69	-0.61
X^-	-0.69	-0.69	-0.68	-0.66
Sum	-0.19	-0.14	-0.26	-0.15

Another way to analyze this data is to add the partial charges of the X-Fe-O moiety together to assess the influence of these changes, which can be found in Table 5.1. The values of the sum of the Fe, carbonyl O, and halogen do not differ by more than 0.12 charge units, which is surprising considering fluorination is observed for NOG/F but not observed with αKG/F. It is also unexpected that the most negative of the models is the NOG/Cl, but this could indicate that it is too negative and therefore no longer in the optimal charged position for halogen binding. The influence of the NOG ligand was found to cause both NOG models to have the most negative partial charge sum compared to the αKG-containing models, which is indicative of the influence of the new amide functional group that could allow for initial binding of the F^- ion, but an unfavorable charged region for Cl^-. Further calculations would need to be performed to probe this phenomenon.

Another metric analyzed for *IM1* was the free energy of halogenation of the Fe center, as defined by eq. 5.1. This free energy value includes the binding free energy of the halogen, as well as the energetics necessary to overcome hydration. Interestingly, the binding affinity seems to depend on the halogen, not the ligand. This is apparent through observation of the free energy values reported in Table 5.2.

Table 5.2: Free energy of halogenation of Fe in SyrB2 as calculated by eq. 5.1.

Ligand/Halogen Combo	**$\Delta G_{X\,bind}$ (eq. 5.1) kcal/mol**
αKG/Cl	-7.7
NOG/Cl	-3.6
αKG/F	-11.2
NOG/F	-12.1

Both values for the fluoride models show energies more negative than -10 kcal/mol, whereas both models tested with chloride are less negative than -10 kcal/mol, meaning that Cl binds weaker to Fe than F regardless of the choice of ligand. When we compare the two halide models to each other, αKG/Cl to NOG/Cl and αKG/F to NOG/F, we do see an interesting trend. The αKG/Cl model binds more easily to the Fe compared to the NOG/Cl by 4.1 kcal/mol, and the NOG/F binds more easily to the Fe than the αKG/F by 0.9 kcal/mol. While the difference in free energies for the F models is small, it does indicate a preference for the NOG/F combination, just as the Cl models show a preference for the αKG/Cl combination.

The stronger binding of F^- models compared to Cl^- models could be explained by the charge analysis results and electronegativity trends. For the two models with Cl^-, the Fe has a charge of 1.11 to 1.12 whereas the models with F^- have Fe partial charges of 1.18 and 1.20. F^- is more electronegative than Cl^-, and the more electronegative F^- causes a more electropositive Fe due to the electron withdrawing nature of the F^- when compared to the Cl^- models. While Cl^- is also very electronegative, the influence of the Cl^- on the Fe is not as strong as F^-, leading to a less electropositive Fe (II) and an overall weaker coordination. This is supported by the charge analysis of the NOG/Cl model, where the Cl^- has a slightly more negative partial charge compared to the native αKG/Cl (-0.68 and -0.66, respectively) however the charge on the Fe is barely affected (1.11 for NOG/Cl and 1.12 αKG/Cl).

5.3.2 Halogenase Mechanism

The mechanism for the catalytic cycles was studied for *IM2* to *IM5*, however *IM2* is more thoroughly being analyzed currently due to a possible geometric issue regarding the torsion of the unbound carboxylate group in the αKG and NOG ligands, therefore our analysis will focus on catalysis from the ferryl intermediate, *IM3*, to halogenation of the ʟ-Thr residue. We find that the NOG/F system follows a similar energy path to the native αKG/Cl system, and in the case that formation of *IM3* occurs, the subsequent hydrogen abstraction by the Fe(IV)=O will most likely occur followed by halogenation of the radical –CH2 group. These results are shown in Figure 5.6.

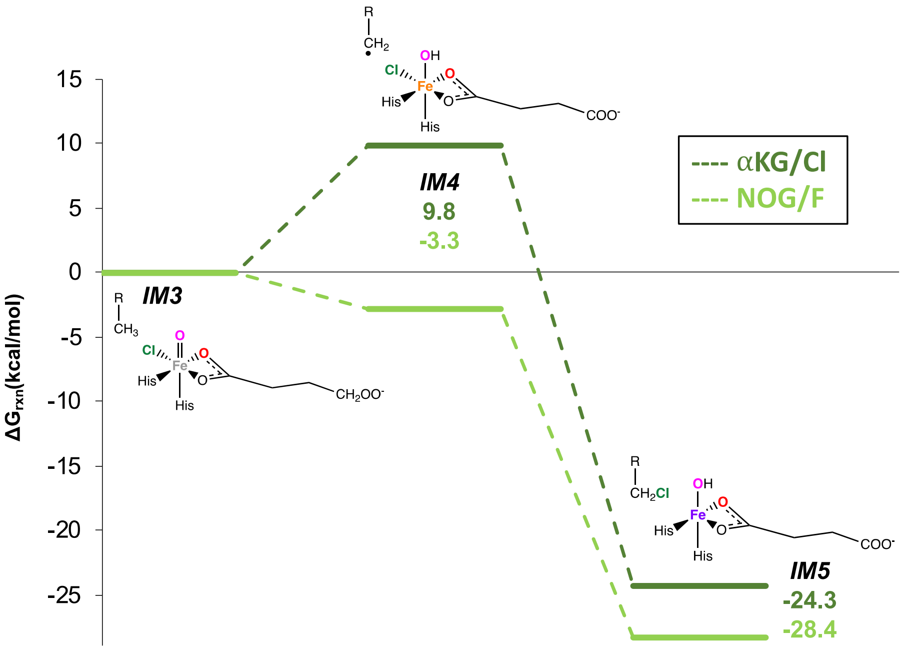

Figure 5.6: Free energy reaction profile of catalysis from *IM3*-*IM5* for SyrB2 halogenase, reported relative to *IM3* in kcal/mol. (Dark Green): The native αKG/Cl model, (Light Green): the NOG/F model. The structural images of the active site are indicative of the native enzyme system.

In the reaction profile, the free energies for the αKG/Cl and NOG/F systems are plotted for *IM3*-*IM5*. The reaction profiles are very similar, with an overall exergonically favorable pathway. In *IM4*, surprisingly the hydrogen abstraction step is downhill by 3.3 kcal/mol for NOG/F whereas the native αKG/Cl *IM4* (9.8 kcal/mol) is 13.1 kcal/mol higher in energy than the NOG/F system. The increased stability of the NOG/F state could be attributed to the additional electronic stability from the more electron-donating NOG ligand, therefore stabilizing the high spin (S=3/2) ferric intermediate more than the αKG/Cl, however the DFT calculation for the NOG/F model does have significant spin contamination (S^2=7.01) indicating that the calculation does have contribution from higher spin states, compared to the αKG/Cl (S^2=6.04).

Additionally, the hydroxylation potential of the NOG/F model was calculated by swapping the positions of the F^- and OH^- groups in order to assess whether the active site could feasibly undergo a reorientation to allow for hydroxylation of the L-Thr residue. Work performed by Huang et al. performed similar anaylsis of this competitive pathway,[158] and this competition is also seen in a different non-heme Fe halogenase enzyme, Wel05.[119] The results indicate that hydroxylation for the NOG/F model is unlikely, as the reoriented system is 14.2 kcal/mol higher in energy than *IM4*. This transformation and the energies of the two intermediates can be found in Figure 5.7. Further calculations are in progress to determine the possibility of hydroxylation in the native αKG/Cl model for SyrB2.

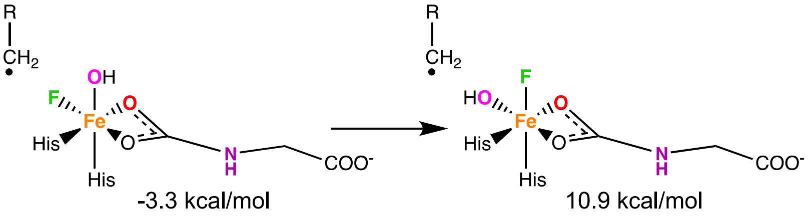

Figure 5.7: *IM4* Fe-centered reorientation of F^- and OH^- to assess viability of hydroxylation of the radical $-CH_2$ group. The structure on the left is the structure of *IM4* for NOG/F, and the structure on the right is the F^-/OH^- reorientation. The associated energies of the intermediates are set relative to *IM3*.

After the hydride abstraction step, *IM4*, the halogenation of the ʟ-Thr residue occurs in *IM5*. Transition state calculations were attempted to isolate the barrier for the transition from IM4 to IM5, however the imaginary frequencies of the current transition states indicate a coupled reaction between the Fe-X-CH_2 transition and an HO-H-H_2N transition of the Fe-OH ligand with the NH_3 group of the ʟ-Thr residue amino acid backbone. Further studies into the transition state between IM4 and IM5 are being studied, including a manual scan of the Fe-X-CH_2 transition to determine whether the halogenation is a barrierless transition, which preliminary results indicate at this time.

For the formation of *IM5*, as can be seen in the reaction profile (Figure 5.6), the halogenation step is exergonic by 34.1 kcal/mol in αKG/Cl and 25.1 kcal/mol in NOG/F. This leads to the conclusion that should the ferryl Fe(IV)=O intermediate IM3 form, it is highly likely that hydrogen abstraction and the subsequent halogenation steps will occur.

Work is currently ongoing for this study, including study of the position of the non-Fe-bound carboxylate tail of the αKG or NOG ligand, isolation of a concerted reaction pathway transition state between *IM2* and *IM3* for the formation of the ferryl Fe(IV)=O intermediate, and mechanistic studies for the other model systems mentioned, αKG/F and NOG/Cl.

5.4 Conclusion

In this section, we studied the non-heme Fe halogenase SyrB2, which natively chlorinates the L-Thr residue of the substrate SyrB1-PPant-L-Thr system for the potential to fluorinate the substrate with slight modification of the enzyme. Specifically, modification of the native αKG ligand to an NOG ligand has been experimentally shown to be active in fluorination. While this work is still ongoing, we have found that the Cl^- binds more strongly to Fe in the presence of αKG as opposed to NOG, whereas the F^- binds more strongly to Fe in the presence of NOG as opposed to αKG. The overall binding energy indicates the F^- models bind more strongly to the Fe than Cl^- models, but this can be attributed to the influence of the difference in electronegativity of the halides on the partial charge of the Fe. The NBO charges of the various ligand/halide combinations were also studied, but no conclusive results were found regarding the chemical reason the NOG/F combination is viable.

Finally, while analysis of the mechanism for the halogenation of the substrate is also ongoing, we can see the halogenation step is very exergonic, and assuming the formation of the highly active Fe(IV)=O intermediate, *IM3*, this reaction will proceed to form SyrB1-PPant-4-X-L-Thr where X is either Cl or F. Finally, we showed for the NOG/F ligand/halogen combination, the competing hydroxylation pathway would have to overcome a 14.2 kcal/mol reorientation, meaning the fluorination pathway is the most likely mechanism and that the competing hydroxylation pathway is unlikely to occur. Currently, ongoing work for this system includes analysis of the competing hydroxylation pathway for the other ligand/halogen combinations, as well as determination of the mechanism through isolation of transition states.

6. Ti-Catalyzed Synthesis of Carbodiimides from Nitrene Transfer Reactions with Isocyanides

6.1 Introduction

Transition metal-catalyzed nitrene transfer reactions are efficient and highly atom economical routes for the synthesis of nitrogen-containing molecules.[159-162] There are many examples of transition metal-catalyzed nitrene transfer using Rh[163-166], Ag[167], and late transition metal porphyrin complexes.[168-170] However, there are significantly fewer examples of catalytic nitrene transfer reactions with early transition metals. This is partly because the reactivity of high-valent early transition metal imido (M≡NR) complexes is dominated by redox-neutral reactions such as [2+2]-cycloaddition and 1,2-addition.[171-174] Recently, we have demonstrated that azobenzene can be used as an oxidant in formal nitrene transfer reactions that stem from initial Ti≡NR and alkyne [2+2]-cycloaddition.[175-182] In an effort to expand the use of azobenzene as a nitrene source in catalytic reactions beyond [2+2] cycloadditions, we sought to use isocyanides as migratory insertion partners with Ti≡NR fragments *en route* to catalytic carbodiimide formation.

Carbodiimides are used as dehydration reagents in chemical synthesis,[183-185] polymer materials,[186, 187] and dyes.[188-191] Unsymmetrical carbodiimides are often synthesized via dehydration of ureas[192, 193] or dehydrosulfurization of thioureas.[194, 195] However, nitrene transfer to isocyanides is an attractive alternative as it provides a potentially more direct and atom economical alternative.[196-205]

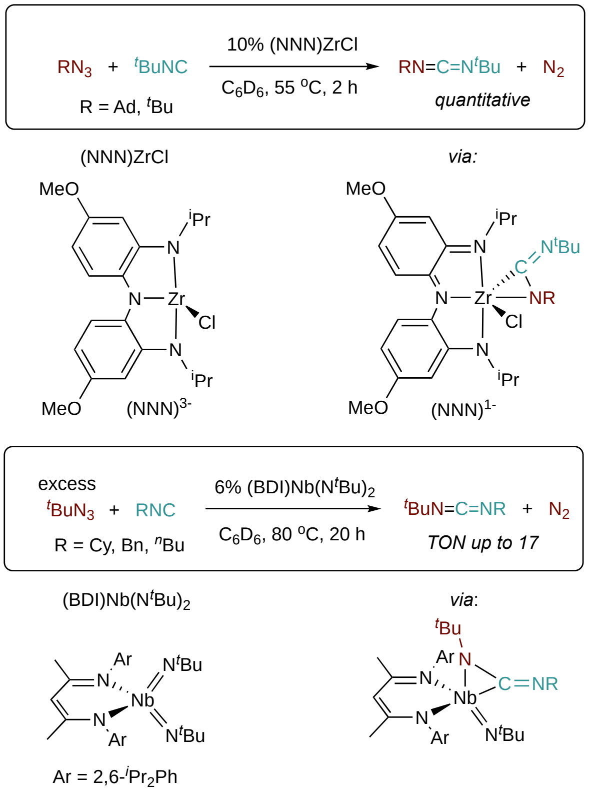

Figure 6.1: Examples of catalytic carbodiimide formation using early transition metals. Top: Redox-active ligands enable oxidation with a Zr catalyst. Bottom: π-overloading yields Nb (*bis*)imidos that are active toward isocyanide insertion. Both proceed through key η^2-carbodiimide adducts.

Reprinted with permission from Beaumier, E. P.; McGreal, M. E.; Pancoast, A. R.; Wilson, R. H.; Moore, J. T.; Graziano, B. J.; Goodpaster, J. D.; Tonks, I. A. *ACS Catalysis* **2019,** *9* (12), 11753-11762. Copyright 2019 American Chemical Society

Although there are several examples of isocyanide migratory insertions into high-valent early transition metal imidos,[206-210] there are only two examples of catalytic carbodiimide formation (Figure 6.1). In one case, Heyduk used a redox-active (*tris*)amide ligand capable of reversible reduction from an NNN^{-1} “quinonate” to an NNN^{3-} catecholate on Zr (NNN^{3-} = bis(2-isopropylamido-4-methoxyphenyl)amide).[205] A similar approach for catalytic nitrene carbonylation has been demonstrated by Wolczanski using a redox-active diamide-diimine

($dadi^{2-}$) ligand capable of reversible reduction to an ene-tetraamide $dadi^{4-}$ ligand ($dadi^{2-}$ = [-CH=N(1,2-C_6H_4)N(2,6-$^iPr_2$-C_6H_3)]$_2$).[211] In the second case, Arnold and Bergman have accomplished catalytic carbodiimide formation using a π-loading strategy with (BDI)Nb(N^tBu)$_2$ (BDI = 2,6-diisopropylphenyl-β-diketiminate),[204] where the two imido ligands competitively π-donate into the Nb center, providing a more reactive imido. Both examples of catalytic carbodiimide formation use azides as the terminal oxidant (Figure 6.1). Herein, we report that catalytic nitrene transfer from diazenes to isocyanides can be achieved with simple Ti imido halide complexes, demonstrating that the redox-noninnocence of the substrates and products are enough to stabilize otherwise high-energy low-valent intermediates.

6.2 Computational Details

Geometry optimizations were performed using the Gaussian09 program version e01.[63] Calculations were run using the restricted M06 functional[212] at the 6-311G(d,p) basis set[213] with a superfine grid, and the Solvation Model Based on Density (SMD) model[214] for $PhCF_3$ with ε = 9.18. Thermodynamic corrections were calculated with frequency analysis to be either minima (with no imaginary frequencies) or transition states (with one imaginary frequency) with temperature corrections at 388.15 K. All non-imaginary frequencies smaller than 50 cm^{-1} were shifted to 50 cm^{-1} for the thermal energy calculation to correct the fictitious large contribution caused by small frequencies due to the harmonic oscillator approximation.

The intrinsic bond orbitals (IBOs)[215, 216] were generated in MOLPRO[217, 218] using the restricted M06 functional at the 6-311G(d,p) basis set and were visualized using VMD 1.9.3.[80] The natural bond order (NBO) calculations were performed to calculate the occupation numbers for the 3d orbitals of the various ligand combination pathways. We used the NBO 5.0 program[219, 220] following the procedure for generating the d orbital occupation numbers outlined in Webster et al.[221]

6.3 Results and Discussion

6.3.1 Reaction Coordinate comparison of various ligand combinations

1,1-insertion of early metal imidos into isocyanides has been demonstrated previously,[206-210] however we wanted to explore the mechanism of this reaction in more detail to understand how ligands, substrates, and products could synergistically affect the Ti redox process. Compared to previous catalytic examples where overt redox-noninnocent ligands were used to promote catalysis,[205] here the critical factors promoting redox catalysis are less clear. Same excess kinetic measurements indicated both product inhibition and catalyst decomposition over the course of the reaction, precluding a full kinetic investigation (Beaumier et al.,[222] Figures S53 and S54). Further preliminary kinetic studies indicated very complex and intractable reaction orders. Thus, we turned to DFT calculations to give further insight into the potential speciation and energetics of catalysis.

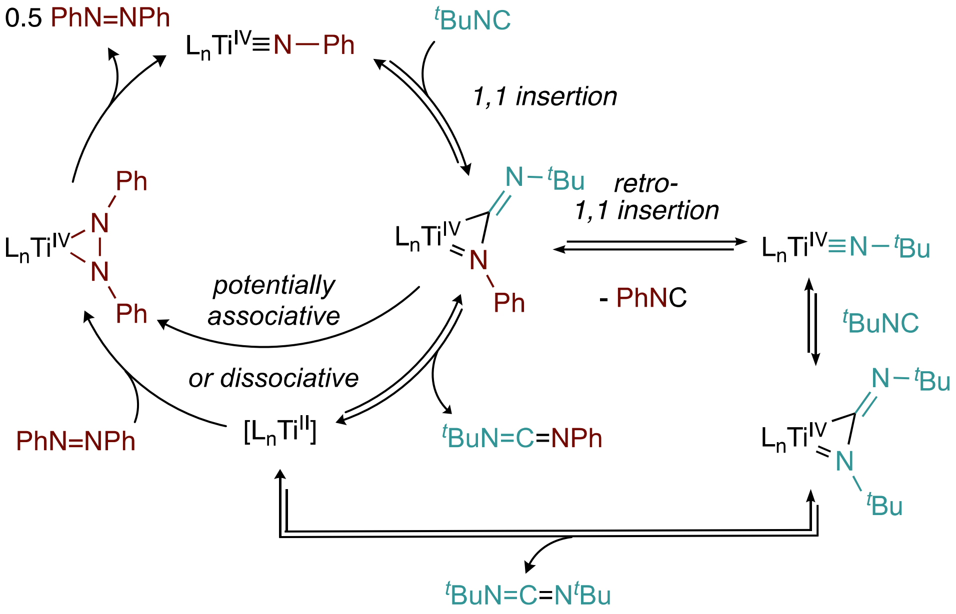

Figure 6.2: Proposed mechanism for carbodiimide formation using isocyanides and diazenes catalyzed by $[py_2TiBr_2(N^tBu)]_2$.

Reprinted with permission from Beaumier, E. P.; McGreal, M. E.; Pancoast, A. R.; Wilson, R. H.; Moore, J. T.; Graziano, B. J.; Goodpaster, J. D.; Tonks, I. A. *ACS Catalysis* **2019,** *9* (12), 11753-11762. Copyright 2019 American Chemical Society

Combined experimental and DFT results are consistent with the mechanism of 1-*tert*-butyl-3-arylcarbodiimide formation proposed in Figure 6.2. First, an isocyanide coordinates to the Ti-imido, which then undergoes a 1,1-migratory insertion into the Ti-imido bond, generating an η^2-carbodiimide. Next, substition of carbodiimide ligand with PhNNPh occurs via either an associative or dissociative manner to give the product carbodiimide and an η^2-hydrazido, which disproportionates[177, 223-226] to regenerate the Ti imido and 0.5 equiv. PhNNPh. The formation of $^tBuNCN^tBu$ *via* retro-1,1 insertion will be discussed later (*vide infra*) in Section 6.3.3.

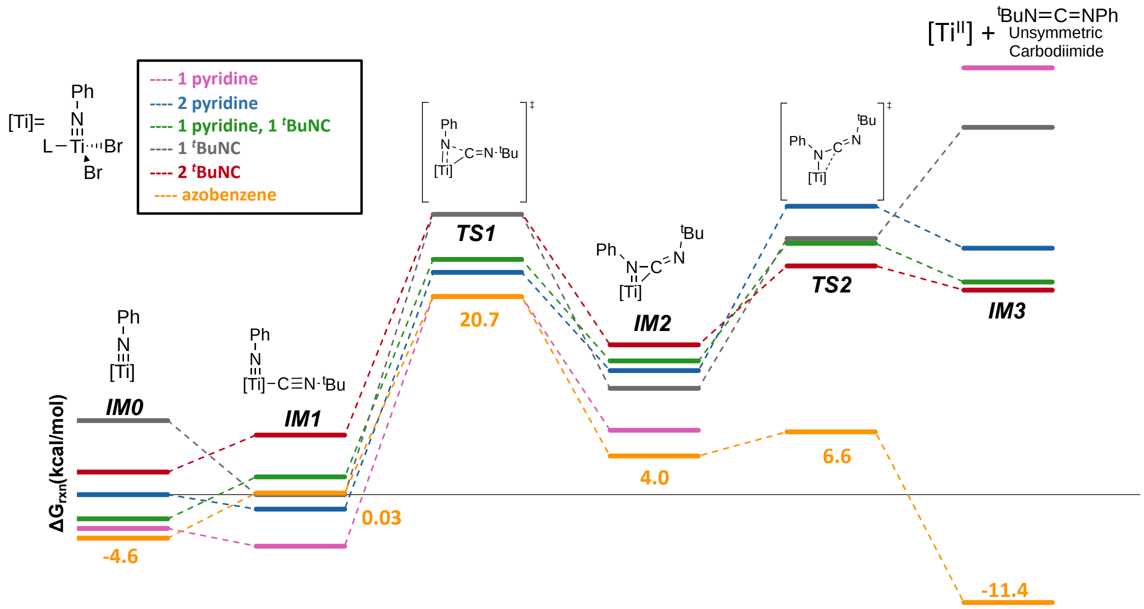

Figure 6.3: Free energy (kcal/mol) reaction profiles for various ligand combinations for isocyanide imination catalysis. Free energy values listed are for L = azobenzene. For all other free energy values, see Table 6.1.

Adapted with permission from Beaumier, E. P.; McGreal, M. E.; Pancoast, A. R.; Wilson, R. H.; Moore, J. T.; Graziano, B. J.; Goodpaster, J. D.; Tonks, I. A. *ACS Catalysis* **2019,** *9* (12), 11753-11762. Copyright 2019 American Chemical Society

A significant challenge in studying these simple Ti halide catalytic systems is the potential for speciation. Previous DFT analysis of Ti-catalyzed nitrene transfer in the [2+2+1] synthesis of pyrroles showed large energetic changes based on ligand speciation.[178] Here, pyridine (py), isocyanide, azobenzene, or carbodiimide could potentially act as a spectator ligand in some (or all) steps of catalysis. As a result, we undertook a study of the effect of various ligand combinations across the entirety of the reaction profile (Figure 6.3). The 6 spectator ligand combinations investigated were a single pyridine (**pink**), two pyridines (**blue**), pyridine/isocyanide (**green**), 1 isocyanide (**grey**), two isocyanides (**red**), and azobenzene (**orange**). In all possible ligand combinations, pathways matching the steps shown in Figure 6.2 were found to be lowest energy.

Table 6.1: Free energies (kcal/mol) for intermediates and transition states of various ligand combinations shown in Figure 3. The lowest-energy species for each intermediate/transition state is bolded and italicized.

	IM0	**IM1**	**TS1**	**IM2**	**TS2**	**IM3**
1 py	-3.7	***-5.5***	***19.8***	6.7	--	44.5
2 py	0.0	-1.6	23.2	12.8	30.1	25.8
1 py &1 ^{t}BuNC	-2.6	1.7	24.5	13.9	26.2	22.1
1 ^{t}BuNC	7.8	-0.08	29.3	11.0	26.8	38.4
2 ^{t}BuNC	2.3	6.1	29.3	15.6	23.8	21.4
PhNNPh	***-4.6***	0.03	20.7	***4.0***	***6.6***	***-11.4***

Reprinted with permission from Beaumier, E. P.; McGreal, M. E.; Pancoast, A. R.; Wilson, R. H.; Moore, J. T.; Graziano, B. J.; Goodpaster, J. D.; Tonks, I. A. *ACS Catalysis* **2019,** *9* (12), 11753-11762. Copyright 2019 American Chemical Society

The ancillary ligand combination significantly impacts the energetics of catalysis (Table 6.1). A key observation is that many possible ligand combinations are close in energy, and thus multiple species may be participating in catalysis. Most importantly, however, is that coordination of azobenzene (Figure 6.3, **orange**) significantly lowers the barrier for all steps of catalysis—in particular, there is a strong effect on product release. As will be discussed below, this is due to two factors: (1) azobenzene is not a strong σ-donor ligand, resulting in an electron-deficient Ti that facilitates 1,1-migratory insertion in **TS1**; and (2) azobenzene is a strongly π-accepting ligand and can directly accept the pair of electrons in **TS2** that were formerly backbonding into the C=N π^* of the η^2-carbodiimide ligand, cirvumenting the formation of a discrete Ti^{II} species proceeding from **TS2** to **IM3**.

This π-acceptor character can be observed in the computed azobenzene N-N bond lengths: from **IM0** through **TS2**, the N-N bond length of 1.25 Å is consistent with an N=N double bond, but upon carbodiimide dissociation it is lengthened to 1.40 Å in **IM3**.

Table 6.2: Selected calculated bond lengths (in Å) for all ligand combinations studied in the carbodiimide formation pathway for IM1, TS1, IM2, and TS2.

Ligands	Complex	Ti-N Bond Length (Å)	Ti-C Bond Length (Å)	C-N Bond Length (Å)
pyridine/pyridine	IM1	1.70	2.24	2.89
	TS1	1.76	2.02	1.71
	IM2	1.90	2.10	1.34
	TS2	2.07	2.53	1.27
pyridine/isocyanide	IM1	1.71	2.24	2.84
	TS1	1.77	2.01	1.75
	IM2	1.90	2.11	1.33
	TS2	2.07	2.53	1.27
isocyanide/isocyanide	IM1	1.71	2.25	2.85
	TS1	1.77	2.01	1.75
	IM2	1.91	2.12	1.33
	TS2	2.07	2.51	1.27
pyridine	IM1	1.69	2.24	2.79
	TS1	1.76	2.01	1.7
	IM2	1.88	2.06	1.35
isocyanide	IM1	1.69	2.24	2.82
	TS1	1.76	2.01	1.64
	IM2	1.88	2.08	1.35
	TS2	2.04	2.58	1.27
azobenzene	IM1	1.68	2.23	2.81
	TS1	1.77	2.02	1.79
	IM2	1.91	2.06	1.34
	TS2	2.29	1.92	1.34

Reprinted with permission from Beaumier, E. P.; McGreal, M. E.; Pancoast, A. R.; Wilson, R. H.; Moore, J. T.; Graziano, B. J.; Goodpaster, J. D.; Tonks, I. A. *ACS Catalysis* **2019,** *9* (12), 11753-11762. Copyright 2019 American Chemical Society

Additional bond lengths for the reaction area of the catalysis, Ti-N, Ti-C, and C-N, were analyzed and presented below in Table 6.2 for all ligand combinations tested. In general, as the carbodiimide is formed and released, the Ti-N bond length increases, the C-N bond length decreases, and the Ti-C shortens then elongates on the release of the carbodiimide. There is one notable deviation in the **TS2** bond lengths for the azobenzene ligand catalyst. Shown below in the NBO analysis (Table 6.3), the Ti(IV) does not reduce to Ti(II) upon dissociation of the carbodiimide product, which explains the difference in the **TS2** geometry. This geometry has a shorter Ti-C bond length than the other ligand combinations tested, and a longer Ti-N bond. The C-N bond length for the azobenzene **TS2** is the same as the azobenzene C-N bond length in **IM2**.

6.3.2 IBO and NBO Analysis

Next, IBO analysis was carried out on the reaction pathway with ligated azobenzene (Figure 6.4). IBOs provide a connection between DFT calculations and the curved arrow formalism[215, 216] and give a simple view of electron flow during a reaction. For the 1,1-insertion step (Figure 6.4A, **IM1** proceeding through **TS1** to **IM2**) an electron pair on one of the Ti≡NR π-bonding orbitals (blue) attacks the isocyanide C=N π* orbital, forming the new C=N bond and pushing an electron pair on to N (red). This type of Ti≡N π to C-N σ bond-forming event is reminiscent of our recent report on [2+2+1] pyrrole formation[178] where C-N bond formation occurs through π orbitals in an electrocyclization event. For the product release step (Figure 6.4B, **IM2** proceeding through **TS2** to **IM3**), the azobenzene π-acceptor character is very important. Here **TS2** involves 3 critical orbital changes: (1) breaking of the ^{t}BuNC-Ti σ bond to form the product carbodiimide C=N π bond (orange), (2) breaking of the Ti=NPh π bond to form a new π backbond with azobenzene (orange), and (3) breaking of the Ti-NPh σ-bond to form the carbodiimide N lone pair (purple).

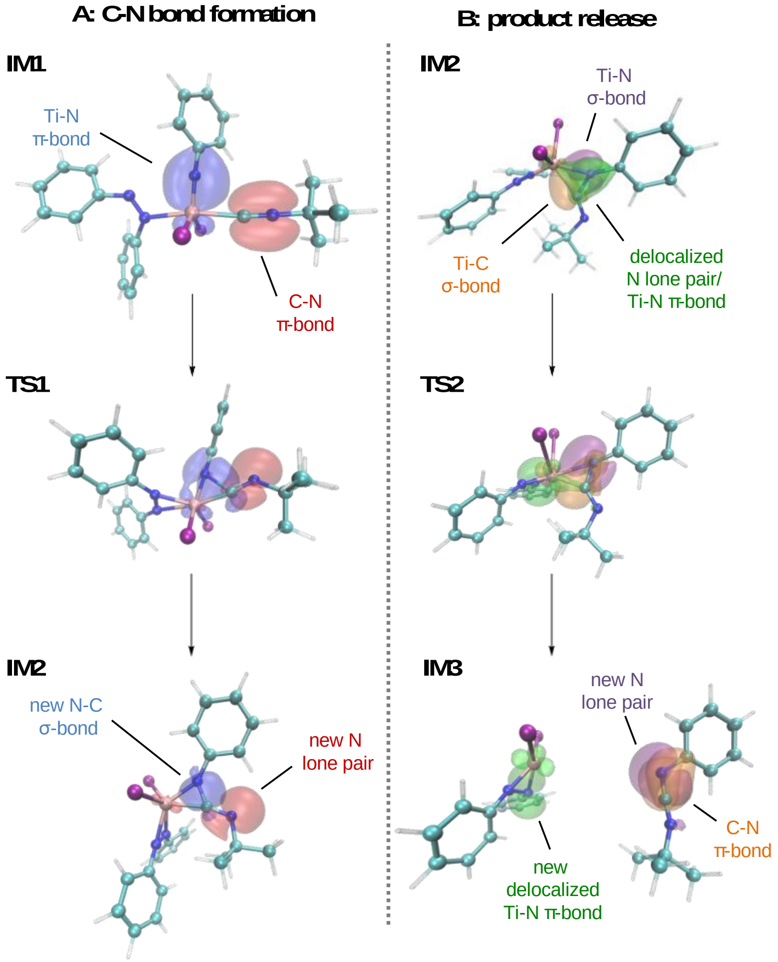

Figure 6.4: (A) IBOs of the reactant (IM1), transition state (TS1), and product (IM2) in the first step of isocyanide imination. The IBOs show the Ti-N π-bond forming a new N-C σ bond (blue orbital) and the C-N π-bond forming a new N lone pair (red orbital). (B) IBOs from the intermediate (IM2), transition state (TS2), and final dissociated product (IM3). The IBOs show the Ti-N σ bond breaking to form a new N lone pair (purple orbital), the Ti-C σ bond breaking to form a new C=N π-bond (orange orbital), and a delocalized N lone pair/Ti-N π-bond transferring through the titanium to form a new Ti-N π-bond with azobenzene (green orbital).

Reprinted with permission from Beaumier, E. P.; McGreal, M. E.; Pancoast, A. R.; Wilson, R. H.; Moore, J. T.; Graziano, B. J.; Goodpaster, J. D.; Tonks, I. A. *ACS Catalysis* **2019,** *9* (12), 11753-11762. Copyright 2019 American Chemical Society

Table 6.3: NBO derived Ti $3d_{z}^{2}$ occupancies of calculated intermediates. Values closer to 0.4 (black) are assigned as formally Ti (IV) while closer to 0.6 (red) are assigned as formally Ti (II). Values between 0.4 and 0.6 are shown in (pink).

Ligands	**Complex**	**Occupation Numbers**	**Formal Oxidation State**
pyridine/pyridine	IM0	0.31	+4
	IM1	0.31	+4
	TS1	0.35	+4
	IM2	0.44	+4
	TS2	**0.65**	+2
	IM3	**0.63**	+2
pyridine/isocyanide	IM0	0.30	+4
	IM1	0.32	+4
	TS1	0.36	+4
	IM2	0.46	+4
	TS2	**0.56**	+2/+4
	IM3	**0.62**	+2
isocyanide/isocyanide	IM0	0.31	+4
	IM1	0.32	+4
	TS1	0.37	+4
	IM2	0.47	+4
	TS2	**0.57**	+2/+4
	IM3	**0.62**	+2
pyridine	IM0	0.32	+4
	IM1	0.31	+4
	TS1	0.36	+4
	IM2	0.45	+4
	TS2	no optimized geometry	
	IM3	**0.76**	+2
isocyanide	IM0	0.32	+4
	IM1	0.31	+4
	TS1	0.39	+4
	IM2	0.45	+4
	TS2	**0.58**	+2/+4
	IM3	**0.67**	+2
azobenzene	IM0	0.31	+4
	IM1	0.31	+4
	TS1	0.35	+4
	IM2	0.44	+4
	TS2	0.40	+4
	IM3	0.39	+4

Reprinted with permission from Beaumier, E. P.; McGreal, M. E.; Pancoast, A. R.; Wilson, R. H.; Moore, J. T.; Graziano, B. J.; Goodpaster, J. D.; Tonks, I. A. *ACS Catalysis* **2019,** *9* (12), 11753-11762. Copyright 2019 American Chemical Society

NBO analysis[219, 220] further supports the importance of the azobenzene π-acceptor character. Previously, we have benchmarked formal Ti oxidation states by examining the occupancy of the Ti $3d_{z}^{2}$ orbital through NBO analysis, where occupancies closer to 0.4 correlate well to formal Ti^{IV}, and occupancies closer to 0.6 correlate well to formal Ti^{II}. The $3d_{z}^{2}$ occupancies of all intermediate ligand combinations, as well as for the 1,1-insertion and product dissociation transition states **TS1** and **TS2**, are presented in Table 6.3. Here, structures with weaker donors (pyridine, azobenzene) have lower $3d_{z}^{2}$ occupancy in **TS1** (correlating to a more oxidized Ti metal center) and thus undergo more facile 1,1-insertion with isocyanide. Additionally, structures with π-accepting ligands (isocyanide, azobenzene) have lower $3d_{z}^{2}$ occupancy in **TS2**, making ligand loss more facile as the building charge on the Ti^{II} fragment can be simultaneously buffered by the π-accepting ligands. Importantly, Ti remains significantly more oxidized when azobenzene is a ligand because the weak N=N π bond is an excellent π-acceptor—in fact, by NBO analysis of the $3d_{z}^{2}$ occupancy, Ti remains close to the +4 oxidation state throughout catalysis when azobenzene is bound.

Azobenzene's synergistic "redox-neutral" buffering of electron density serves the same purpose as an ancillary redox noninnocent ligand and was previously proposed by Wang for several other Ti redox catalytic reactions.[227, 228] Interestingly, previous computations for pyrrole product release from Ti^{II} in the related catalytic formal [2+2+1] synthesis of pyrroles does not require this type of buffering.[178] While the reasons for this difference are currently unclear, a contributing factor could be the stability of the released product: in the case of pyrrole release, reformation of the aromatic ring (loss of Ti-pyrrole backbonding) could be enough of a driving force to eject Ti^{II} even in the absence of azobenzene as a redox buffer; on the contrary, in carbodiimide synthesis (and the related carboamination reactions calculated by Wang[228]), formation of a single C=N π bond is likely not enough of a driving force to eject free Ti^{II}. Nonetheless, it is also important to note that the other (non-azobenzene bound) pathways are low enough in energy (~25 kcal/mol, Table 6.1) that they also may contribute to the overall reaction rate to some extent, and that azobenzene is not absolutely critical for catalysis.

6.3.3 Analysis of Competing Mechanisms

Next, we investigated the formation of the "nitrene scrambled" ^{t}BuNCN^{t}Bu byproducts that were observed in all reactions with ^{t}BuNC. Notably, when using catalysts $py_3TiBr_2(NPh)$ and $(THF)_3TiI_2(NPh)$ (Table 1, entries 2 and 3 from Beaumier et al.[222]; Figure 6.5), ^{t}BuNCN^{t}Bu was still formed in 8% and 9% yield, respectively. These results demonstrate that ^{t}BuNCN^{t}Bu formation is not solely generated from stoichiometric reaction of the ^{t}Bu imido group of the precatalyst.

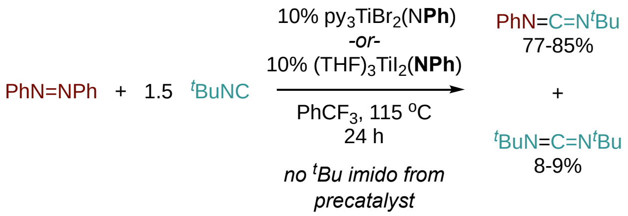

Figure 6.5: Formation of ^{t}BuNCN^{t}Bu using catalytic precurser 2 or 3, $py_3TiBr_2(NPh)$ or $(THF)_3TiI_2(NPh)$ respectively, demonstrates that this side product is not solely formed from Ti(N^{t}Bu) precatalyst activation.

Reprinted with permission from Beaumier, E. P.; McGreal, M. E.; Pancoast, A. R.; Wilson, R. H.; Moore, J. T.; Graziano, B. J.; Goodpaster, J. D.; Tonks, I. A. *ACS Catalysis* **2019,** *9* (12), 11753-11762. Copyright 2019 American Chemical Society

A process in which the nitrene fragments are formally scrambled could reasonably occur through either an isocyanide metathesis or carbodiimide metathesis pathway (Figure 6.6). In an isocyanide metathesis, a Ti≡NPh imido undergoes a 1,1-insertion with ^{t}BuNC to form an η^2-carbodiimide. Instead of undergoing ligand dissociation to liberate the carbodiimide product, the η^2-carbodiimide undergoes *retro*-1,1 insertion to liberate PhNC and a Ti≡N^{t}Bu imido, which can react further with ^{t}BuNC to yield ^{t}BuNCN^{t}Bu (Figure 6.6, top). In a carbodiimide metathesis pathway, an equivalent of ^{t}BuNCNPh product undergoes [2+2] cycloaddition with a Ti≡NPh imido, ultimately liberating PhNCNPh and the Ti≡N^{t}Bu imido necessary to yield ^{t}BuNCN^{t}Bu (Figure 6.6, bottom). There is only a single report of d^0 metal imido promoted isocyanide metathesis.[204] On the contrary, there are both stoichiometric[229-231] and catalytic[232-235] examples of carbodiimide metathesis with d^0 metal imidos, although dihalide Ti imidos have been shown to be poor catalysts for this transformation.[234] Experimentally, we have not observed either of the expected byproducts of these pathways, PhNC or PhNCNPh, in significant quantities, although control experiments indicate that both pathways may be operable (Beaumier et al.[222] SI, Figure S52).

Figure 6.7 shows the DFT-calculated free energy profiles of isocyanide metathesis (green) and carbodiimide metathesis (red) catalyzed by $py_2TiBr_2(N^tBu)$. In the isocyanide metathesis pathway (Figure 6.7, green), the first steps of the reaction are identical to productive carbodiimide formation (Figure 6.3, **IM0** through **IM2**), where ^{t}BuNC first coordinates to the Ti≡NPh imido followed by imido 1,1-

insertion into the Ti-isocyanide bond, yielding an η^2-carbodiimide (**IM2**). From here, the Ti rearranges to the adjacent C=N^{t}Bu π-bond, resulting in an isomeric η^2-carbodiimide structure (**IM3-ICM**) of almost equal energy to **IM2**. **IM3-ICM** next undergoes rate-determining (27.2 kcal/mol) *retro*-1,1 insertion, yielding a Ti≡N^{t}Bu imido with a bound PhNC ligand (**IM4-ICM**), which can dissociate to yield the free Ti≡N^{t}Bu imido **IM5-ICM**. In the carbodiimide metathesis pathway (Figure 6.7, red), the starting Ti≡NPh imido **IM0** undergoes [2+2] cycloaddition with PhNCN^{t}Bu, yielding the guanadinate **IM2-CM**. **IM2-CM** then undergoes rate-determining (34.7 kcal/mol) *retro*-[2+2] cycloaddition in the opposite manner, yielding the Ti≡N^{t}Bu imido **IM3-CM** with the expulsion of PhNCNPh.

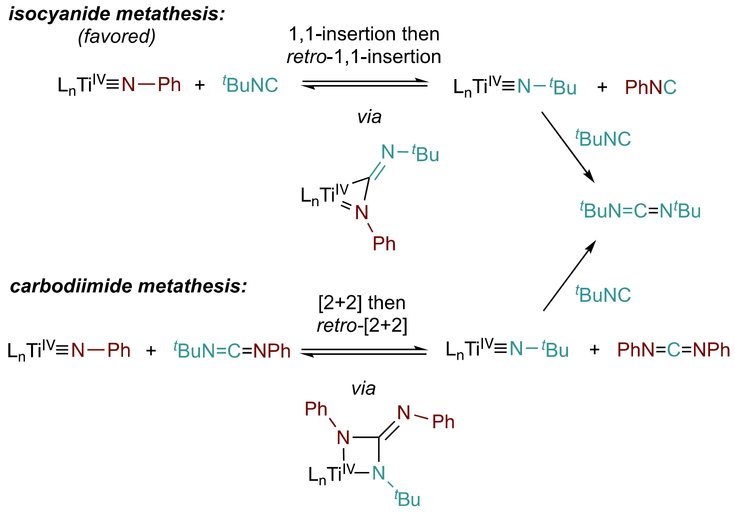

Figure 6.6: Possible mechanisms leading to formation of Ti tert-butyl imido moieties responsible for catalytic production of ^{t}BuNCN^{t}Bu.

Reprinted with permission from Beaumier, E. P.; McGreal, M. E.; Pancoast, A. R.; Wilson, R. H.; Moore, J. T.; Graziano, B. J.; Goodpaster, J. D.; Tonks, I. A. *ACS Catalysis* **2019,** *9* (12), 11753-11762. Copyright 2019 American Chemical Society

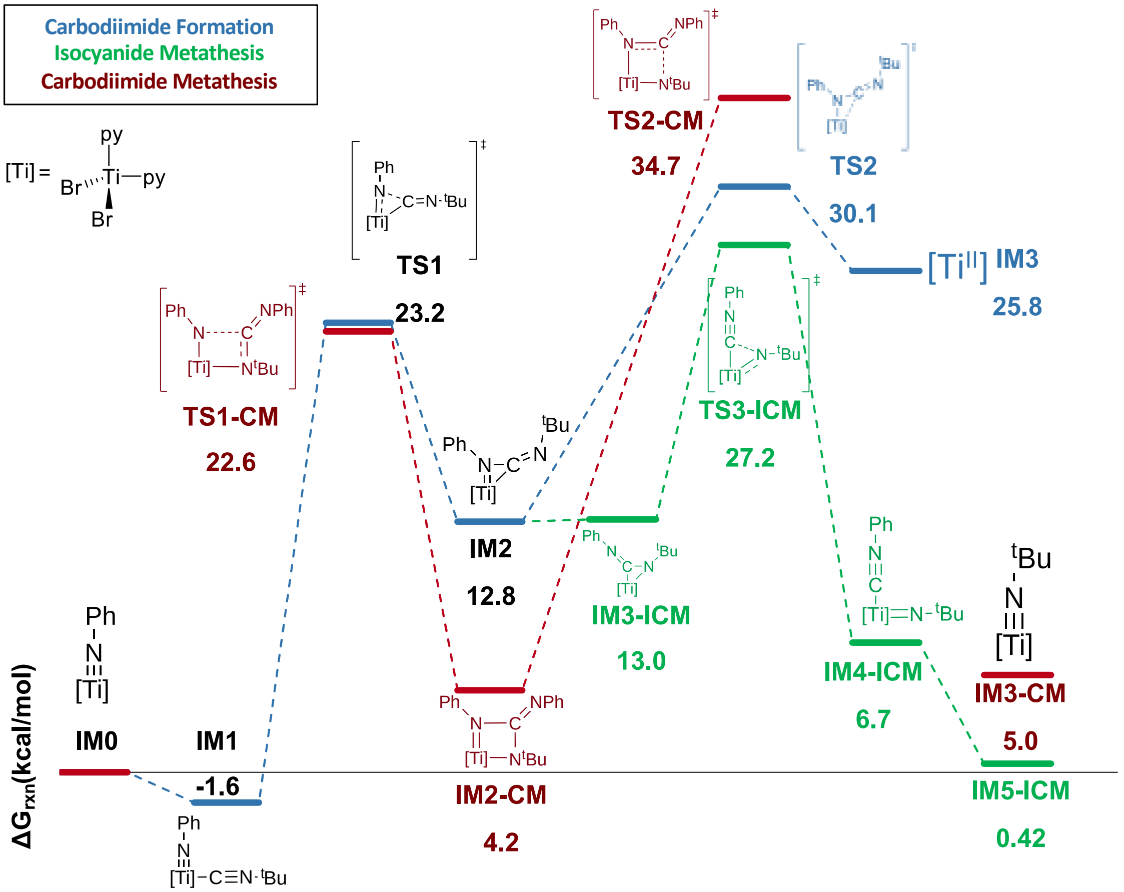

Figure 6.7: Free energy profiles of possible mechanisms leading to formation of Ti tert-butyl imido moieties responsible for catalytic production of ^{t}BuNCN^{t}Bu. Blue: carbodiimide formation, same as $Br_2Ti(NPh)py_2$ from Figure 6.3 (blue). Green: isocyanide metathesis with ^{t}BuNC. Red: carbodiimide metathesis with PhNCN^{t}Bu.

Adapted with permission from Beaumier, E. P.; McGreal, M. E.; Pancoast, A. R.; Wilson, R. H.; Moore, J. T.; Graziano, B. J.; Goodpaster, J. D.; Tonks, I. A. *ACS Catalysis* **2019,** *9* (12), 11753-11762. Copyright 2019 American Chemical Society

Comparing the scrambling pathways, the rate-determining barrier for isocyanide metathesis (**TS3-ICM**, 27.2 kcal/mol) is significantly lower than for carbodiimide metathesis (**TS2-CM**, 34.7 kcal/mol), indicating that isocyanide metathesis is the likely major pathway of scrambling. The computed rate-determining step for productive unsymmetrical carbodiimide formation (Figure 6.7

blue and Table 6.1, **TS2**, 2 py, 30.1 kcal/mol) is slightly higher than **TS3-ICM** for isocyanide metathesis. However, these calculations were performed with 2 ancillary pyridine ligands, and upon ligand exchange to azobenzene the productive redox pathway to unsymmetrical product is much lower in energy (Table 6.1, **TS2**, 1 azobenzene, 6.6 kcal/mol). Since isocyanide and carbodiimide metatheses are redox neutral pathways, coordination of azobenzene will not significantly change the barrier for **TS3-ICM** or **TS2-CM** (by analogy, as seen in Figure 6.3, and Table 6.1, the barrier for **TS1** changes < 5 kcal/mol moving from py_2 ligation to azobenzene ligation). Thus, productive catalysis will in most cases kinetically outcompete isocyanide metathesis if azobenzene is present, accounting for the low yields of the symmetrical ^{t}BuNCN^{t}Bu byproduct.

6.4 Conclusion

In conclusion, we have demonstrated that catalytic nitrene transfer to isocyanides using diazenes or azides can be accomplished with the simple Ti imido halide complex $[Br_2Ti(N^tBu)py_2]_2$. DFT analysis of the reaction profile suggests that during the initial steps of isocyanide coordination to Ti and 1,1 migratory insertion, the ligand environment around Ti is somewhat ambiguous, showing similar barriers for several possible ligand combinations. Alternatively, the carbodiimide dissociation step likely proceeds while Ti is bound to a diazene ligand in an overall associative ligand exchange process, given that the barrier for carbodiimide dissociation is significantly lower with this combination than all other possibilities probed. The low barrier for azobenzene-bound Ti to dissociate an η^2-

carbodiimide is a result of the azobenzene acting as a redox buffer, immediately accepting a pair of electrons upon dissociation of the η^2-carbodiimide and circumventing a discrete Ti^{II} intermediate.

In addition, the unanticipated formation of the symmetrical carbodiimide ^{t}BuNCN^{t}Bu, a byproduct observed during catalysis, was proposed to form via a rare isocyanide metathesis mechanism evidenced through both experiment and DFT analysis. This is only the second report of an isocyanide metathesis in the literature. Importantly, this study indicates that substrates that can participate in synergistic backbonding/redox buffering to significantly reduce the barrier for overall redox processes, which may provide further avenues for exploring early transition metal redox catalysis outside of more classical redox noninnocent ligand designs.

7. Quantifying Chemical Hardness of Anions

7.1 Introduction

Supramolecular anion recognition is the study of structures and functions of the resultant supermolecules from the binding of anions to molecular receptors.[236, 237] Supramolecular recognition of anions in water is key to the design of molecular probes for their detection and of receptors for their sequestration and transport which have applications in both medical and environmental fields.[238-244]

Lanthanide complexes have multiple benefits as probes for anions such as phosphates[245-257], carbonates[246, 247, 258-262], fluorides[263-266], cyanides[267, 268], and certain carboxylates[245-248, 269-272]. Lanthanides are favored for practicality due to their labile nature, meaning these metal ions exchange ligands rapidly.[273, 274] Among such metal-based receptors for anions, lanthanide complexes with open coordination sites are uniquely promising since both their magnetic and luminescent properties are affected by anion coordination. Therefore, lanthanide-based receptors for anions can also behave as molecular sensors. For example, gadolinium (III) complexes have been used as relaxivity probes or responsive MRI contrast agents.[275, 276]

The difficulty in designing lanthanide-based probes is to establish selectivity for one anion over competing ones. To date, developing lanthanide-based receptors for a desired anion with high affinity and selectivity remains, for the most part, serendipitous. Some features that have been found to influence the binding and selectivity have been isolated, such as ligand geometry, steric hindrance at the binding site, and Coulombic interactions. However, the geometry of the complex is not convincing enough justification for many of the observed anion selectivity by lanthanide complexes. For certain Gd (III) containing complexes, specifically Gd2 from Figure 7.1, the open coordination sites have little steric hindrance for anions[277, 278], however this complex has no affinity for carbonates, phosphates, or fluorides and weak affinity for oxalate.[279] Surprisingly another species, Gd1 (Figure 7.1), which has nearly a nearly identical geometric structure to Gd2, has high affinity for phosphates but a weak affinity for bicarbonate.[257]

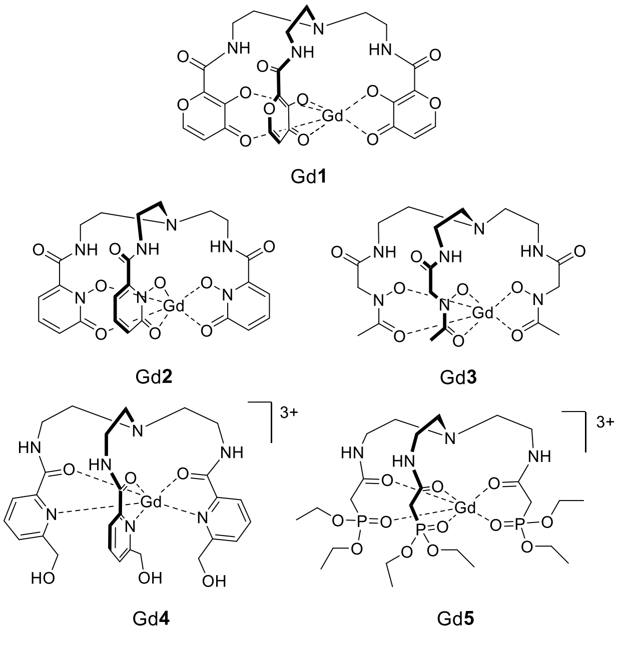

Gd**1**

Gd**2**

Gd**3**

Gd**4**

Gd**5**

Figure 7.1: Chemical structures of tripodal Gd (III) complexes for anion recognition.

Reprinted with permission from Raju, M. V. R.; Wilharm, R. K.; Dresel, M. J.; McGreal, M. E.; Mansergh, J. P.; Marting, S. T.; Goodpaster, J. D.; Pierre, V. C. *Inorganic Chemistry* **2019,** *58* (22), 15189-15201. Copyright 2019 American Chemical Society

To further elucidate properties that affect anion affinity for these Gd (III) complexes, properties such as hydration free energy, basicity, and molecular radius were probed. Additionally, absolute chemical hardness[280] was calculated using computational methods for a series of anions in solution to assess the binding affinity of these specific anions to a lanthanide containing complexes, specifically the Gd (III) complexes which contain tris-bidentate chelating ligands shown in Figure 7.1.[237]

Hardness is a property that describes the resistance to changes in electronic configuration of chemical complexes. This property, along with electronegativity, is considered an indicator of chemical reactivity and stability, making it of interest for studying various trends among chemical systems. Mathematically, it is defined as the second derivative of the energy of the system, E, with respect to N number of electrons at a constant external potential (υ):

$$\eta = \frac{1}{2}\left(\frac{\partial^2 E}{\partial N^2}\right)_{\upsilon} \tag{6.1}$$

The electronic chemical potential of the system is the first derivative of the energy with respect to N number of electrons at a constant external potential, similar to hardness.

$$\mu = \left(\frac{\partial E}{\partial N}\right)_{\upsilon} \tag{6.2}$$

This definition of chemical potential suffers from N integer discontinuity, which causes different values of the derivative for the removal or addition of electrons. These are estimated by finite differences, so Parr and Pearson[281] proposed an operational definition of chemical hardness (eq. 6.3).

$$\eta = \frac{I-A}{2} \tag{6.3}$$

$$I = E_{N-1} - E_N \tag{6.4}$$

$$A = E_N - E_{N+1} \tag{6.5}$$

In this definition, I is the vertical ionization energy (eq. 6.4), and A is vertical electron affinity (eq. 6.5). E_N refers to the energy of the neutral system (N), whereas $N + 1$ is the anionic species and $N - 1$ is the cationic species.

There is some difficulty in computationally calculating the chemical hardness of anions with DFT. First, anions are unstable due to the electron detachment, meaning it cannot be described with a standard DFT total energy calculation. A standard DFT calculation can reasonably estimate relative trends in hardness with a medium sized basis set, but this is an artificial phenomenon caused by the binding of the electron due to the finite basis set. The addition of diffuse functions to the basis set do improve this by allowing electrons to leave the system for continuum or dipole bound states; however this causes the electron affinity, A, to approach zero, causing chemical hardness and potential to approach I /2.[280]

Setting electron affinity to zero is an alternative approach; however, this leads to hardness being equivalent to the negative chemical potential, meaning there is no need to distinguish between the two quantities. Physically, this means the gain and loss of electrons are treated equally in the definition of hardness. However, this excludes ions that exhibit strong bias towards unidirectional flow of charge. So, if A is highly negative, it is resistant to the uptake of charge (also yielding high chemical hardness) which is not captured when $A = 0$. One could include explicit negative electron affinities; however, this broadens the scale of hardness. Instead, one can use a Koopman-type theorem[282, 283] to rewrite chemical hardness (eq. 6.6) and potential (eq. 6.7) using KS-DFT orbital energies,

$$\eta = \frac{\varepsilon_{\mathrm{LUMO}} - \varepsilon_{\mathrm{HOMO}}}{2} \tag{6.6}$$

$$\mu = \frac{\varepsilon_{\mathrm{HOMO}} + \varepsilon_{\mathrm{LUMO}}}{2} \; . \tag{6.7}$$

Large errors are found when using these equations, even though relative information for a series of systems or molecules are reliable. Tozer and De Proft[284] found that the errors associated with local functionals for equation 6 can be understood from studying the integer discontinuity problem previously mentioned. They propose that, assuming local functionals average over the discontinuity, if one includes the relationships between the $N+1$ and $N-1$ sides of N, the following equation can be used with local functionals:

$$\eta = \frac{\varepsilon_{\mathrm{LUMO}} - \varepsilon_{\mathrm{HOMO}}}{2} + (\varepsilon_{\mathrm{HOMO}} + I) \tag{6.8}$$

One of the main benefits of this equation for hardness is the lack an explicit calculation of electron affinity, requiring only two KS calculations on E_N and E_{N-1}. Additionally, this formalism creates an unconventional definition of electron affinity,

$$A = -(\varepsilon_{\mathrm{LUMO}} + \varepsilon_{\mathrm{HOMO}}) - I. \tag{6.9}$$

When electron affinity was calculated using equation 6.9, De Proft et al. found a mean absolute error of 0.49 eV for electron affinity when compared to conventional definitions (such as eq. 6.5). Additionally, using this method of calculating chemical hardness, trends in chemical hardness were consistent with chemical intuition and experimental gas phase hardness values of corresponding radicals.[280]

7.2 Computational Details

The calculations were performed in the MOLPRO 2015 program.[217, 218] Single point energy calculations were performed on the neutral, cationic, and anionic species with the PBE[285] DFT functional and the aug-cc-pVTZ[286-288] basis set. Additionally, the COSMO[289] model within MOLPRO was used to incorporate the effect of solvent.

The values in Table 7.1 were calculated using the equations found in the previous section. Vertical ionization energy, I, was calculated as shown in eq. 6.4 using the difference in energy between the cationic (E_{N-1}) and neutral species (E_N). Chemical hardness was then calculated using eq. 6.8, which requires I, $\varepsilon_{\mathrm{HOMO}}$, and $\varepsilon_{\mathrm{LUMO}}$.

7.3 Results and Discussion

The experimental work found that complex Gd1 (Figure 7.1) had an affinity for only four anions: strong affinities for phosphate and arsenate, and weak affinities for fluoride and bicarbonate, whereas Gd2, which has a similar geometry and the same charge as Gd1, does not have any affinity for these anions. To explain this phenomenon, we turn to certain properties, such as absolute hardness (Table 7.1), Gibbs free energy of hydration, radius of the anion, and the pK_a of the conjugate acid of the coordinating ions, which are reported in Table 7.2.[237]

The computational data for this project is shown below in Table 7.1, where the reported values of chemical hardness for F^-, HCO_3^-, HPO_4^{2-}, $H_2PO_4^-$, $HAsO_4^{2-}$, and $H_2AsO_4^-$ are presented.

Table 7.1: HOMO and LUMO orbital energies, Ionization Energy (I), and hardness (η) of anions calculated at PBE/aug-cc-pVTZ with COSMO solvation, reported in eV.

Anion	$\boldsymbol{\varepsilon}_{\mathbf{HOMO}}$	$\boldsymbol{\varepsilon}_{\mathbf{LUMO}}$	$\boldsymbol{I}$ (eq. 6.4)	$\boldsymbol{\eta}$ (eq. 6.8)
F^-	-5.72	2.45	7.45	5.81
HCO_3^-	-5.25	-0.37	6.34	3.52
HPO_4^{2-}	-4.46	-0.38	5.19	2.77
$H_2PO_4^-$	-5.93	-0.68	6.78	3.48
$HAsO_4^{2-}$	-4.83	-0.78	5.49	2.68
$H_2AsO_4^-$	-6.05	-1.34	6.91	3.22

Reprinted with permission from Raju, M. V. R.; Wilharm, R. K.; Dresel, M. J.; McGreal, M. E.; Mansergh, J. P.; Marting, S. T.; Goodpaster, J. D.; Pierre, V. C. *Inorganic Chemistry* **2019,** *58* (22), 15189-15201. Copyright 2019 American Chemical Society

The fluoride anion, as expected via chemical intuition, has the highest hardness value at 5.81 eV. Additionally, our values for the various properties shown in Table 7.1 are almost the same as reported in the literature proposing this method of calculating hardness, the deviations attributed to the difference in implicit solvation models and computational software used.[280]

The order of anion hardness, from increasing to decreasing, matches what one would expect based on chemical intuition.

$$F^- > HCO_3^- > H_2PO_4^- > H_2AsO_4^- > HPO_4^{2-} > HAsO_4^{2-}$$

Hard bases are typically small, compact, and nonpolarizable. Additionally, more negative charge means a system is more easily polarizable, so would lead to softer bases. Based on this information, it makes sense that the P containing anions are harder than the corresponding As containing anions since P is smaller than As, and that the anions with a net -2 charge are softer than the anions with a net -1 charge since they are more easily polarized. HCO_3^- is both smaller than P and As and less polarizable than the -2 charged anions, so that placement follows chemical intuition as well.

The calculated absolute hardness, while following chemical intuition, does not fit the observed trend for anion affinity for Gd1. As previously stated, Gd1 only weakly associates with fluoride anions, which were found to be the hardest of the calculated anions, while the same complex has a stronger affinity for the softer phosphate and arsenate anions. Lanthanides are considered hard acids following Pearson's hard and soft acid-base theory,[290] therefore the stronger anion affinity for the softer bases is unexpected.

Table 7.2: Gibbs Free Energy of Hydration, Radius, and pK_a of Conjugate Acid of Coordinating Anions.

	$\Delta G^\circ_{hydration}$ (kJ/mol)	Radius (Å)	pK_a of conjugate acid
HPO_4^{2-}	-465	2.38	7.2
$H_2PO_4^-$	-	-	2.1
$HAsO_4^{2-}$	-	2.48	6.94
$H_2AsO_4^-$	-	-	2.2
HCO_3^-	-335	1.56	6.3
F^-	-465	1.26	3.21

Adapted with permission from Raju, M. V. R.; Wilharm, R. K.; Dresel, M. J.; McGreal, M. E.; Mansergh, J. P.; Marting, S. T.; Goodpaster, J. D.; Pierre, V. C. *Inorganic Chemistry* **2019,** *58* (22), 15189-15201. Copyright 2019 American Chemical Society

Additionally, due to the stronger affinity for the larger phosphate and arsenate ions compared to the smaller fluoride anion, the anion affinities are likely not related to the size of the anion nor the steric hindrance of the coordinated ligands. Finally, the hydration energies between $H_2PO_4^-$ and F^- are nearly identical at 298K (-465 kJ/mol for both anions shown in Table 7.2), therefore this is also unlikely to explain the observed selectivity of Gd1.

There is, however, a trend between the selectivity of Gd1 for anions and the basicity of the anion. Considering only the monoprotic form of phosphate and arsenate, the trend in basicity of the anions: $HPO_4^{2-} > HAsO_4^{2-} > HCO_3^- > F^-$, is identical to that observed for the affinity of Gd1 for the anions. Gd1 has no significant affinity for any of the other anions tested.

Importantly, the trend observed with Gd1 also holds for the other tripodal complexes. Gd3, a complex that also has the same charge and similar geometry to Gd1 and Gd2, shows the same trend in its affinity for anions: $HPO_4^{2-} > HAsO_4^{2-} > HCO_3^- > F^-$. Phosphate, in this case, is too strong an anion for Gd3 such that it replaces the tripodal ligand resulting in the formation of a gadolinium phosphate salt. The weaker binding arsenate still forms a quaternary complex with Gd3, replacing both water molecules that natively occupy the binding site. In this case, the conjugate acid of the tripodal ligand 3 is less acidic than the conjugate acid of ligand 1, and the corresponding Gd3 has a slightly higher affinity constant for arsenate than Gd1. As for Gd1, Gd3 also only forms ternary complexes with bicarbonate and fluoride, with similar affinities than observed with Gd1. Notably, Gd3, like Gd1 and Gd2, does not respond to the other anions, including HCO_2^-, NO_2^-, $CH_3CO_2^-$, SO_4^{2-}, NO_3^-, ClO_3^-, BrO_3^-, Cl^-, or Br^- under the conditions tested.

7.4 Conclusion

In summary, we have explored various properties associated with anion affinity for various Gd (III) containing complexes. Specifically in this chapter, we explored the differences between the Gd1 and Gd2 complexes to elucidate the phenomena that cause strong affinity of phosphates and arsenates to Gd1 but no anion affinity for Gd2. This is of particular interest considering these complexes have very similar architecture and the same overall charge. Based on the results in Table 7.1 and Table 7.2, we found that there is a trend between the anion affinities for Gd1 and the basicity of the anions that is also consistent with the anion affinity and basicity trends for Gd3, a structurally similar and charge consistent complex with Gd1. The results discussed in this chapter do not elucidate rationale for the lack of anion affinity in Gd2. However, the stability of the Gd2 complex is higher than the stability of the other Gd-containing complexes, as determined by the calculated conditional stability constants (19.3 Gd2, 15.9 Gd1, and 15.5 for Gd3), therefore the most stable of the Gd(III)-containing complexes have no affinity for coordinating anions. Further information about the stability constants can be found in the published article.[237]

While the trends in absolute chemical hardness did not match the trends in anion affinity for these Gd (III) complexes, this project also showed that computational calculation of chemical hardness is possible and follows chemical intuition. This is important for application to other future projects, as chemical hardness can be used to further characterize certain properties or trends in other complex metal systems, such as assessing whether hardness of certain charged ligands coordinated to Fe plays a role in the biomimetic mutations on the [NiFe]-hydrogenase active site as discussed in Chapter 4.

8. Conclusion

In this dissertation, various transition metal systems were studied using DFT methods to elucidate electronic information about various properties of the systems. This work has shown that high quality model systems can elucidate structural, mechanistic, functional, charge, and redox information to further knowledge about the specific chemical bond making and breaking processes involved in catalysis.

Much of the work performed was to discover the features of the [NiFe]-hydrogenase active site that catalyze the reversible hydrogen oxidation reaction. We discovered that the function and catalytic activity of the enzyme is modulated by the highly conserved structure of the active site, with the four Cys residues acting as a scaffold for H_2 binding and cleavage, and the Fe-coordinated inorganic ligands, which modulate the redox character of the active site.

In Chapter 2, we explored the various model sizes and degrees of constraint imposed on the active site, as well as the mechanism of catalysis. We found that the regeneration process of the Ni-SI_a catalyst most likely occurs through spontaneous electron ejection in the Ni-L intermediate, followed by H^+ dissociation instead of a coupled proton/electron dissociation step. From our analysis of the best models used to describe the active site of this enzyme (Models ***2C*** and ***3B***), we are also able to interpret the structure/function relationships in this catalytic process. Specifically, we found that slight changes in the $[(RS)_2Ni\mu(SR)_2Fe(CO)(CN)_2]$ core active site structure caused changes in the overall reaction energy, indicating that the geometry modulates the catalytic activity. Additionally, these various models tested also show that the Cys residue orientation is highly conserved and acts as a scaffold for the active site geometry.

In Chapter 3, we explored amino acid mutations based on some experimental work performed[29] that shows a shutdown in catalysis upon mutation of a highly conserved Arg residue to Lys. We performed calculations using model 2C from Chapter 2 with inclusion of four additional amino acid residues that were tested and shown to have significant decrease of catalytic activity. While we were unable to explain this shutdown in catalysis due to consistent overall energies for these mutated systems, we do find further evidence of the scaffold properties of the Cys residues as well as the relationship between the conserved structure of the active site and the overall catalytic activity.

The last chapter focused on [NiFe]-hydrogenase focuses on making changes to the active site inspired by biomimetic models that are currently developed. [19, 96-98, 100-102] We specifically studied the influence of manipulation of the Fe-coordinated ligands, as well as the influence of changing the bridging μ-Cys residues. We found that changing the electron donating or withdrawing nature of a CN ligand changes the redox character of the active site. Mainly, a more electron withdrawing ligand pulls the electron density away from Fe, destabilizing the Ni-Fe cooperativity which no longer has the ability to spontaneously eject an electron to the proximal [4Fe-4S] cluster; conversely, more electron donating groups donate electron density to the Fe, further stabilizing the Ni-Fe cooperativity and finding possible spontaneous electron ejection at all steps tested in the catalytic cycle. Additionally, we found that replacement of the 2 CN ligands with Cp derived groups causes unfavorable distortion of the active site structure, namely elongation of the Ni-Fe bond, which inhibits formation of the μ-H bridging ligand as well as an increase in the overall energy for catalysis. Finally, we found that changing the bridging Cys residues to the pdt-derived ligands distorts the geometry at the Ni center through elongation of the S-S distance between the bidentate dithiolate functional group compared to the native Cys residues, resulting in an increase of overall reaction energy, although these ligands do show that the redox character of the active site is unchanged compared to the native. This project is a computational experiment, where we can probe exactly how each specific change influences the catalytic and redox character of the enzyme activity to inform experimental work. Further work on the Ni-bound terminal modifications is currently being performed.

In Chapter 5, we studied another transition metal enzyme system, non-heme Fe halogenase SyrB2, which natively chlorinates the L-Thr residue of the substrate SyrB1-PPant-L-Thr system, for the potential to fluorinate the substrate with slight modification of the enzyme. Specifically, modification of the native αKG ligand to an NOG ligand has been experimentally shown to be active in fluorination. While this work is still ongoing, we have found that the Cl^- binds more strongly to Fe in the presence of αKG as opposed to NOG, whereas the F^- binds more strongly to Fe in the presence of NOG as opposed to αKG. This can be attributed to the influence of the difference in electronegativity of the halides on the partial charge of the Fe. The NBO charges of the various ligand/halide combinations were also studied but did not show any conclusive results regarding the chemical reason the NOG/F combination is viable. Finally, analysis of the mechanism for the halogenation of the substrate is also ongoing, but we can see the halogenation step is very exergonic, and assuming the formation of the highly active Fe(IV)=O intermediate, *IM3*, this reaction will proceed to form SyrB1-PPant-4-X-L-Thr where X is either Cl or F. Finally, we showed for the NOG/F ligand/halogen combination, the competing hydroxylation pathway would have to overcome a 14.2 kcal/mol reorientation, meaning the fluorination pathway is the most likely mechanism and that the competing hydroxylation pathway is unlikely to occur. Further work on this system includes analysis of the competing hydroxylation pathway for the other ligand/halogen combinations, as well as determination of the mechanism through isolation of transition states, which is currently ongoing.

In Chapter 6, we studied carbodiimide synthesis via catalytic nitrene transfer to isocyanides using diazenes or azides, and found that can be accomplished with the simple Ti imido halide complex $[Br_2Ti(N^tBu)py_2]_2$. While the initial isocyanide coordination steps indicate an ambiguous ligand environment, it was found that the carbodiimide dissociation step likely proceeds while Ti is bound to a diazene ligand in an overall associative ligand exchange process, given that the barrier for carbodiimide dissociation is significantly lower with this combination than all other possibilities probed. The low barrier for azobenzene-bound Ti to dissociate an η^2-

carbodiimide is a result of the azobenzene acting as a redox buffer, immediately accepting a pair of electrons upon dissociation of the η^2-carbodiimide and circumventing a discrete Ti^{II} intermediate. In addition, the unanticipated formation of the symmetrical carbodiimide ^{t}BuNCN^{t}Bu, a byproduct observed during catalysis, was proposed to form via a rare isocyanide metathesis mechanism evidenced through both experiment and DFT analysis. Importantly, this study showed that substrates that can participate in synergistic backbonding/redox buffering to significantly reduce the barrier for overall redox processes, which may provide further avenues for exploring early transition metal redox catalysis outside of more classical redox noninnocent ligand designs.

The final study performed in Chapter 7 explored various properties associated with anion affinity for various Gd (III) containing complexes. Specifically in this chapter, the Gd1 and Gd2 complexes were studied to elucidate the phenomena that cause strong affinity of phosphates and arsenates to Gd1 but no anion affinity for Gd2. We found that there is a trend between the anion affinities for Gd1 and the basicity of the anions that is also consistent with the anion affinity and basicity trends for Gd3. The results discussed in this chapter do not elucidate rationale for the lack of anion affinity in Gd2. However, the stability of the Gd2 complex is higher than the stability of the other Gd-containing complexes, therefore the most stable of the Gd (III)-containing complexes have no affinity for coordinating anions.

Overall, this dissertation has shown that chemical phenomena associated with transition metal catalysis can be successfully modeled and studied using DFT electronic structure methods. Additionally, these electronic structure calculations provide valuable insight into the structure/function relationships within the metalloenzyme systems studied, as well as elucidation of other synthetic catalytic processes. Calculation of chemical and physical phenomena that cannot be studied in the laboratory setting allows for collaboration and symbiosis between experiment and computation for a more complete and thorough understanding of these complex but important chemical or biochemical systems.

The field of metalloenzyme catalysis is an important field of study, as we have justified in previous chapters. These large enzyme systems were evolved to perform specific functions in the most efficient way possible, which is why scientists look to nature for inspiration for large scale synthetic catalysts.[10, 291] The evolutionary line of many of these enzymes dates back to the Hadean period when carbon fixation was necessary for the synthesis of macromolecular compounds which resulted in the creation of organic materials,[291, 292] therefore these enzymes have had over 4 billion years to evolve and optimize. In addition, metalloenzymes make up approximately half of all known enzymes,[293] with the various transition metals for the catalytically active metalloenzymes including V, Mn, Fe, Co, Ni, Cu, Mo, and W.[291] The use of computational methods for studying these systems, specifically electronic structure methods, allows for in-depth study of the bond making and breaking processes that occur within the enzyme in ways that cannot be studied in the lab. This has many benefits, from understanding what structure/function relationships exist in these systems, to predicting the influence of mutations or other structural changes, or even to providing information to inform experimentalists attempting to create biomimics for performing the various important processes in these highly active protein environments, as seen in Chapters 2-5.

From this end, there are a few logical next steps to be taken. The methods discussed throughout this thesis offer a systematic way to analyze what components are important in the active region for enzymes, and therefore can be applied to many other metalloenzymes to really understand what most strongly influences catalytic activity for those systems. One direction to take would be the study of new catalytic metalloenzyme systems. Hydrogenases have been extensively discussed here, but other enzymes with similar features, specifically FeS and (Fe,Ni)S centers, include acetyl CoA-synthase and carbon monoxide dehydrogenase.[291] Studies similar to what has been performed here could be done on these enzyme systems to elucidate important chemical and structural features that contribute to catalysis.

Another direction would be to study these enzyme systems through the lens of biomimetic inspired catalysis, as discussed in Chapter 4. Creating this “computational experiment” where specific changes are made one at a time to determine how the modification influences the enzyme, catalysis, and other properties could help influence the choices experimentalists make in lab. Experimentalists can then advise the computational chemists of changes that could feasibly be done in the lab, or what has/has not worked, creating a feedbackloop where computation informs experiment which informs computation, etc. with the eventual goal of developing new synthetic analogues that are as efficient as the enzymes they are based upon, or providing new syntheses of important compounds with milder conditions and more environmentally friendly methods.

Bibliography

1. Kohn, W.; Sham, L. J., Self-Consistent Equations Including Exchange and Correlation Effects. *Physical Review* **1965,** *140* (4A), A1133-A1138.

2. Koch, W.; Holthausen, M. C., *Elementary Quantum Chemistry The Hohenberg-Kohn Theorems The Kohn-Sham Approach*. 2001; p 3-5, 33-64.

3. Kulik, H. J.; Luehr, N.; Ufimtsev, I. S.; Martinez, T. J., Ab Initio Quantum Chemistry for Protein Structures. *The Journal of Physical Chemistry B* **2012,** *116* (41), 12501-12509.

4. Grimme, S.; Antony, J.; Ehrlich, S.; Krieg, H., A consistent and accurate ab initio parametrization of density functional dispersion correction (DFT-D) for the 94 elements H-Pu. *Journal of Chemical Physics* **2010,** *132* (15), 19.

5. Grimme, S.; Ehrlich, S.; Goerigk, L., Effect of the damping function in dispersion corrected density functional theory. *Journal of Computational Chemistry* **2011,** *32* (7), 1456-1465.

6. Delcey, M. G.; Pierloot, K.; Phung, Q. M.; Vancoillie, S.; Lindh, R.; Ryde, U., Accurate calculations of geometries and singlet-triplet energy differences for active-site models of NiFe hydrogenase. *Physical Chemistry Chemical Physics* **2014,** *16* (17), 7927-7938.

7. Altun, A.; Breidung, J.; Neese, F.; Thiel, W., Correlated Ab Initio and Density Functional Studies on H2 Activation by FeO+. *Journal of Chemical Theory and Computation* **2014,** *10* (9), 3807-3820.

8. Lubitz, W.; Ogata, H.; Rüdiger, O.; Reijerse, E., Hydrogenases. *Chemical Reviews* **2014,** *114* (8), 4081-4148.

9. Vignais, P. M.; Billoud, B.; Meyer, J., Classification and phylogeny of hydrogenases. *Fems Microbiology Reviews* **2001,** *25* (4), 455-501.

10. Vignais, P. M.; Billoud, B., Occurrence, Classification, and Biological Function of Hydrogenases: An Overview. *Chemical Reviews* **2007,** *107* (10), 4206-4272.

11. Cammack, R.; Frey, M.; Robson, R., *Hydrogen as a Fuel: Learning from Nature*. 1st Edition ed.; Taylor & Francis: London, 2001; p 267.

12. Pandelia, M. E.; Nitschke, W.; Infossi, P.; Giudici-Orticoni, M. T.; Bill, E.; Lubitz, W., Characterization of a unique FeS cluster in the electron transfer chain of the oxygen tolerant NiFe hydrogenase from Aquifex aeolicus. *Proceedings of the National Academy of Sciences of the United States of America* **2011,** *108* (15), 6097-6102.

13. Yagi, T.; Kimura, K.; Daidoji, H.; Sakai, F.; Tamura, S.; Inokuchi, H., Properties of Purified Hydrogenase from the Particulate Fraction of Desulfovibrio vulgaris, Miyazaki1. *The Journal of Biochemistry* **1976,** *79* (3), 661-671.

14. Fontecilla-Camps, J. C.; Volbeda, A.; Cavazza, C.; Nicolet, Y., Structure/Function Relationships of [NiFe]- and [FeFe]-Hydrogenases. *Chemical Reviews* **2007,** *107* (10), 4273-4303.

15. Fontecilla-Camps, J. C.; Amara, P.; Cavazza, C.; Nicolet, Y.; Volbeda, A., Structure–function relationships of anaerobic gas-processing metalloenzymes. *Nature* **2009,** *460* (7257), 814-822.

16. Ash, P. A.; Hidalgo, R.; Vincent, K. A., Proton Transfer in the Catalytic Cycle of NiFe Hydrogenases: Insight from Vibrational Spectroscopy. *ACS Catalysis* **2017,** *7* (4), 2471-2485.

17. Shafaat, H. S.; Rüdiger, O.; Ogata, H.; Lubitz, W., [NiFe] hydrogenases: A common active site for hydrogen metabolism under diverse conditions. *Biochimica et Biophysica Acta (BBA) - Bioenergetics* **2013,** *1827* (8), 986-1002.

18. Vincent, K. A.; Parkin, A.; Armstrong, F. A., Investigating and exploiting the electrocatalytic properties of hydrogenases. *Chemical Reviews* **2007,** *107* (10), 4366-4413.

19. Ahmed, M. E.; Dey, A., Recent developments in bioinspired modelling of [NiFe]- and [FeFe]-hydrogenases. *Current Opinion in Electrochemistry* **2019,** *15*, 155-164.

20. Moura, I.; Pauleta, S. R.; Moura, J. J. G., Enzymatic activity mastered by altering metal coordination spheres. *JBIC Journal of Biological Inorganic Chemistry* **2008,** *13* (8), 1185-1195.

21. Tai, H. L.; Hirota, S., Mechanism and Application of the Catalytic Reaction of NiFe Hydrogenase: Recent Developments. *Chembiochem* **2020,** *21* (11), 1573-1581.

22. Ogata, H.; Hirota, S.; Nakahara, A.; Komori, H.; Shibata, N.; Kato, T.; Kano, K.; Higuchi, Y., Activation Process of [NiFe] Hydrogenase Elucidated by High-Resolution X-Ray Analyses: Conversion of the Ready to the Unready State. *Structure* **2005,** *13* (11), 1635-1642.

23. Dementin, S.; Burlat, B.; De Lacey, A. L.; Pardo, A.; Adryanczyk-Perrier, G.; Guigliarelli, B.; Fernandez, V. M.; Rousset, M., A Glutamate Is the Essential Proton Transfer Gate during the Catalytic Cycle of the [NiFe] Hydrogenase*. *Journal of Biological Chemistry* **2004,** *279* (11), 10508-10513.

24. Volbeda, A.; Charon, M. H.; Piras, C.; Hatchikian, E. C.; Frey, M.; Fontecillacamps, J. C., CRYSTAL-STRUCTURE OF THE NICKEL-IRON HYDROGENASE FROM DESULFOVIBRIO-GIGAS. *Nature* **1995,** *373* (6515), 580-587.

25. Volbeda, A.; Garcin, E.; Piras, C.; de Lacey, A. L.; Fernandez, V. M.; Hatchikian, E. C.; Frey, M.; Fontecilla-Camps, J. C., Structure of the [NiFe] Hydrogenase Active Site: Evidence for Biologically Uncommon Fe Ligands. *Journal of the American Chemical Society* **1996,** *118* (51), 12989-12996.

26. Pierik, A. J.; Hulstein, M.; Hagen, W. R.; Albracht, S. P. J., A low-spin iron with CN and CO as intrinsic ligands forms the core of the active site in Fe - hydrogenases. *European Journal of Biochemistry* **1998,** *258* (2), 572-578.

27. Happe, R. P.; Roseboom, W.; Pierik, A. J.; Albracht, S. P. J.; Bagley, K. A., Biological activition of hydrogen. *Nature* **1997,** *385* (6612), 126-126.

28. de Lacey, A. L.; Hatchikian, E. C.; Volbeda, A.; Frey, M.; Fontecilla-Camps, J. C.; Fernandez, V. M., Infrared-Spectroelectrochemical Characterization of the [NiFe] Hydrogenase of Desulfovibrio gigas. *Journal of the American Chemical Society* **1997,** *119* (31), 7181-7189.

29. Armstrong, F. A., Hydrogenases: active site puzzles and progress. *Current Opinion in Chemical Biology* **2004,** *8* (2), 133-140.

30. Stein, M.; Lubitz, W., Quantum chemical calculations of [NiFe] hydrogenase. *Current Opinion in Chemical Biology* **2002,** *6* (2), 243-249.

31. Higuchi, Y.; Ogata, H.; Miki, K.; Yasuoka, N.; Yagi, T., Removal of the bridging ligand atom at the Ni–Fe active site of [NiFe] hydrogenase upon reduction with H2, as revealed by X-ray structure analysis at 1.4 Å resolution. *Structure* **1999,** *7* (5), 549-556.

32. Lubitz, W.; Reijerse, E.; van Gastel, M., [NiFe] and [FeFe] Hydrogenases Studied by Advanced Magnetic Resonance Techniques. *Chemical Reviews* **2007,** *107* (10), 4331-4365.

33. Albracht, S. P. J.; Kalkman, M. L.; Slater, E. C., Magnetic interaction of nickel(III) and the iron-sulphur cluster in hydrogenase from Chromatium vinosum. *Biochimica et Biophysica Acta (BBA) - Bioenergetics* **1983,** *724* (3), 309-316.

34. van der Zwaan, J. W.; Coremans, J. M. C. C.; Bouwens, E. C. M.; Albracht, S. P. J., Effect of 17O2 and 13CO on EPR espectra of nickel in hydrogenase from Chromatium vinosum. *Biochimica et Biophysica Acta (BBA) - Protein Structure and Molecular Enzymology* **1990,** *1041* (2), 101-110.

35. Sigfridsson, K. G. V.; Leidel, N.; Sanganas, O.; Chernev, P.; Lenz, O.; Yoon, K.-S.; Nishihara, H.; Parkin, A.; Armstrong, F. A.; Dementin, S.; Rousset, M.; De Lacey, A. L.; Haumann, M., Structural differences of oxidized iron–sulfur and nickel–iron cofactors in O2-tolerant and O2-sensitive hydrogenases studied by X-ray absorption spectroscopy. *Biochimica et Biophysica Acta (BBA) - Bioenergetics* **2015,** *1847* (2), 162-170.

36. Carepo, M.; Tierney, D. L.; Brondino, C. D.; Yang, T. C.; Pamplona, A.; Telser, J.; Moura, I.; Moura, J. J. G.; Hoffman, B. M., 17O ENDOR detection of a solvent-derived Ni-(OHx)-Fe bridge that is lost upon activation of the hydrogenase from Desulfovibrio gigas. *Journal of the American Chemical Society* **2002,** *124* (2), 281-286.

37. Trofanchuk, O.; Stein, M.; Geßner, C.; Lendzian, F.; Higuchi, Y.; Lubitz, W., Single crystal EPR studies of the oxidized active site of [NiFe] hydrogenase from Desulfovibrio vulgaris Miyazaki F. *JBIC Journal of Biological Inorganic Chemistry* **2000,** *5* (1), 36-44.

38. Ogata, H.; Lubitz, W.; Higuchi, Y., [NiFe] hydrogenases: structural and spectroscopic studies of the reaction mechanism. *Dalton Transactions* **2009,** (37), 7577-7587.

39. Pandelia, M. E.; Ogata, H.; Lubitz, W., Intermediates in the Catalytic Cycle of NiFe Hydrogenase: Functional Spectroscopy of the Active Site. *Chemphyschem* **2010,** *11* (6), 1127-1140.

40. Ogata, H.; Nishikawa, K.; Lubitz, W., Hydrogens detected by subatomic resolution protein crystallography in a NiFe hydrogenase. *Nature* **2015,** *520* (7548), 571-574.

41. Brecht, M.; van Gastel, M.; Buhrke, T.; Friedrich, B.; Lubitz, W., Direct Detection of a Hydrogen Ligand in the [NiFe] Center of the Regulatory H2-Sensing Hydrogenase from Ralstonia eutropha in Its Reduced State by HYSCORE and ENDOR Spectroscopy. *Journal of the American Chemical Society* **2003,** *125* (43), 13075-13083.

42. Whitehead, J. P.; Gurbiel, R. J.; Bagyinka, C.; Hoffman, B. M.; Maroney, M. J., The hydrogen binding site in hydrogenase: 35-GHz ENDOR and XAS studies of the nickel-C (reduced and active form) and the Ni-L photoproduct. *Journal of the American Chemical Society* **1993,** *115* (13), 5629-5635.

43. Stein, M.; Lubitz, W., The electronic structure of the catalytic intermediate Ni-C in [NiFe] and [NiFeSe] hydrogenases. *Physical Chemistry Chemical Physics* **2001,** *3* (23), 5115-5120.

44. Kramer, T.; Kamp, M.; Lubitz, W.; van Gastel, M.; Neese, F., Theoretical Spectroscopy of the Ni-II Intermediate States in the Catalytic Cycle and the Activation of NiFe Hydrogenases. *Chembiochem* **2013,** *14* (14), 1898-1905.

45. Foerster, S.; Stein, M.; Brecht, M.; Ogata, H.; Higuchi, Y.; Lubitz, W., Single Crystal EPR Studies of the Reduced Active Site of [NiFe] Hydrogenase from Desulfovibrio vulgaris Miyazaki F. *Journal of the American Chemical Society* **2003,** *125* (1), 83-93.

46. Fichtner, C.; van Gastel, M.; Lubitz, W., Wavelength dependence of the photo-induced conversion of the Ni–C to the Ni–L redox state in the [NiFe] hydrogenase of Desulfovibrio vulgaris Miyazaki F. *Physical Chemistry Chemical Physics* **2003,** *5* (24), 5507-5513.

47. Medina, M.; Claude Hatchikian, E.; Cammack, R., Studies of light-induced nickel EPR signals in hydrogenase: comparison of enzymes with and without selenium. *Biochimica et Biophysica Acta (BBA) - Bioenergetics* **1996,** *1275* (3), 227-236.

48. Dong, G.; Phung, Q. M.; Pierloot, K.; Ryde, U., Reaction Mechanism of NiFe Hydrogenase Studied by Computational Methods. *Inorganic Chemistry* **2018,** *57* (24), 15289-15298.

49. Dong, G.; Phung, Q. M.; Hallaert, S. D.; Pierloot, K.; Ryde, U., H2 binding to the active site of [NiFe] hydrogenase studied by multiconfigurational and coupled-cluster methods. *Physical Chemistry Chemical Physics* **2017,** *19* (16), 10590-10601.

50. Dong, G.; Ryde, U.; Aa. Jensen, H. J.; Hedegård, E. D., Exploration of H2 binding to the [NiFe]-hydrogenase active site with multiconfigurational density functional theory. *Physical Chemistry Chemical Physics* **2018,** *20* (2), 794-801.

51. Qiu, S. Y.; Azofra, L. M.; MacFarlane, D. R.; Sun, C. H., Unraveling the Role of Ligands in the Hydrogen Evolution Mechanism Catalyzed by NiFe Hydrogenases. *Acs Catalysis* **2016,** *6* (8), 5541-5548.

52. Dole, F.; Fournel, A.; Magro, V.; Hatchikian, E. C.; Bertrand, P.; Guigliarelli, B., Nature and Electronic Structure of the Ni-X Dinuclear Center of Desulfovibrio gigas Hydrogenase. Implications for the Enzymatic Mechanism. *Biochemistry* **1997,** *36* (25), 7847-7854.

53. Huyett, J. E.; Carepo, M.; Pamplona, A.; Franco, R.; Moura, I.; Moura, J. J. G.; Hoffman, B. M., 57Fe Q-Band Pulsed ENDOR of the Hetero-Dinuclear Site of Nickel Hydrogenase: Comparison of the NiA, NiB, and NiC States. *Journal of the American Chemical Society* **1997,** *119* (39), 9291-9292.

54. Liebgott, P. P.; Leroux, F.; Burlat, B.; Dementin, S.; Baffert, C.; Lautier, T.; Fourmond, V.; Ceccaldi, P.; Cavazza, C.; Meynial-Salles, I.; Soucaille, P.; Fontecilla-Camps, J. C.; Guigliarelli, B.; Bertrand, P.; Rousset, M.; Leger, C., Relating diffusion along the substrate tunnel and oxygen sensitivity in hydrogenase. *Nature Chemical Biology* **2010,** *6* (1), 63-70.

55. Jensen, F., *Introduction to computational chemistry*. 2017.

56. Kampa, M.; Pandelia, M.-E.; Lubitz, W.; van Gastel, M.; Neese, F., A Metal–Metal Bond in the Light-Induced State of [NiFe] Hydrogenases with Relevance to Hydrogen Evolution. *Journal of the American Chemical Society* **2013,** *135* (10), 3915-3925.

57. Bennie, S. J.; van der Kamp, M. W.; Pennifold, R. C. R.; Stella, M.; Manby, F. R.; Mulholland, A. J., A Projector-Embedding Approach for Multiscale Coupled-Cluster Calculations Applied to Citrate Synthase. *Journal of Chemical Theory and Computation* **2016,** *12* (6), 2689-2697.

58. Sundararajan, M.; Hillier, I. H., Comprehensive Inorganic Chemistry II: From Elements to Applications. Elsevier: 2013; Vol. 9.

59. Vogiatzis, K. D.; Polynski, M. V.; Kirkland, J. K.; Townsend, J.; Hashemi, A.; Liu, C.; Pidko, E. A., Computational Approach to Molecular Catalysis by 3d Transition Metals: Challenges and Opportunities. *Chemical Reviews* **2019,** *119* (4), 2453-2523.

60. Qiu, S. Y.; Azofra, L. M.; MacFarlane, D. R.; Sun, C. H., Why is a proton transformed into a hydride by NiFe hydrogenases? An intrinsic reactivity analysis based on conceptual DFT. *Physical Chemistry Chemical Physics* **2016,** *18* (22), 15369-15374.

61. Qiu, S. Y.; Azofra, L. M.; MacFarlane, D. R.; Sun, C. H., Hydrogen bonding effect between active site and protein environment on catalysis performance in H-2-producing NiFe hydrogenases. *Physical Chemistry Chemical Physics* **2018,** *20* (9), 6735-6743.

62. Kaliakin, D. S.; Zaari, R. R.; Varganov, S. A., Effect of H2 Binding on the Nonadiabatic Transition Probability between Singlet and Triplet States of the [NiFe]-Hydrogenase Active Site. *The Journal of Physical Chemistry A* **2015,** *119* (6), 1066-1073.

63. Frisch, M. J.; Trucks, G. W.; Schlegel, H. B.; Scuseria, G. E.; Robb, M. A.; Cheeseman, J. R.; Scalmani, G.; Barone, V.; Mennucci, B.; Petersson, G. A.; Nakatsuji, H.; Caricato, M.; Li, X.; Hratchian, H. P.; Izmaylov, A. F.; Bloino, J.; Zheng, G.; Sonnenberg, J. L.; Hada, M.; Ehara, M.; Toyota, K.; Fukuda, R.; Hasegawa, J.; Ishida, M.; Nakajima, T.; Honda, Y.; Kitao, O.; Nakai, H.; Vreven,

T.; Montgomery, J. A., Jr.; Peralta, J. E.; Ogliaro, F.; Bearpark, M.; Heyd, J. J.; Brothers, E.; Kudin, K. N.; Staroverov, V. N.; Kobayashi, R.; Normand, J.; Raghavachari, K.; Rendell, A.; Burant, J. C.; Iyengar, S. S.; Tomasi, J.; Cossi, M.; Rega, N.; Millam, J. M.; Klene, M.; Knox, J. E.; Cross, J. B.; Bakken, V.; Adamo, C.; Jaramillo, J.; Gomperts, R.; Stratmann, R. E.; Yazyev, O.; Austin, A. J.; Cammi, R.; Pomelli, C.; Ochterski, J. W.; Martin, R. L.; Morokuma, K.; Zakrzewski, V. G.; Voth, G. A.; Salvador, P.; Dannenberg, J. J.; Dapprich, S.; Daniels, A. D.; Farkas, Ö.; Foresman, J. B.; Ortiz, J. V.; Cioslowski, J.; Fox, D. J. *Gaussian 09, Revision E.01*, Gaussian, Inc.: Wallingford CT, 2009.

64. Becke, A. D., DENSITY-FUNCTIONAL EXCHANGE-ENERGY APPROXIMATION WITH CORRECT ASYMPTOTIC-BEHAVIOR. *Physical Review A* **1988,** *38* (6), 3098-3100.

65. Weigend, F.; Ahlrichs, R., Balanced basis sets of split valence, triple zeta valence and quadruple zeta valence quality for H to Rn: Design and assessment of accuracy. *Physical Chemistry Chemical Physics* **2005,** *7* (18), 3297-3305.

66. Weigend, F., Accurate Coulomb-fitting basis sets for H to Rn. *Physical Chemistry Chemical Physics* **2006,** *8* (9), 1057-1065.

67. Foresman, J. B.; Keith, T. A.; Wiberg, K. B.; Snoonian, J.; Frisch, M. J., Solvent effects .5. Influence of cavity shape, truncation of electrostatics, and electron correlation ab initio reaction field calculations. *Journal of Physical Chemistry* **1996,** *100* (40), 16098-16104.

68. Volbeda, A.; Martin, L.; Liebgott, P.-P.; De Lacey, A. L.; Fontecilla-Camps, J. C., [NiFe]-hydrogenases revisited: nickel–carboxamido bond formation in a variant with accrued O2-tolerance and a tentative re-interpretation of Ni-SI states†. *Metallomics* **2015,** *7* (4), 710-718.

69. Evans, R. M.; Brooke, E. J.; Wehlin, S. A. M.; Nomerotskaia, E.; Sargent, F.; Carr, S. B.; Phillips, S. E. V.; Armstrong, F. A., Mechanism of hydrogen activation by NiFe hydrogenases. *Nature Chemical Biology* **2016,** *12* (1), 46-50.

70. McNaught, A. D.; Wilkinson, A., *IUPAC. Compendium of Chemical Terminology*. 2nd ed. (the "Gold Book") ed.; Blackwell Scientific Publications: Oxford, 1997.

71. Trasatti, S., THE ABSOLUTE ELECTRODE POTENTIAL - AN EXPLANATORY NOTE (RECOMMENDATIONS 1986). *Pure and Applied Chemistry* **1986,** *58* (7), 955-966.

72. Yang, L.; Powell, D. R.; Houser, R. P., Structural variation in copper(I) complexes with pyridylmethylamide ligands: structural analysis with a new four-coordinate geometry index, tau(4). *Dalton Transactions* **2007,** (9), 955-964.

73. Addison, A. W.; Rao, T. N.; Reedijk, J.; Vanrijn, J.; Verschoor, G. C., SYNTHESIS, STRUCTURE, AND SPECTROSCOPIC PROPERTIES OF COPPER(II) COMPOUNDS CONTAINING NITROGEN SULFUR DONOR LIGANDS - THE CRYSTAL AND MOLECULAR-STRUCTURE OF AQUA 1,7-BIS(N-METHYLBENZIMIDAZOL-2'-YL)-2,6-DITHIAHEPTANE COPPER(II) PERCHLORATE. *Journal of the Chemical Society-Dalton Transactions* **1984,** (7), 1349-1356.

74. Volbeda, A.; Amara, P.; Darnault, C.; Mouesca, J. M.; Parkin, A.; Roessler, M. M.; Armstrong, F. A.; Fontecilla-Camps, J. C., X-ray crystallographic and computational studies of the O-2-tolerant NiFe -hydrogenase 1 from Escherichia coli. *Proceedings of the National Academy of Sciences of the United States of America* **2012,** *109* (14), 5305-5310.

75. Stephan, D. W.; Erker, G., Frustrated Lewis Pairs: Metal-free Hydrogen Activation and More. *Angewandte Chemie-International Edition* **2010,** *49* (1), 46-76.

76. Szőri-Dorogházi, E.; Maróti, G.; Szőri, M.; Nyilasi, A.; Rákhely, G.; Kovács, K. L., Analyses of the Large Subunit Histidine-Rich Motif Expose an Alternative Proton Transfer Pathway in [NiFe] Hydrogenases. *PLOS ONE* **2012,** *7* (4), e34666.

77. Berggren, G.; Adamska, A.; Lambertz, C.; Simmons, T. R.; Esselborn, J.; Atta, M.; Gambarelli, S.; Mouesca, J. M.; Reijerse, E.; Lubitz, W.; Happe, T.; Artero, V.; Fontecave, M., Biomimetic assembly and activation of [FeFe]-hydrogenases. *Nature* **2013,** *499* (7456), 66-69.

78. Dutta, A.; DuBois, D. L.; Roberts, J. A. S.; Shaw, W. J., Amino acid modified Ni catalyst exhibits reversible H₂ oxidation/production over a broad pH range at elevated temperatures. *Proceedings of the National Academy of Sciences* **2014,** *111* (46), 16286.

79. Priyadarshani, N.; Dutta, A.; Ginovska, B.; Buchko, G. W.; O'Hagan, M.; Raugei, S.; Shaw, W. J., Achieving Reversible H2/H+ Interconversion at Room Temperature with Enzyme-Inspired Molecular Complexes: A Mechanistic Study. *ACS Catalysis* **2016,** *6* (9), 6037-6049.

80. Humphrey, W.; Dalke, A.; Schulten, K., VMD: Visual molecular dynamics. *Journal of Molecular Graphics & Modelling* **1996,** *14* (1), 33-38.

81. Schilter, D.; Camara, J. M.; Huynh, M. T.; Hammes-Schiffer, S.; Rauchfuss, T. B., Hydrogenase Enzymes and Their Synthetic Models: The Role of Metal Hydrides. *Chemical Reviews* **2016,** *116* (15), 8693-8749.

82. Sealy, C., The problem with platinum. *Materials Today* **2008,** *11* (12), 65-68.

83. Peters, J. W.; Schut, G. J.; Boyd, E. S.; Mulder, D. W.; Shepard, E. M.; Broderick, J. B.; King, P. W.; Adams, M. W. W., [FeFe]- and [NiFe]-hydrogenase diversity, mechanism, and maturation. *Biochimica et Biophysica Acta (BBA) - Molecular Cell Research* **2015,** *1853* (6), 1350-1369.

84. Gloaguen, F.; Rauchfuss, T. B., Small molecule mimics of hydrogenases: hydrides and redox. *Chemical Society Reviews* **2009,** *38* (1), 100-108.

85. Heinekey, D. M., Hydrogenase enzymes: Recent structural studies and active site models. *Journal of Organometallic Chemistry* **2009,** *694* (17), 2671-2680.

86. Tard, C.; Pickett, C. J., Structural and Functional Analogues of the Active Sites of the [Fe]-, [NiFe]-, and [FeFe]-Hydrogenases. *Chemical Reviews* **2009,** *109* (6), 2245-2274.

87. Darensbourg, M. Y., HYDROGENASE ACTIVE SITES: A NEW PARADIGM FOR NATURAL PRODUCT-INSPIRED SYNTHESIS BASED ON ORGANOMETALLIC CHEMISTRY. *Comments on Inorganic Chemistry* **2010,** *31* (3-4), 144-152.

88. Yang, J. Y.; Bullock, R. M.; DuBois, M. R.; DuBois, D. L., Fast and efficient molecular electrocatalysts for H₂ production: Using hydrogenase enzymes as guides. *MRS Bulletin* **2011,** *36*, 39-47.

89. DuBois, D. L., Development of Molecular Electrocatalysts for Energy Storage. *Inorganic Chemistry* **2014,** *53* (8), 3935-3960.

90. Simmons, T. R.; Berggren, G.; Bacchi, M.; Fontecave, M.; Artero, V., Mimicking hydrogenases: From biomimetics to artificial enzymes. *Coordination Chemistry Reviews* **2014,** *270-271*, 127-150.

91. Artero, V.; Berggren, G.; Atta, M.; Caserta, G.; Roy, S.; Pecqueur, L.; Fontecave, M., From Enzyme Maturation to Synthetic Chemistry: The Case of Hydrogenases. *Accounts of Chemical Research* **2015,** *48* (8), 2380-2387.

92. Xu, T.; Chen, D.; Hu, X., Hydrogen-activating models of hydrogenases. *Coordination Chemistry Reviews* **2015,** *303*, 32-41.

93. So, K.; Kitazumi, Y.; Shirai, O.; Nishikawa, K.; Higuchi, Y.; Kano, K., Direct electron transfer-type dual gas diffusion H2/O2 biofuel cells. *Journal of Materials Chemistry A* **2016,** *4* (22), 8742-8749.

94. Szczesny, J.; Marković, N.; Conzuelo, F.; Zacarias, S.; Pereira, I. A. C.; Lubitz, W.; Plumeré, N.; Schuhmann, W.; Ruff, A., A gas breathing hydrogen/air biofuel cell comprising a redox polymer/hydrogenase-based bioanode. *Nature communications* **2018,** *9* (1), 4715-4715.

95. Cracknell, J. A.; Vincent, K. A.; Armstrong, F. A., Enzymes as Working or Inspirational Electrocatalysts for Fuel Cells and Electrolysis. *Chemical Reviews* **2008,** *108* (7), 2439-2461.

96. Brazzolotto, D.; Gennari, M.; Queyriaux, N.; Simmons, T. R.; Pecaut, J.; Demeshko, S.; Meyer, F.; Orio, M.; Artero, V.; Duboc, C., Nickel-centred proton reduction catalysis in a model of NiFe hydrogenase. *Nature Chemistry* **2016,** *8* (11), 1054-1060.

97. Ghosh, P.; Quiroz, M.; Wang, N.; Bhuvanesh, N.; Darensbourg, M. Y., Complexes of MN2S2 center dot Fe(eta(5)-C5R5)(CO) as platform for exploring cooperative heterobimetallic effects in HER electrocatalysis. *Dalton Transactions* **2017,** *46* (17), 5617-5624.

98. Chu, X. X.; Yu, X.; Raje, S.; Angamuthu, R.; Ma, J. P.; Tung, C. H.; Wang, W. G., Synthetic NiFe models with a fluxional CO ligand. *Dalton Transactions* **2017,** *46* (40), 13681-13685.

99. Chu, X. X.; Jin, J. H.; Ming, B. R.; Pang, M. F.; Yu, X.; Tung, C. H.; Wang, W. G., Bimetallic nickel-cobalt hydrides in H-2 activation and catalytic proton reduction. *Chemical Science* **2019,** *10* (3), 761-767.

100. Barton, B. E.; Rauchfuss, T. B., Hydride-Containing Models for the Active Site of the Nickel-Iron Hydrogenases. *Journal of the American Chemical Society* **2010,** *132* (42), 14877-14885.

101. Ulloa, O. A.; Huynh, M. T.; Richers, C. P.; Bertke, J. A.; Nilges, M. J.; Hammes-Schiffer, S.; Rauchfuss, T. B., Mechanism of H-2 Production by Models for the NiFe -Hydrogenases: Role of Reduced Hydrides. *Journal of the American Chemical Society* **2016,** *138* (29), 9234-9245.

102. Manor, B. C.; Rauchfuss, T. B., Hydrogen Activation by Biomimetic NiFe -Hydrogenase Model Containing Protected Cyanide Cofactors. *Journal of the American Chemical Society* **2013,** *135* (32), 11895-11900.

103. Ohki, Y.; Tatsumi, K., Thiolate-Bridged Iron–Nickel Models for the Active Site of [NiFe] Hydrogenase. *European Journal of Inorganic Chemistry* **2011,** *2011* (7), 973-985.

104. Simmons, T. R.; Artero, V., Catalytic Hydrogen Oxidation: Dawn of a New Iron Age. *Angewandte Chemie International Edition* **2013,** *52* (24), 6143-6145.

105. Canaguier, S.; Artero, V.; Fontecave, M., Modelling NiFe hydrogenases: nickel-based electrocatalysts for hydrogen production. *Dalton Transactions* **2008,** (3), 315-325.

106. Ogo, S., Electrons from hydrogen. *Chemical Communications* **2009,** (23), 3317-3325.

107. Frisch, M. J.; Trucks, G. W.; Schlegel, H. B.; Scuseria, G. E.; Robb, M. A.; Cheeseman, J. R.; Scalmani, G.; Barone, V.; Petersson, G. A.; Nakatsuji, H.; Li, X.; Caricato, M.; Marenich, A. V.; Bloino, J.; Janesko, B. G.; Gomperts, R.; Mennucci, B.; Hratchian, H. P.; Ortiz, J. V.; Izmaylov, A. F.; Sonnenberg, J. L.; Williams; Ding, F.; Lipparini, F.; Egidi, F.; Goings, J.; Peng, B.; Petrone, A.; Henderson, T.; Ranasinghe, D.; Zakrzewski, V. G.; Gao, J.; Rega, N.; Zheng, G.; Liang, W.; Hada, M.; Ehara, M.; Toyota, K.; Fukuda, R.; Hasegawa, J.; Ishida, M.; Nakajima, T.; Honda, Y.; Kitao, O.; Nakai, H.; Vreven, T.; Throssell, K.; Montgomery Jr., J. A.; Peralta, J. E.; Ogliaro, F.; Bearpark, M. J.; Heyd, J. J.; Brothers, E. N.; Kudin, K. N.; Staroverov, V. N.; Keith, T. A.; Kobayashi, R.; Normand, J.; Raghavachari, K.; Rendell, A. P.; Burant, J. C.; Iyengar, S. S.; Tomasi, J.; Cossi, M.; Millam, J. M.; Klene, M.; Adamo, C.; Cammi, R.; Ochterski, J. W.; Martin, R. L.; Morokuma, K.; Farkas, O.; Foresman, J. B.; Fox, D. J. *Gaussian 16 Rev. C.01*, Wallingford, CT, 2016.

108. Neumann, C. S.; Fujimori, D. G.; Walsh, C. T., Halogenation Strategies In Natural Product Biosynthesis. *Chemistry & Biology* **2008,** *15* (2), 99-109.

109. Mehmood, R.; Qi, H. W.; Steeves, A. H.; Kulik, H. J., The Protein's Role in Substrate Positioning and Reactivity for Biosynthetic Enzyme Complexes: The Case of SyrB2/SyrB1. *ACS Catalysis* **2019,** *9* (6), 4930-4943.

110. Lowe, J. R.; Martello, M. T.; Tolman, W. B.; Hillmyer, M. A., Functional biorenewable polyesters from carvone-derived lactones. *Polymer Chemistry* **2011,** *2* (3), 702-708.

111. Tong, W.; Huang, Q.; Li, M.; Wang, J.-b., Enzyme-catalyzed C–F bond formation and cleavage. *Bioresources and Bioprocessing* **2019,** *6* (1), 46.

112. Gribble, G. W., Natural Organohalogens: A New Frontier for Medicinal Agents? *Journal of Chemical Education* **2004,** *81* (10), 1441.

113. Vaillancourt, F. H.; Yeh, E.; Vosburg, D. A.; Garneau-Tsodikova, S.; Walsh, C. T., Nature's Inventory of Halogenation Catalysts: Oxidative Strategies Predominate. *Chemical Reviews* **2006,** *106* (8), 3364-3378.

114. Wilcken, R.; Zimmermann, M. O.; Lange, A.; Joerger, A. C.; Boeckler, F. M., Principles and Applications of Halogen Bonding in Medicinal Chemistry and Chemical Biology. *Journal of Medicinal Chemistry* **2013,** *56* (4), 1363-1388.

115. Fujimori, D. G.; Walsh, C. T., What's new in enzymatic halogenations. *Current opinion in chemical biology* **2007,** *11* (5), 553-560.

116. Walsh, C. T., The Chemical Versatility of Natural-Product Assembly Lines. *Accounts of Chemical Research* **2008,** *41* (1), 4-10.

117. Menon, B. R. K.; Richmond, D.; Menon, N., Halogenases for biosynthetic pathway engineering: Toward new routes to naturals and non-naturals. *Catalysis Reviews* **2020**, 1-59.

118. Borowski, T.; Noack, H.; Radoń, M.; Zych, K.; Siegbahn, P. E. M., Mechanism of Selective Halogenation by SyrB2: A Computational Study. *Journal of the American Chemical Society* **2010,** *132* (37), 12887-12898.

119. Zhang, X.; Wang, Z.; Gao, J.; Liu, W., Chlorination versus hydroxylation selectivity mediated by the non-heme iron halogenase WelO5. *Physical Chemistry Chemical Physics* **2020,** *22* (16), 8699-8712.

120. Zhang, L. Y.; Morello, G.; Carr, S. B.; Armstrong, F. A., Aerobic Photocatalytic H-2 Production by a NiFe Hydrogenase Engineered to Place a Silver Nanocluster in the Electron Relay. *Journal of the American Chemical Society* **2020,** *142* (29), 12699-12707.

121. Tsutsuura, M.; Moriyama, H.; Kojima, N.; Mizukami, Y.; Tashiro, S.; Osa, S.; Enoki, Y.; Taguchi, K.; Oda, K.; Fujii, S.; Takahashi, Y.; Hamada, Y.; Kimura, T.; Takesue, Y.; Matsumoto, K., The monitoring of vancomycin: a systematic review and meta-analyses of area under the concentration-time curve-guided dosing and trough-guided dosing. *BMC Infectious Diseases* **2021,** *21* (1), 153.

122. Harris, C. M.; Kannan, R.; Kopecka, H.; Harris, T. M., The role of the chlorine substituents in the antibiotic vancomycin: preparation and characterization of mono- and didechlorovancomycin. *Journal of the American Chemical Society* **1985,** *107* (23), 6652-6658.

123. Piraee, M.; White, R. L.; Vining, L. C., Biosynthesis of the dichloroacetyl component of chloramphenicol in Streptomyces venezuelae ISP5230: genes required for halogenation. *Microbiology* **2004,** *150* (1), 85-94.

124. Solomon, E. I.; Brunold, T. C.; Davis, M. I.; Kemsley, J. N.; Lee, S.-K.; Lehnert, N.; Neese, F.; Skulan, A. J.; Yang, Y.-S.; Zhou, J., Geometric and Electronic Structure/Function Correlations in Non-Heme Iron Enzymes. *Chemical Reviews* **2000,** *100* (1), 235-350.

125. Costas, M.; Mehn, M. P.; Jensen, M. P.; Que, L., Dioxygen Activation at Mononuclear Nonheme Iron Active Sites: Enzymes, Models, and Intermediates. *Chemical Reviews* **2004,** *104* (2), 939-986.

126. Hausinger, R. P., Fe(II)/α-Ketoglutarate-Dependent Hydroxylases and Related Enzymes. *Critical Reviews in Biochemistry and Molecular Biology* **2004,** *39* (1), 21-68.

127. Krebs, C.; Galonić Fujimori, D.; Walsh, C. T.; Bollinger, J. M., Non-Heme Fe(IV)–Oxo Intermediates. *Accounts of Chemical Research* **2007,** *40* (7), 484-492.

128. Solomon, E. I.; Goudarzi, S.; Sutherlin, K. D., O2 Activation by Non-Heme Iron Enzymes. *Biochemistry* **2016,** *55* (46), 6363-6374.

129. Timmins, A.; De Visser, S. P., A Comparative Review on the Catalytic Mechanism of Nonheme Iron Hydroxylases and Halogenases. *Catalysts* **2018,** *8* (8), 314.

130. Solomon, E. I.; Decker, A.; Lehnert, N., Non-heme iron enzymes: Contrasts to heme catalysis. *Proceedings of the National Academy of Sciences* **2003,** *100* (7), 3589-3594.

131. de Visser, S. P., Propene Activation by the Oxo-Iron Active Species of Taurine/α-Ketoglutarate Dioxygenase (TauD) Enzyme. How Does the Catalysis Compare to Heme-Enzymes? *Journal of the American Chemical Society* **2006,** *128* (30), 9813-9824.

132. de Visser, S. P., What Factors Influence the Ratio of CH Hydroxylation versus CC Epoxidation by a Nonheme Cytochrome P450 Biomimetic? *Journal of the American Chemical Society* **2006,** *128* (49), 15809-15818.

133. Que, L., The Road to Non-Heme Oxoferryls and Beyond. *Accounts of Chemical Research* **2007,** *40* (7), 493-500.

134. Nam, W., High-Valent Iron(IV)–Oxo Complexes of Heme and Non-Heme Ligands in Oxygenation Reactions. *Accounts of Chemical Research* **2007,** *40* (7), 522-531.

135. Loenarz, C.; Schofield, C. J., Expanding chemical biology of 2-oxoglutarate oxygenases. *Nature Chemical Biology* **2008,** *4* (3), 152-156.

136. de Visser, S. P., Trends in Substrate Hydroxylation Reactions by Heme and Nonheme Iron(IV)-Oxo Oxidants Give Correlations between Intrinsic Properties of the Oxidant with Barrier Height. *Journal of the American Chemical Society* **2010,** *132* (3), 1087-1097.

137. Dong, G.; Lu, J.; Lai, W., Insights into the Mechanism of Aromatic Ring Cleavage of Noncatecholic Compound 2-Aminophenol by Aminophenol Dioxygenase: A Quantum Mechanics/Molecular Mechanics Study. *ACS Catalysis* **2016,** *6* (6), 3796-3803.

138. Agarwal, V.; Miles, Z. D.; Winter, J. M.; Eustáquio, A. S.; El Gamal, A. A.; Moore, B. S., Enzymatic Halogenation and Dehalogenation Reactions: Pervasive and Mechanistically Diverse. *Chemical Reviews* **2017,** *117* (8), 5619-5674.

139. de Visser, S. P., Mechanistic Insight on the Activity and Substrate Selectivity of Nonheme Iron Dioxygenases. *The Chemical Record* **2018,** *18* (10), 1501-1516.

140. Vaillancourt, F. H.; Yin, J.; Walsh, C. T., SyrB2 in syringomycin E biosynthesis is a nonheme Fe^{II} α-ketoglutarate- and O₂-dependent halogenase. *Proceedings of the National Academy of Sciences of the United States of America* **2005,** *102* (29), 10111-10116.

141. Blasiak, L. C.; Vaillancourt, F. H.; Walsh, C. T.; Drennan, C. L., Crystal structure of the non-haem iron halogenase SyrB2 in syringomycin biosynthesis. *Nature* **2006,** *440* (7082), 368-371.

142. Galonić, D. P.; Barr, E. W.; Walsh, C. T.; Bollinger, J. M.; Krebs, C., Two interconverting Fe(IV) intermediates in aliphatic chlorination by the halogenase CytC3. *Nature Chemical Biology* **2007,** *3* (2), 113-116.

143. Wong, C.; Fujimori, D. G.; Walsh, C. T.; Drennan, C. L., Structural Analysis of an Open Active Site Conformation of Nonheme Iron Halogenase CytC3. *Journal of the American Chemical Society* **2009,** *131* (13), 4872-4879.

144. Vaillancourt, F. H.; Yeh, E.; Vosburg, D. A.; O'Connor, S. E.; Walsh, C. T., Cryptic chlorination by a non-haem iron enzyme during cyclopropyl amino acid biosynthesis. *Nature* **2005,** *436* (7054), 1191-1194.

145. Mitchell, A. J.; Zhu, Q.; Maggiolo, A. O.; Ananth, N. R.; Hillwig, M. L.; Liu, X.; Boal, A. K., Structural basis for halogenation by iron- and 2-oxo-glutarate-dependent enzyme WelO5. *Nature Chemical Biology* **2016,** *12* (8), 636-640.

146. Khare, D.; Wang, B.; Gu, L.; Razelun, J.; Sherman, D. H.; Gerwick, W. H.; Håkansson, K.; Smith, J. L., Conformational switch triggered by α-ketoglutarate in a halogenase of curacin A biosynthesis. *Proceedings of the National Academy of Sciences* **2010,** *107* (32), 14099-14104.

147. Pratter, S. M.; Light, K. M.; Solomon, E. I.; Straganz, G. D., The Role of Chloride in the Mechanism of O2 Activation at the Mononuclear Nonheme Fe(II) Center of the Halogenase HctB. *Journal of the American Chemical Society* **2014,** *136* (26), 9385-9395.

148. Wilson, R. H.; Bhagi-Damodaran, A., University of Minnesota: Minneapolis, MN, Unpublished Work, 2021.

149. Kalliri, E.; Grzyska, P. K.; Hausinger, R. P., Kinetic and spectroscopic investigation of CoII, NiII, and N-oxalylglycine inhibition of the FeII/α-ketoglutarate dioxygenase, TauD. *Biochemical and Biophysical Research Communications* **2005,** *338* (1), 191-197.

150. Park, H.; Ko, S.; Jeon, Y. H., Force field design and molecular dynamics simulations of factor-inhibiting HIF-1 and its complex with known inhibitors: Implications for rational inhibitor design. *Journal of Molecular Graphics and Modelling* **2010,** *29* (2), 221-228.

151. O'Hagan, D., Understanding organofluorine chemistry. An introduction to the C–F bond. *Chemical Society Reviews* **2008,** *37* (2), 308-319.

152. Ni, C.; Hu, J., The unique fluorine effects in organic reactions: recent facts and insights into fluoroalkylations. *Chemical Society Reviews* **2016,** *45* (20), 5441-5454.

153. O'Hagan, D.; Deng, H., Enzymatic Fluorination and Biotechnological Developments of the Fluorinase. *Chemical Reviews* **2015,** *115* (2), 634-649.

154. Becke, A. D., Density-functional thermochemistry. III. The role of exact exchange. *The Journal of Chemical Physics* **1993,** *98* (7), 5648-5652.

155. Stephens, P. J.; Devlin, F. J.; Chabalowski, C. F.; Frisch, M. J., Ab Initio Calculation of Vibrational Absorption and Circular Dichroism Spectra Using Density Functional Force Fields. *The Journal of Physical Chemistry* **1994,** *98* (45), 11623-11627.

156. Hertwig, R. H.; Koch, W., On the parameterization of the local correlation functional. What is Becke-3-LYP? *Chemical Physics Letters* **1997,** *268* (5), 345-351.

157. Smith, D. G. A.; Burns, L. A.; Patkowski, K.; Sherrill, C. D., Revised Damping Parameters for the D3 Dispersion Correction to Density Functional Theory. *The Journal of Physical Chemistry Letters* **2016,** *7* (12), 2197-2203.

158. Huang, J.; Li, C.; Wang, B.; Sharon, D. A.; Wu, W.; Shaik, S., Selective Chlorination of Substrates by the Halogenase SyrB2 Is Controlled by the Protein According to a Combined Quantum Mechanics/Molecular Mechanics and Molecular Dynamics Study. *ACS Catalysis* **2016,** *6* (4), 2694-2704.

159. Muller, P.; Fruit, C., Enantioselective catalytic aziridinations and asymmetric nitrene insertions into CH bonds. *Chemical Reviews* **2003,** *103* (8), 2905-2919.

160. Halfen, J. A., Recent advances in metal-mediated carbon-nitrogen bond formation reactions: Aziridination and amidation. *Current Organic Chemistry* **2005,** *9* (7), 657-669.

161. Degennaro, L.; Trinchera, P.; Luisi, R., Recent Advances in the Stereoselective Synthesis of Aziridines. *Chemical Reviews* **2014,** *114* (16), 7881-7929.

162. Zalatan, D. N.; Du Bois, J., Metal-Catalyzed Oxidations of C-H to C-N Bonds. *C-H Activation* **2010,** *292*, 347-378.

163. Kornecki, K. P.; Berry, J. F.; Powers, D. C.; Ritter, T., Metal-Metal Bond-Containing Complexes as Catalysts for C-H Functionalization. *Progress in Inorganic Chemistry, Vol 58* **2014,** *58*, 225-302.

164. Roizen, J. L.; Harvey, M. E.; Du Bois, J., Metal-Catalyzed Nitrogen-Atom Transfer Methods for the Oxidation of Aliphatic C-H Bonds. *Accounts of Chemical Research* **2012,** *45* (6), 911-922.

165. Davies, H. M. L.; Manning, J. R., Catalytic C-H functionalization by metal carbenoid and nitrenoid insertion. *Nature* **2008,** *451* (7177), 417-424.

166. Du Bois, J., Rhodium-Catalyzed C-H Amination. An Enabling Method for Chemical Synthesis. *Organic Process Research & Development* **2011,** *15* (4), 758-762.

167. Alderson, J. M.; Corbin, J. R.; Schomaker, J. M., Tunable, Chemo- and Site-Selective Nitrene Transfer Reactions through the Rational Design of Silver(I) Catalysts. *Accounts of Chemical Research* **2017,** *50* (9), 2147-2158.

168. Lu, H. J.; Zhang, X. P., Catalytic C-H functionalization by metalloporphyrins: recent developments and future directions. *Chemical Society Reviews* **2011,** *40* (4), 1899-1909.

169. Che, C. M.; Lo, V. K. Y.; Zhou, C. Y.; Huang, J. S., Selective functionalisation of saturated C-H bonds with metalloporphyrin catalysts. *Chemical Society Reviews* **2011,** *40* (4), 1950-1975.

170. Fantauzzi, S.; Caselli, A.; Gallo, E., Nitrene transfer reactions mediated by metallo-porphyrin complexes. *Dalton Transactions* **2009,** (28), 5434-5443.

171. Wolczanski, P. T., Activation of Carbon-Hydrogen Bonds via 1,2-RH-Addition/-Elimination to Early Transition Metal Imides. *Organometallics* **2018,** *37* (4), 505-516.

172. Hazari, N.; Mountford, P., Reactions and applications of titanium imido complexes. *Accounts of Chemical Research* **2005,** *38* (11), 839-849.

173. Muller, T. E.; Hultzsch, K. C.; Yus, M.; Foubelo, F.; Tada, M., Hydroamination: Direct addition of amines to alkenes and alkynes. *Chemical Reviews* **2008,** *108* (9), 3795-3892.

174. Odom, A. L.; McDaniel, T. J., Titanium-Catalyzed Multicomponent Couplings: Efficient One-Pot Syntheses of Nitrogen Heterocycles. *Accounts of Chemical Research* **2015,** *48* (11), 2822-2833.

175. Chiu, H. C.; Tonks, I. A., Trimethylsilyl-Protected Alkynes as Selective Cross-Coupling Partners in Titanium-Catalyzed 2+2+1 Pyrrole Synthesis. *Angewandte Chemie-International Edition* **2018,** *57* (21), 6090-6094.

176. Davis-Gilbert, Z. W.; Yao, L. J.; Tonks, I. A., Ti-Catalyzed Multicomponent Oxidative Carboamination of Alkynes with Alkenes and Diazenes. *Journal of the American Chemical Society* **2016,** *138* (44), 14570-14573.

177. Gilbert, Z. W.; Hue, R. J.; Tonks, I. A., Catalytic formal 2+2+1 synthesis of pyrroles from alkynes and diazenes via Ti-II/Ti-IV redox catalysis. *Nature Chemistry* **2016,** *8* (1), 63-68.

178. Davis-Gilbert, Z. W.; Wen, X. L.; Goodpaster, J. D.; Tonks, I. A., Mechanism of Ti-Catalyzed Oxidative Nitrene Transfer in 2+2+1 Pyrrole Synthesis from Alkynes and Azobenzene. *Journal of the American Chemical Society* **2018,** *140* (23), 7267-7281.

179. Davis-Gilbert, Z. W.; Kawakita, K.; Blechschmidt, D. R.; Tsurugi, H.; Mashima, K.; Tonks, I. A., In Situ Catalyst Generation and Benchtop-Compatible Entry Points for Ti-II/Ti-IV Redox Catalytic Reactions. *Organometallics* **2018,** *37* (23), 4439-4445.

180. Davis-Gilbert, Z. W.; Tonks, I. A., Titanium redox catalysis: insights and applications of an earth-abundant base metal. *Dalton Transactions* **2017,** *46* (35), 11522-11528.

181. Chiu, H. C.; See, X. Y.; Tonks, I. A., Dative Directing Group Effects in Ti-Catalyzed 2+2+1 Pyrrole Synthesis: Chemo- and Regioselective Alkyne Heterocoupling. *Acs Catalysis* **2019,** *9* (1), 216-223.

182. Beaumier, E. P.; Pearce, A. J.; See, X. Y.; Tonks, I. A., Modern applications of low-valent early transition metals in synthesis and catalysis. *Nature Reviews Chemistry* **2019,** *3* (1), 15-34.

183. Bauminger, S.; Meir, W., The use of carbodiimides in the preparation of immunizing conjugates. *Methods in Enzymology* **1980,** *70*, 151-159.

184. Li, P.; Xu, J. C., Highly efficient synthesis of peptides by rational utilization of novel coupling reagents. *Chinese Journal of Chemistry* **2000,** *18* (4), 456-466.

185. Albericio, F.; Chinchilla, R.; Dodsworth, D. J.; Najera, C., New trends in peptide coupling reagents. *Organic Preparations and Procedures International* **2001,** *33* (2-3), 205-303.

186. Pankratov, V. A., POLYCARBODIIMIDES. *Uspekhi Khimii* **1993,** *62* (12), 1185-1204.

187. Kennemur, J. G.; Novak, B. M., Advances in polycarbodiimide chemistry. *Polymer* **2011,** *52* (8), 1693-1710.

188. Khorana, H. G., THE CHEMISTRY OF CARBODIIMIDES. *Chemical Reviews* **1953,** *53* (2), 145-166.

189. Kurzer, F.; Douraghi-Zadeh, K., Advances in the Chemistry of Carbodiimides. *Chemical Reviews* **1967,** *67* (2), 107-152.

190. Williams, A.; Ibrahim, I. T., CARBODIIMIDE CHEMISTRY - RECENT ADVANCES. *Chemical Reviews* **1981,** *81* (6), 589-636.

191. Ulrich, H., Chemistry and Technology of Carbodiimides. John Wiley & Sons: Chichester, England, 2007.

192. Stevens, C. L.; Singhal, G. H.; Ash, A. B., CARBODIIMIDES . DEHYDRATION OF UREAS. *Journal of Organic Chemistry* **1967,** *32* (9), 2895-&.

193. Jaszay, Z. M.; Petnehazy, I.; Toke, L.; Szajani, B., PREPARATION OF CARBODIIMIDES USING PHASE-TRANSFER CATALYSIS. *Synthesis-Stuttgart* **1987,** (5), 520-523.

194. Mitsunobu, O.; Kato, K.; Tomari, M., Preparation of carbodiimides by the reaction of thioureas with diethyl azodicarboxylate. *Tetrahedron* **1970,** *26* (24), 5731-5736.

195. Kim, S.; Yi, K. Y., DI-2-PYRIDYL SULFITE - A NEW USEFUL REAGENT FOR THE PREPARATION OF N-SULFINYLAMINES, NITRILES, ISOCYANIDES, AND CARBODIIMIDES UNDER MILD CONDITIONS. *Tetrahedron Letters* **1986,** *27* (17), 1925-1928.

196. Saegusa, T.; Ito, Y.; Shimizu, T., Synthetic reactions by complex catalysts. XVIII. Reaction of an azide with isocyanide using an iron carbonyl catalyst. New route to carbodiimide. *The Journal of Organic Chemistry* **1970,** *35* (11), 3995-3996.

197. Cowley, R. E.; Eckert, N. A.; Elhaik, J.; Holland, P. L., Catalytic nitrene transfer from an imidoiron(III) complex to form carbodiimides and isocyanates. *Chemical Communications* **2009,** (13), 1760-1762.

198. Cowley, R. E.; Golder, M. R.; Eckert, N. A.; Al-Afyouni, M. H.; Holland, P. L., Mechanism of Catalytic Nitrene Transfer Using Iron(I)-Isocyanide Complexes. *Organometallics* **2013,** *32* (19), 5289-5298.

199. Mankad, N. P.; Muller, P.; Peters, J. C., Catalytic N-N Coupling of Aryl Azides To Yield Azoarenes via Trigonal Bipyramid Iron-Nitrene Intermediates. *Journal of the American Chemical Society* **2010,** *132* (12), 4083-4085.

200. Wiese, S.; Aguila, M. J. B.; Kogut, E.; Warren, T. H., beta-Diketiminato Nickel Imides in Catalytic Nitrene Transfer to Isocyanides. *Organometallics* **2013,** *32* (8), 2300-2308.

201. Laskowski, C. A.; Hillhouse, G. L., Group-Transfer Reactions of Ni(II)-Ni(II) Bridging Imido Complexes. Catalytic Formation of Carbodiimides and Isocyanates via Nitrene Transfer from Organoazides. *Organometallics* **2009,** *28* (20), 6114-6120.

202. Yousif, M.; Tjapkes, D. J.; Lord, R. L.; Groysman, S., Catalytic Formation of Asymmetric Carbodiimides at Mononuclear Chromium(II/IV) Bis(alkoxide) Complexes. *Organometallics* **2015,** *34* (20), 5119-5128.

203. Zhang, Z.; Li, Z. Y.; Fu, B.; Zhang, Z. H., Palladium-catalyzed cross-coupling reaction of azides with isocyanides. *Chemical Communications* **2015,** *51* (91), 16312-16315.

204. Kriegel, B. M.; Bergman, R. G.; Arnold, J., Nitrene Metathesis and Catalytic Nitrene Transfer Promoted by Niobium Bis(imido) Complexes. *Journal of the American Chemical Society* **2016,** *138* (1), 52-55.

205. Nguyen, A. I.; Zarkesh, R. A.; Lacy, D. C.; Thorson, M. K.; Heyduk, A. F., Catalytic nitrene transfer by a zirconium(IV) redox-active ligand complex. *Chemical Science* **2011,** *2* (1), 166-169.

206. Walsh, P. J.; Hollander, F. J.; Bergman, R. G., MONOMERIC AND DIMERIC ZIRCONOCENE IMIDO COMPOUNDS - SYNTHESIS, STRUCTURE, AND REACTIVITY. *Organometallics* **1993,** *12* (9), 3705-3723.

207. Dunn, S. C.; Hazari, N.; Cowley, A. R.; Green, J. C.; Mountford, P., Synthesis and reactions of group 4 imido complexes supported by cyclooctatetraene ligands. *Organometallics* **2006,** *25* (7), 1755-1770.

208. Royo, P.; Sánchez-Nieves, J., Oxo and imido/imido exchange and C–H activation reactions based on pentamethylcylopentadienyl imido tantalum complexes. *Journal of Organometallic Chemistry* **2000,** *597* (1), 61-68.

209. Barnea, E.; Majumder, S.; Staples, R. J.; Odom, A. L., One-Step Route to 2,3-Diaminopyrroles Using a Titanium-Catalyzed Four-Component Coupling. *Organometallics* **2009,** *28* (13), 3876-3881.

210. Aldrich, K. E.; Odom, A. L., Titanium-Catalyzed Hydroamination and Multicomponent Coupling with a Simple Silica-Supported Catalyst. *Organometallics* **2018,** *37* (23), 4341-4349.

211. Heins, S. P.; Wolczanski, P. T.; Cundari, T. R.; MacMillan, S. N., Redox non-innocence permits catalytic nitrene carbonylation by (dadi)Ti=NAd (Ad = adamantyl). *Chemical Science* **2017,** *8* (5), 3410-3418.

212. Zhao, Y.; Truhlar, D. G., The M06 suite of density functionals for main group thermochemistry, thermochemical kinetics, noncovalent interactions, excited states, and transition elements: two new functionals and systematic testing of four M06-class functionals and 12 other functionals. *Theoretical Chemistry Accounts* **2008,** *120* (1-3), 215-241.

213. Krishnan, R.; Binkley, J. S.; Seeger, R.; Pople, J. A., SELF-CONSISTENT MOLECULAR-ORBITAL METHODS. XX. BASIS SET FOR CORRELATED WAVE-FUNCTIONS. *Journal of Chemical Physics* **1980,** *72* (1), 650-654.

214. Marenich, A. V.; Cramer, C. J.; Truhlar, D. G., Universal Solvation Model Based on Solute Electron Density and on a Continuum Model of the Solvent Defined by the Bulk Dielectric Constant and Atomic Surface Tensions. *Journal of Physical Chemistry B* **2009,** *113* (18), 6378-6396.

215. Knizia, G., Intrinsic Atomic Orbitals: An Unbiased Bridge between Quantum Theory and Chemical Concepts. *Journal of Chemical Theory and Computation* **2013,** *9* (11), 4834-4843.

216. Knizia, G.; Klein, J., Electron Flow in Reaction Mechanisms-Revealed from First Principles. *Angewandte Chemie-International Edition* **2015,** *54* (18), 5518-5522.

217. Werner, H. J.; Knowles, P. J.; Knizia, G.; Manby, F. R.; Schutz, M., Molpro: a general-purpose quantum chemistry program package. *Wiley Interdisciplinary Reviews-Computational Molecular Science* **2012,** *2* (2), 242-253.

218. MOLPRO, v., a package of ab initio programs, Werner, H. J.; Knowles, P. J.; Knizia, G.; Manby, F. R.; Schütz, M.; Celani, P.; Korona, T.; Lindh, R.; Mitrushenkov, A.; Rauhut, G.; Shamasun-dar, K. R.; Adler, T. B.; Amos, R. D.; Bernhardsson, A.; Berning, A.; Cooper, D. L.; Deegan, M. J. O.; Dobbyn, A. J.; Eckert, F.; Goll, E.; Hampel, C.; Hesselmann, A.; Hetzer, G.; Hrenar, T.; Jansen, G.; Köppl, C.; Liu, Y.; Lloyd, A. W.; Mata, R. A.; May, A. J.; McNicholas, S. J.; Meyer, W.; Mura, M. E.; Nicklass, A.; O'Neill, D. P.; Palmieri, P.; Peng, D.; Pflöger, K.; Pitzer, R.; Reiher, M.; Shiozaki, T.; Stoll, H.; Stone, A. J.; Tarroni, R.; Thorsteinsson, T.; Wang, M.; see http://www.molpro.net.

219. Glendening, E. D.; Landis, C. R.; Weinhold, F., NBO 6.0: Natural bond orbital analysis program. *Journal of Computational Chemistry* **2013,** *34* (16), 1429-1437.

220. Weinhold, F.; Landis, C. R., *Valency and Bonding: A Natural Bond Orbital Donor-Acceptor Perspective*. Cambridge University Press: Cambridge, 2005.

221. Webster, A. J.; Mueller, C. M.; Foegen, N. P.; Sit, P. H. L.; Speetzen, E. D.; Cunningham, D. W.; D'Acchioli, J. S., Oxidation states "naturally": A Natural Bond Orbital method for determining transition metal oxidation states. *Polyhedron* **2016,** *114*, 128-132.

222. Beaumier, E. P.; McGreal, M. E.; Pancoast, A. R.; Wilson, R. H.; Moore, J. T.; Graziano, B. J.; Goodpaster, J. D.; Tonks, I. A., Carbodiimide Synthesis via Ti-Catalyzed Nitrene Transfer from Diazenes to Isocyanides. *ACS Catalysis* **2019,** *9* (12), 11753-11762.

223. Hill, J. E.; Profilet, R. D.; Fanwick, P. E.; Rothwell, I. P., SYNTHESIS, STRUCTURE, AND REACTIVITY OF ARYLOXO(IMIDO)TITANIUM COMPLEXES. *Angewandte Chemie-International Edition* **1990,** *29* (6), 664-665.

224. Edema, J. J. H.; Duchateau, R.; Gambarotta, S.; Hynes, R.; Gabe, E., NOVEL TITANIUM(II) AMINE COMPLEXES L4TICL2 L = 1/2 N,N,N',N'-TETRAMETHYLETHYLENEDIAMINE (TMEDA), 1/2 N,N,N'-TRIMETHYLETHYLENEDIAMINE, PYRIDINE, 1/2 2,2'-BIPYRIDINE - SYNTHESIS AND CRYSTAL-STRUCTURE OF MONOMERIC TRANS-(TMEDA)2TICL2. *Inorganic Chemistry* **1991,** *30* (2), 154-156.

225. Gray, S. D.; Thorman, J. L.; Adamian, V. A.; Kadish, K. M.; Woo, L. K., Synthesis, electrochemistry, and imido transfer reactions of (TTP)Ti(eta(2)-PhN = NPh). *Inorganic Chemistry* **1998,** *37* (1), 1-4.

226. Wijeratne, G. B.; Zolnhofer, E. M.; Fortier, S.; Grant, L. N.; Carroll, P. J.; Chen, C. H.; Meyer, K.; Krzystek, J.; Ozarowski, A.; Jackson, T. K.; Mindiola, D. J.; Telser, J., Electronic Structure and Reactivity of a Well-Defined Mononuclear Complex of Ti(II). *Inorganic Chemistry* **2015,** *54* (21), 10380-10397.

227. Guo, J. D.; Deng, X.; Song, C. Y.; Lu, Y.; Qu, S. L.; Dang, Y. F.; Wang, Z. X., Differences between the elimination of early and late transition metals: DFT mechanistic insights into the titanium-catalyzed synthesis of pyrroles from alkynes and diazenes. *Chemical Science* **2017,** *8* (3), 2413-2425.

228. Guo, J. D.; Lu, Y.; Zhao, R. H.; Liu, Z. Y.; Menberu, W.; Wang, Z. X., Strong Preference of the Redox-Neutral Mechanism over the Redox Mechanism for the Ti-IV Catalysis Involved in the Carboamination of Alkyne with Alkene and Diazene. *Chemistry-a European Journal* **2018,** *24* (27), 7010-7025.

229. Zuckerman, R. L.; Bergman, R. G., Structural factors that influence the course of overall 2+2 cycloaddition reactions between imidozirconocene complexes and heterocumulenes. *Organometallics* **2000,** *19* (23), 4795-4809.

230. Zuckerman, R. L.; Bergman, R. G., Mechanistic investigation of cycloreversion/cycloaddition reactions between zirconocene metallacycle complexes and unsaturated organic substrates. *Organometallics* **2001,** *20* (9), 1792-1807.

231. Guiducci, A. E.; Boyd, C. L.; Mountford, P., Reactions of cyclopentadienyl-amidinate titanium imido compounds with CS2, COS, isocyanates, and other unsaturated organic compounds. *Organometallics* **2006,** *25* (5), 1167-1187.

232. Meisel, I.; Hertel, G.; Weiss, K., Investigations of polymerizations and metathesis reactions: Part IX11Part VIII, J. Mol. Catal., 36 (1986) 39.. Metathesis of carbodiimides with tungsten(VI)-imido complexes. *Journal of Molecular Catalysis* **1986,** *36* (1), 159-162.

233. Birdwhistell, K. R.; Lanza, J.; Pasos, J., Carbodiimide metathesis catalyzed by vanadium oxo and imido complexes via imido transfer. *Journal of Organometallic Chemistry* **1999,** *584* (1), 200-205.

234. Ong, T. G.; Yap, G. P. A.; Richeson, D. S., Catalytic C=N bond metathesis of carbodiimides by group 4 and 5 imido complexes supported by guanidinate ligands. *Chemical Communications* **2003,** (20), 2612-2613.

235. Louie, J., Transition metal catalyzed reactions of carbon dioxide and other heterocumulenes. *Current Organic Chemistry* **2005,** *9* (7), 605-623.

236. Lehn, J. M., SUPRAMOLECULAR CHEMISTRY - RECEPTORS, CATALYSTS, AND CARRIERS. *Science* **1985,** *227* (4689), 849-856.

237. Raju, M. V. R.; Wilharm, R. K.; Dresel, M. J.; McGreal, M. E.; Mansergh, J. P.; Marting, S. T.; Goodpaster, J. D.; Pierre, V. C., The Stability of the Complex and the Basicity of the Anion Impact the Selectivity and Affinity of Tripodal

Gadolinium Complexes for Anions. *Inorganic Chemistry* **2019,** *58* (22), 15189-15201.

238. Piguet, C.; Bunzli, J. C. G., Mono- and polymetallic lanthanide-containing functional assemblies: a field between tradition and novelty. *Chemical Society Reviews* **1999,** *28* (6), 347-358.

239. Faulkner, S.; Pope, S. J. A.; Burton-Pye, B. P., Lanthanide complexes for luminescence imaging applications. *Applied Spectroscopy Reviews* **2005,** *40* (1), 1-31.

240. Ma, X.; Zhao, Y. L., Biomedical Applications of Supramolecular Systems Based on Host-Guest Interactions. *Chemical Reviews* **2015,** *115* (15), 7794-7839.

241. Cui, H. G.; Xu, B., Supramolecular medicine. *Chemical Society Reviews* **2017,** *46* (21), 6430-6432.

242. Safont-Sempere, M. M.; Fernandez, G.; Wurthner, F., Self-Sorting Phenomena in Complex Supramolecular Systems. *Chemical Reviews* **2011,** *111* (9), 5784-5814.

243. Binnemans, K., Lanthanide-Based Luminescent Hybrid Materials. *Chemical Reviews* **2009,** *109* (9), 4283-4374.

244. Martinez-Calvo, M.; Kotova, O.; Mobius, M. E.; Bell, A. P.; McCabe, T.; Boland, J. J.; Gunnlaugsson, T., Healable Luminescent Self-Assembly Supramolecular Metallogels Possessing Lanthanide (Eu/Tb) Dependent Rheological and Morphological Properties. *Journal of the American Chemical Society* **2015,** *137* (5), 1983-1992.

245. Burai, L.; Hietapelto, V.; Kiraly, R.; Toth, E.; Brucher, E., Stability constants and H-1 relaxation effects of ternary complexes formed between Gd-DTPA, Gd-DTPA-BMA, Gd-DOTA, and Gd-EDTA and citrate, phosphate, and carbonate ions. *Magnetic Resonance in Medicine* **1997,** *38* (1), 146-150.

246. Bruce, J. I.; Dickins, R. S.; Govenlock, L. J.; Gunnlaugsson, T.; Lopinski, S.; Lowe, M. P.; Parker, D.; Peacock, R. D.; Perry, J. J. B.; Aime, S.; Botta, M., The selectivity of reversible oxy-anion binding in aqueous solution at a chiral europium and terbium center: Signaling of carbonate chelation by changes in the form and circular polarization of luminescence emission. *Journal of the American Chemical Society* **2000,** *122* (40), 9674-9684.

247. Dickins, R. S.; Aime, S.; Batsanov, A. S.; Beeby, A.; Botta, M.; Bruce, J.; Howard, J. A. K.; Love, C. S.; Parker, D.; Peacock, R. D.; Puschmann, H., Structural, luminescence, and NMR studies of the reversible binding of acetate, lactate, citrate, and selected amino acids to chiral diaqua ytterbium, gadolinium,

and europium complexes. *Journal of the American Chemical Society* **2002,** *124* (43), 12697-12705.

248. Atkinson, P.; Bretonniere, Y.; Parker, D., Chemoselective signalling of selected phospho-anions using lanthanide luminescence. *Chemical Communications* **2004,** (4), 438-439.

249. Charbonniere, L. J.; Schurhammer, R.; Mameri, S.; Wipff, G.; Ziessel, R. F., Photophysical and structural impact of phosphorylated anions associated to lanthanide complexes in water. *Inorganic Chemistry* **2005,** *44* (20), 7151-7160.

250. Atkinson, P.; Murray, B. S.; Parker, D., A cationic lanthanide complex binds selectively to phosphorylated tyrosine sites, aiding NMR analysis of the phosphorylated insulin receptor peptide fragment. *Organic & Biomolecular Chemistry* **2006,** *4* (16), 3166-3171.

251. Schaferling, M.; Wolfbeis, O. S., Europium tetracycline as a luminescent probe for nucleoside phosphates and its application to the determination of kinase activity. *Chemistry-a European Journal* **2007,** *13* (15), 4342-4349.

252. Wang, Y. W.; Liu, S. B.; Yang, Y. L.; Wang, P. Z.; Zhang, A. J.; Peng, Y., A Terbium(III)-Complex-Based On-Off Fluorescent Chemosensor for Phosphate Anions in Aqueous Solution and Its Application in Molecular Logic Gates. *Acs Applied Materials & Interfaces* **2015,** *7* (7), 4415-4422.

253. Schaferling, M.; Aaritalo, T.; Soukka, T., Multidentate Europium Chelates as Luminoionophores for Anion Recognition: Impact of Ligand Design on Sensitivity and Selectivity, and Applicability to Enzymatic Assays. *Chemistry-a European Journal* **2014,** *20* (18), 5298-5308.

254. Sahoo, J.; Arunachalam, R.; Subramanian, P. S.; Suresh, E.; Valkonen, A.; Rissanen, K.; Albrecht, M., Coordinatively Unsaturated Lanthanide(III) Helicates: Luminescence Sensors for Adenosine Monophosphate in Aqueous Media. *Angewandte Chemie-International Edition* **2016,** *55* (33), 9625-9629.

255. Hewitt, S. H.; Parris, J.; Mailhot, R.; Butler, S. J., A continuous luminescence assay for monitoring kinase activity: signalling the ADP/ATP ratio using a discrete europium complex. *Chemical Communications* **2017,** *53* (94), 12626-12629.

256. Shuvaev, S.; Fox, M. A.; Parker, D., Monitoring of the ADP/ATP Ratio by Induced Circularly Polarised Europium Luminescence. *Angewandte Chemie-International Edition* **2018,** *57* (25), 7488-7492.

257. Harris, S. M.; Nguyen, J. T.; Pailloux, S. L.; Mansergh, J. P.; Dresel, M. J.; Swanholm, T. B.; Gao, T.; Pierre, V. C., Gadolinium Complex for the Catch and

Release of Phosphate from Water. *Environmental Science & Technology* **2017,** *51* (8), 4549-4558.

258. Dickins, R. S.; Gunnlaugsson, T.; Parker, D.; Peacock, R. D., Reversible anion binding in aqueous solution at a cationic heptacoordinate lanthanide centre: selective bicarbonate sensing by time-delayed luminescence. *Chemical Communications* **1998,** (16), 1643-1644.

259. Bretonniere, Y.; Cann, M. J.; Parker, D.; Slater, R., Design, synthesis and evaluation of ratiometric probes for hydrogencarbonate based on europium emission. *Organic & Biomolecular Chemistry* **2004,** *2* (11), 1624-1632.

260. Bretonniere, Y.; Cann, M. J.; Parker, D.; Slater, R., Ratiometric probes for hydrogencarbonate analysis in intracellular or extracellular environments using europium luminescence. *Chemical Communications* **2002,** (17), 1930-1931.

261. Murray, B. S.; New, E. J.; Pal, R.; Parker, D., Critical evaluation of five emissive europium(III) complexes as optical probes: correlation of cytotoxicity, anion and protein affinity with complex structure, stability and intracellular localisation profile. *Organic & Biomolecular Chemistry* **2008,** *6* (12), 2085-2094.

262. Piccinelli, F.; De Rosa, C.; Melchior, A.; Faura, G.; Tolazzi, M.; Bettinelli, M., Eu(III) and Tb(III) complexes of 6-fold coordinating ligands showing high affinity for the hydrogen carbonate ion: a spectroscopic and thermodynamic study. *Dalton Transactions* **2019,** *48* (4), 1202-1216.

263. Tripier, R.; Platas-Iglesias, C.; Boos, A.; Morfin, J. F.; Charbonniere, L., Towards Fluoride Sensing with Positively Charged Lanthanide Complexes. *European Journal of Inorganic Chemistry* **2010,** (18), 2735-2745.

264. Lima, L. M. P.; Lecointre, A.; Morfin, J. F.; de Blas, A.; Visvikis, D.; Charbonniere, L. J.; Platas-Iglesias, C.; Tripier, R., Positively Charged Lanthanide Complexes with Cyclen-Based Ligands: Synthesis, Solid-State and Solution Structure, and Fluoride Interaction. *Inorganic Chemistry* **2011,** *50* (24), 12508-12521.

265. Blackburn, O. A.; Chilton, N. F.; Keller, K.; Tait, C. E.; Myers, W. K.; McInnes, E. J. L.; Kenwright, A. M.; Beer, P. D.; Timmel, C. R.; Faulkner, S., Spectroscopic and Crystal Field Consequences of Fluoride Binding by YbDTMA (3+) in Aqueous Solution. *Angewandte Chemie-International Edition* **2015,** *54* (37), 10783-10786.

266. Blackburn, O. A.; Edkins, R. M.; Faulkner, S.; Kenwright, A. M.; Parker, D.; Rogers, N. J.; Shuvaev, S., Electromagnetic susceptibility anisotropy and its importance for paramagnetic NMR and optical spectroscopy in lanthanide coordination chemistry. *Dalton Transactions* **2016,** *45* (16), 6782-6800.

267. Routledge, J. D.; Zhang, X. J.; Connolly, M.; Tropiano, M.; Blackburn, O. A.; Kenwright, A. M.; Beer, P. D.; Aldridge, S.; Faulkner, S., Lanthanide Complexes that Respond to Changes in Cyanide Concentration in Water. *Angewandte Chemie-International Edition* **2017,** *56* (27), 7783-7786.

268. Huang, S. Y.; Pierre, V. C., A turn-on luminescent europium probe for cyanide detection in water. *Chemical Communications* **2018,** *54* (66), 9210-9213.

269. Leonard, J. P.; dos Santos, C. M. G.; Plush, S. E.; McCabe, T.; Gunnlaugsson, T., pH driven self-assembly of a ternary lanthanide luminescence complex: the sensing of anions using a beta-diketonate-Eu(III) displacement assay. *Chemical Communications* **2007,** (2), 129-131.

270. Hammell, J.; Buttarazzi, L.; Huang, C. H.; Morrow, J. R., Eu(III) Complexes as Anion-Responsive Luminescent Sensors and Paramagnetic Chemical Exchange Saturation Transfer Agents. *Inorganic Chemistry* **2011,** *50* (11), 4857-4867.

271. Pierre, V. C.; Botta, M.; Aime, S.; Raymond, K. N., Substituent effects on Gd(III)-based MRI contrast agents: Optimizing the stability and selectivity of the complex and the number of coordinated water molecules. *Inorganic Chemistry* **2006,** *45* (20), 8355-8364.

272. Esplin, T. L.; Cable, M. L.; Gray, H. B.; Ponce, A., Terbium-Macrocycle Complexes as Chemical Sensors: Detection of an Aspirin Metabolite in Urine Using a Salicylurate-Specific Receptor Site. *Inorganic Chemistry* **2010,** *49* (10), 4643-4647.

273. Langton, M. J.; Serpell, C. J.; Beer, P. D., Anion Recognition in Water: Recent Advances from a Supramolecular and Macromolecular Perspective. *Angewandte Chemie-International Edition* **2016,** *55* (15), 4629-4629.

274. Aletti, A. B.; Gillen, D. M.; Gunnlaugsson, T., Luminescent/colorimetric probes and (chemo-) sensors for detecting anions based on transition and lanthanide ion receptor/binding complexes. *Coordination Chemistry Reviews* **2018,** *354*, 98-120.

275. Merbach, H.; Helm, L.; Toth, E., Chemistry of contrast agents in medical resonance imaging. John Wiley and Sons: Hoboken, NJ, 2013.

276. Caravan, P.; Ellison, J. J.; McMurry, T. J.; Lauffer, R. B., Gadolinium(III) chelates as MRI contrast agents: Structure, dynamics, and applications. *Chemical Reviews* **1999,** *99* (9), 2293-2352.

277. Doble, D. M. J.; Melchior, M.; O'Sullivan, B.; Siering, C.; Xu, J. D.; Pierre, V. C.; Raymond, K. N., Toward optimized high-relaxivity MRI agents: The effect of

ligand basicity on the thermodynamic stability of hexadentate hydroxypyridonate/catecholate gadolinium(III) complexes. *Inorganic Chemistry* **2003,** *42* (16), 4930-4937.

278. O'Sullivan, B.; Doble, D. M. J.; Thompson, M. K.; Siering, C.; Xu, J. D.; Botta, M.; Aime, S.; Raymond, K. N., The effect of ligand scaffold size on the stability of tripodal hydroxypyridonate gadolinium complexes. *Inorganic Chemistry* **2003,** *42* (8), 2577-2583.

279. Jocher, C. J.; Moore, E. G.; Xu, J. D.; Avedano, S.; Botta, M.; Aime, S.; Raymond, K. N., 1,2-hydroxypyridonates as contrast agents for magnetic resonance imaging: TREN-1,2-HOPO. *Inorganic Chemistry* **2007,** *46* (22), 9182-9191.

280. De Proft, F.; Sablon, N.; Tozer, D. J.; Geerlings, P., Calculation of negative electron affinity and aqueous anion hardness using Kohn-Sham HOMO and LUMO energies. *Faraday Discussions* **2007,** *135*, 151-159.

281. Parr, R. G.; Pearson, R. G., Absolute hardness - companion parameter to absolute electronegativity. *Journal of the American Chemical Society* **1983,** *105* (26), 7512-7516.

282. Pearson, R. G., Absolute electronegativity and hardness correlated with molecular-orbital theory. *Proceedings of the National Academy of Sciences of the United States of America* **1986,** *83* (22), 8440-8441.

283. Koopmans, T., Über die Zuordnung von Wellenfunktionen und Eigenwerten zu den Einzelnen Elektronen Eines Atoms. *Physica* **1934,** *1* (1), 104-113.

284. Tozer, D. J.; De Proft, F., Computation of the hardness and the problem of negative electron affinities in density functional theory. *Journal of Physical Chemistry A* **2005,** *109* (39), 8923-8929.

285. Perdew, J. P.; Burke, K.; Ernzerhof, M., Generalized gradient approximation made simple. *Physical Review Letters* **1996,** *77* (18), 3865-3868.

286. Kendall, R. A.; Jr., T. H. D.; Harrison, R. J., Electron affinities of the first-row atoms revisited. Systematic basis sets and wave functions. *The Journal of Chemical Physics* **1992,** *96* (9), 6796-6806.

287. Woon, D. E.; Dunning, T. H., GAUSSIAN-BASIS SETS FOR USE IN CORRELATED MOLECULAR CALCULATIONS .3. THE ATOMS ALUMINUM THROUGH ARGON. *Journal of Chemical Physics* **1993,** *98* (2), 1358-1371.

288. Wilson, A. K.; Woon, D. E.; Peterson, K. A.; Dunning, T. H., Gaussian basis sets for use in correlated molecular calculations. IX. The atoms gallium through krypton. *Journal of Chemical Physics* **1999,** *110* (16), 7667-7676.

289. Klamt, A.; Schuurmann, G., COSMO - a new approach to dielectric screening in solvents with explicit expressions for the screening energy and its gradient. *Journal of the Chemical Society-Perkin Transactions 2* **1993,** (5), 799-805.

290. Écija, D.; Urgel, J. I.; Seitsonen, A. P.; Auwärter, W.; Barth, J. V., Lanthanide-Directed Assembly of Interfacial Coordination Architectures–From Complex Networks to Functional Nanosystems. *Accounts of Chemical Research* **2018,** *51* (2), 365-375.

291. Hoppert, M., Metalloenzymes. In *Encyclopedia of Geobiology*, Reitner, J.; Thiel, V., Eds. Springer Netherlands: Dordrecht, 2011; pp 558-563.

292. Wächtershäuser, G., Evolution of the first metabolic cycles. *Proceedings of the National Academy of Sciences* **1990,** *87* (1), 200-204.

293. Holm, R. H.; Kennepohl, P.; Solomon, E. I., Structural and Functional Aspects of Metal Sites in Biology. *Chemical Reviews* **1996,** *96* (7), 2239-2314.